UNIVERSITEIT VAN PRETORIA
UNIVERSITY OF PRETORIA
YUNIBESITHI YA PRETORIA

Faculty of Engineering,
Built Environment and
Information Technology

Fakulteit Ingenieurswese, Bou-omgewing en
Inligtingtegnologie / Lefapha la Boetšenere,
Tikologo ya Kago le Theknolotši ya Tshedimošo

Extracting Blade Condition Information from the Pressure Field around a Turbine Blade

---

Submitted in Partial Fulfilment of the Requirements for the Degree
Master of Mechanical Engineering

Student:	*Supervisor:*
Gregory Janse van Vuuren	Prof. P.S. Heyns
u14182492	

2019-11-12

UNIVERSITY OF PRETORIA

FACULTY OF ENGINEERING, BUILT ENVIRONMENT AND INFORMATION TECHNOLOGY

DEPARTMENT OF MECHANICAL AND AERONAUTICAL ENGINEERING

Abstract

Extracting Blade Condition Information from the Pressure Field around a Turbine Blade

Author:	Gregory Janse van Vuuren
Student Number:	u14182492
Supervisor:	Prof. P.S. Heyns
Department:	Mechanical and Aeronautical Engineering
Degree:	Master of Mechanical Engineering
University:	University of Pretoria
Year:	2019

Turbine stages are exposed to a variety of excitation sources in the power industry. The resulting forced vibration excitation of the blades may occur near a blade's natural frequency. Blade vibration is an inevitable, inherent characteristic of turbines as the rotor blades travel through the trailing wakes of the upstream stator blades. Blade vibration can be worsened by other mechanisms such as pitting, corrosion fatigue and stress corrosion cracking commonly experienced in the power industry.

Measuring turbine blade vibration allows for condition monitoring of the blades for damage. This is often coupled with finite element models of the blades or with computational fluid dynamic models of the flow field around the blades. These numerical methods, although well-established, lack the complexity of the true multiphysics phenomena within a turbine. As the blade vibration measurement techniques essentially capture blade vibration that is the result of fluid-structure interaction (FSI), blade vibration should be modelled as a coupled problem, but this is usually computationally expensive.

A rudimentary yet fundamentally correct numerical model of a turbine stage is thus required to model the fluid-structure interaction while minimising computational costs and retaining accuracy. If this can be achieved and blade health information can be detected in the flow field within the model, further analyses can then be put forth to predict blade health over time.

The main objective of this study is to investigate the extent to which blade condition information can be extracted from a transient three-dimensional two-way FSI model of a blade passage containing a single rotor and stator blade. An experimental single-stage test turbine with five stator and five rotor blades is used to gather experimental data. The experimental data is used to validate the FSI model in the time and frequency domains. Two rotor blade assemblies were tested with the first configuration consisting of five healthy blades, and the second configuration consisting of four healthy blades and one damaged blade. All simulations are performed at constant rotational speeds for one single revolution of the rotor. Structural damping of the rotor blades is not considered. All numerical simulations are carried out using the commercial multiphysics software package of Ansys R2 2019 and the explicit use of CFX for the CFD simulations.

The results of the FSI model compare well to the experimental results when considering the simplifying assumptions made for the development of the numerical model. The first natural frequency and blade passing frequencies of the healthy and damaged blades can be extracted from the pressure field of the FSI model at critical speeds. Similar findings were observed in the fluid mesh deformation time profiles around the blade tips. Blade excitation is strongly coupled to engine-ordered vibration frequencies, specifically the blade passing frequencies and its first harmonic. Challenges are realised when modelling a single damaged blade that is part of a larger, healthy assembly of rotor blades. The compromise of reducing computational effort is highlighted here.

However, very promising results pertaining to blade condition information extraction from the two-way FSI model pressure field are obtained. These results have established a foundation on which a more complex FSI model can be built and coupled with a fatigue or remaining useful life study. It is suggested that future work should include structural damping of the rotor blades, a larger computational domain, and investigation of longer simulation times.

Acknowledgements

I would like to acknowledge the following entities who contributed to the research presented in this dissertation:

- The Centre for Asset Integrity Management (C-AIM) of the University of Pretoria for providing funds for the research and an environment conducive to learning and personal development.
- Prof. P.S. Heyns - for your technical insight, guidance and your enthusiasm throughout the study. You provide the opportunities for students to grow in knowledge and the environment in which they can produce research of international standard.
- Mr. Breitenbach - for the momentous support getting the rotor test bench modified, the countless discussions of how to plan my experimental work and the setting up of the data acquisitioning system.
- Peet Kruger and the Mechanical Workshop - for the long hours manufacturing the experimental blades and all unforeseen modifications that had to be made to the rotor test bench.
- Brian - for assistance in assembling the modified rotor test bench and setting up of the data acquisitioning system.
- Johan, PJ and Marcel - for the companionship, long brainstorming sessions and infinite amounts of coffee.
- Ms. Bonolo Mokoka - for the administrative support and assistance in procuring additional equipment.
- Eskom Power Plant Engineering Institute (EPPEI) for your support in turbine related research.
- Bradley, my little brother - for the infinite number of cups of coffee for my late nights at home and even more cups of coffee in the mornings.
- My mother and father - for your unconditional love and support.
- Last, but not least, Moniqué - my fiancée for her constant support, love and patience while facing her own challenges with her master's degree study. You are my rock.

Table of Contents

Nomenclature

English letters and symbols

a, A	Amplitude	mm
CFL	Courant-Friedrichs-Levy number	$-$
$\boldsymbol{D}$	Damping (Matrix)	$N \cdot s/m$
e	Internal Energy	J/kg
f	Frequency	Hz
F	Force	N
g	Gravitational Acceleration	m/s^2
k	Turbulent Kinetic Energy	J/kg
L	Characteristic Length	m
$\boldsymbol{K}$	Stiffness (Matrix)	N/m
$\boldsymbol{M}$	Mass (Matrix)	kg
N	Rotational Speed	rpm
p	Numerical order accuracy	$-$
r	Grid refinement ratio	$-$
Re	Reynolds number	$-$
R	Radius	m
T	Time period	s
	Temperature	K
t	Time	s
u, x	Displacement	m
V	Velocity	m/s
y^+	Y-plus value	$-$

Greek symbols

Δ	Difference/change in quantity	
δ	Kronecker's delta	
ε	Turbulent kinetic energy dissipation rate	$J/kg \cdot s$
ρ	Density	kg/m^3
μ	Dynamic Viscosity	$Pa \cdot s$
ω	Rotational frequency	rad/s
	Specific turbulent kinetic energy dissipation rate	Hz
Ω	Rotational frequency (shaft)	rad/s
φ	Mode shape	$-$
τ	Viscous Stress Tensor	Pa

Special characters

$\tilde{\ }$	Vector/Estimate
$[\ \ ]$	Matrix (bold)
$[\dot{\ }]$	First time derivative
$[\ddot{\ }]$	Second time derivative

$\|\ \|$	Magnitude
∂	Partial Derivative
$\frac{D}{Dt}$	Total Derivative

Subscripts

i, j, k	Cartesian coordinate directions
n	Natural (frequency)
off	Offset
pp	Passing Period

Abbreviations and Acronyms

BPF	Blade Passing Frequency
BPP	Blade Passing Period
BTT	Blade Tip Timing
C-AIM	Centre for Asset Integrity Management
CFD	Computational Fluid Dynamics
CVS	Casing Vibration Signal
CPS	Casing Pressure Signal
EO	Engine Order
Exp	Experimental
FE	Finite Element
FEA	Finite Element Analysis
FEM	Finite Element Model/Method
FM	Frequency Modulated
FMGS	Frequency Modulated Grid System
FSI	Fluid-structure Interaction, Fluid Structure Interaction model
FTT	Fast Fourier Transform
GCI	Grid Convergence Index
HCF	High Cycle Fatigue
HP	High Pressure
LCF	Low Cycle Fatigue
LE	Leading Edge
LP	Low Pressure
NSE	Navier-Stokes Equations
MDOF	Multi-degree of Freedom
MPR	Multiple-per-revolution
ODE	Ordinary Differential Equation
OPR	Once-per-revolution
PSD	Power Spectral Density
RANS	Reynolds-averaged Navier-Stokes
RKE	Realizable $k - \varepsilon$
SDOF	Single Degree of Freedom
SPF	Stator Passing Frequency
SSTKO	Shear Stress Transport $k - \omega$
TE	Trailing Edge

1 Introduction

The following sections will give some background to this dissertation, present the problem statement, and scope and give an overview of the remainder of the dissertation. The majority of this theory and literature presented relates to turbomachinery as a whole and not only to steam turbines, and turbines in general. The discussions and arguments will however be in context of axial flow steam turbines as this is the focus of this study.

1.1 Background

Turbomachine stages are exposed to a variety of excitation sources leading to forced vibration responses that may occur in the vicinity of a blade's natural frequency (Carrington *et al.*, 2001). Flutter in its various forms and physical blade damage, are identified as root causes to blade vibration (McCloskey, 2002). As the structural motion of the blades directly affects the fatigue life, performance and integrity of the assembly, responses need to be monitored (Heath and Imregun, 1996).

Measuring turbine blade vibration is driven by the need to obtain either the blade's forced response magnitude and associated frequency or to estimate the modal parameters of the blade (Forbes, Alshroof and Randall, 2011). Acquiring this information allows for the estimation of high cycle fatigue life or the direct condition monitoring of the blades for damage.

A study by Meher-Homji (1995) indicated that gas turbine failures due to blade faults were as high as 42% and similar failure numbers were reported by Epri (1985) for steam turbines. One can only be led to imagine that these failure occurrences have decreased over the last few years with the technological advancements. But, even so, blade vibration is inevitable as it is an inherent characteristic of turbines due to the rotor blades travelling through the trailing wakes of the upstream stator blades (Alshroof *et al.*, 2012).

Various blade vibration measurement techniques exist which are categorised as either intrusive or nonintrusive. The data obtained using such methods, after the necessary processing, are then often linked with finite element models of the blades or with computational fluid dynamic models of the flow field around the blades for validation purposes. The results of such investigations can then either be used for online condition monitoring of the turbomachine blade health or for the prediction of the fatigue life and essentially the remaining useful life of the blades. The aforementioned numerical methods, although well-established, lack the complexity of the true multiphysics phenomena within a turbomachine. As the blade vibration measurement techniques essentially capture blade vibration that is resultant of fluid-structure interaction, modelling of this fluid-structure interaction has been given some attention recently (see Rao and Dutta, 2014; Brahimi and Ouibrahim, 2016; Krack, Salles and Thouverez, 2016; Ubulom, Neely and Shankar, 2017).

Frequently, problems that involve fluid-structure interaction can be modelled as uncoupled problems within their specific domains. The fluid flow and structural motion within a turbomachine, however, is an example of a substantially complex problem that needs to be modelled due to the complicated geometry of the flow paths. Due to this complexity and the fact that fluid-structure interaction within turbines have primarily been modelled with transient solution procedures (Alshroof *et al.*, 2012), computational costs are high. Modelling of the fluid-structure interaction within a turbine are generally split up into either one-way or two-way coupling between the two numerical domains where the former only considers the effect of the one domain on the other (Alshroof *et al.*, 2012). This then naturally reduces the accuracy of the solution with respect to the physical problem.

Large, complex computational domains in addition to transient solution procedures have led to numerous simplifying fluid-structure interaction assumptions for turbines in order to bring down the computational costs of the models (Alshroof *et al.*, 2012). Herein lies the challenge - producing a complete enough numerical model of a turbine stage to model the fluid-structure interaction while minimising computational costs and retaining accuracy. If this can be achieved and blade vibration can be detected in the flow field within the model, numerical prediction of the blades or stage status can be made. Coupling such a model with online vibration condition monitoring or some artificial intelligence system could provide the foundation of an advanced turbine condition prognostics tool.

1.2 Literature Review

The literature review aims to establish a framework for the research study by presenting specific topics in a logical order. The topics that will be covered in this review outline the focus areas of the intended study. The area of focus for this study is centred on investigating blade vibration and its relationship with the flow field through a steam turbine which is largely applicable to the power industry.

1.2.1 Steam Turbines Overview

This section of the literature review can be considered introductory and supplementary in light of the remainder of the topics that are covered. This section is included to remind the reader of certain terms and definitions regarding turbines and the associated vibrational characteristics.

1.2.1.1 Turbine Blade Vibration and Response Mechanisms

Turbine vibrations can be caused by a multitude of mechanisms including rotor and bearing imbalances, asymmetric flexibility and misalignment of the shaft, periodic loading, rotor blade damage and shaft whirl to name a few (Boyce, 2012). These vibrations can be classified into two main groups: synchronous or asynchronous vibration. The distinction between the two groups lies in the occurrence of the vibration being an integer multiple of the shaft rotational speed or not. This is known as engine-ordered vibration, or, synchronous vibration. The engine order, EO, is given by

$$EO = \frac{\omega_f}{\Omega} \tag{1}$$

where EO is the ratio of the excitation frequency, ω_f, to the rotational frequency of the shaft, Ω. Synchronous vibrations are caused by periodic aerodynamic loadings, which are inherent to the periodic internal geometry of turbines (Forbes and Randall, 2007). This is depicted in Figure 1.1 where the fluid flow interacts with the rotor blades and stator blades. The associated excitation frequency that is linked to the rotor blade passing the stator blades is called the stator passing frequency (SPF) and is generally of a higher EO. Synchronous vibrations could also stem from the mechanical effects such as unbalanced rotors and non-concentric casings and the associated pressure field fluctuations (Zielinski and Ziller, 2000). These effects produce excitation forces of lower EOs.

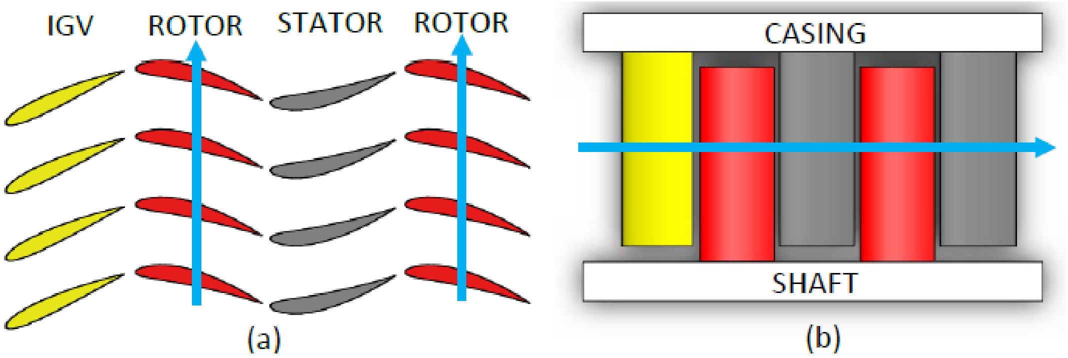

Figure 1.1. Turbine cross-section schematic. (a) Cascade view with blade rotation direction. (b) Meridional view with fluid flow direction (Church, 2016)

Asynchronous vibrations are non-integer multiples of shaft speed. These vibrations are usually triggered by rotating stall, blade flutter, occurring predominantly at a blade's natural frequency, and acoustic resonance (Zielinski and Ziller, 2000; Forbes and Randall, 2007).

Dimitriadis *et al.* (2002) noted that synchronous and asynchronous vibrations could occur close to each other in the frequency spectrum. Synchronous modes of vibration could coexist in a rotor stage as well as combined synchronous and asynchronous modes. This has made it important for turbomachine designers to design blades that have resonant frequencies that do not coincide with integer multiples of shaft speed during run-up and run-down of the turbomachine. This will however be inevitable as the turbine will most likely run past these critical speeds during start-up and shut-down of the turbomachine, but its effect can be limited by passing quickly over these speeds (Rao and Dutta, 2012). This will, however, lead to accumulation of fatigue damage of the rotor blades over time.

The root cause of blade vibration, in the context of damage, could be attributed to various mechanisms. The following are some of the most prevalent turbine steam path damage mechanisms: creep, solid particle erosion, low and high cycle fatigue (LCF & HCF), pitting, corrosion fatigue, stress corrosion cracking and liquid droplet erosion (McCloskey, 2002). According to McCloskey (2002), corrosion fatigue is one of the leading causes of damage in the rotor blades of steam turbines. It is a combination of alternating stresses and environmental effects. This mechanism usually originates from the presence of pitting or other localised erosion (McCloskey, 2002). This fault is then developed through cyclic stresses which lead to either corrosion fatigue or stress corrosion cracking.

1.2.1.2 Turbine Blade Vibration Modes

Before diving into the depths of analysing possible blade damage mechanisms, the vibrational response of an undamaged blade should first be understood. The basic mode shapes for turbine blades can be categorised as either bending, torsional or a combination of both (EPRI, 2008). The bending modes can be subdivided further into tangential, axial and second bending modes. The four fundamental mode shape classifications are outlined next in terms of simple blade geometries (EPRI, 2008; Schönleitner *et al.*, 2015):

1. *Tangential* – shown in Figure 1.2 (a). A flap-wise motion of the blade in the circumferential direction.
2. *Axial* – shown in Figure 1.2 (b). An edgewise motion of the blade in the flow direction.

3. *Torsional* – shown in Figure 1.2 (c). A twisting motion of the blade where the tip points are out of phase.
4. *Second bending modes* – shown in Figure 1.2 (d). A more complex flap-wise motion of the blade in the circumferential direction where the body and tip are out of phase.

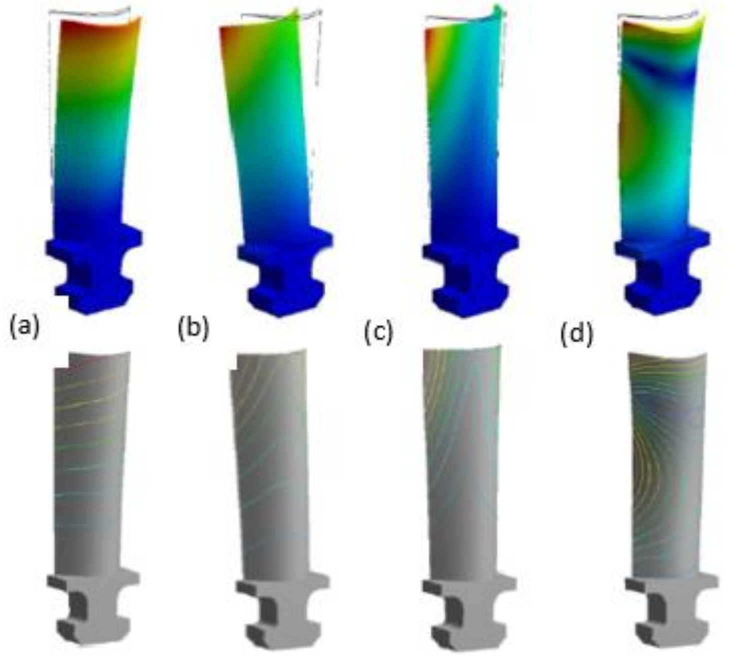

Figure 1.2. Fundamental mode shapes of turbine blade. (a) 1st flap-wise bending mode; (b) 1st edgewise bending mode; (c) 1st torsional mode; (d) 2nd flap-wise bending mode (Schönleitner et al., 2015)

In general, turbine blades are far more complex than the simple curved blade presented in Figure 1.2. The blades can contain tapering, twisting and complex airfoil cross-sections throughout the length of the blades, which also differ from stage to stage of large industrial turbines (Rao and Dutta, 2012). This results in complex mode shapes that appear as a combination of pure bending and torsional modes.

As mentioned before, fatigue – whether high cycle or low cycle – is a core turbine blade damage mechanism. Different modes of vibration result in significantly different stress distributions in the blades. A probabilistic investigation by Booysen (2014) on the fatigue life of low pressure (LP) turbine blades during start-up showed that the first bending mode had a considerable effect on the fatigue life of test specimens. These results emphasise that the lower modes of vibration are of interest which are also highlighted by Schönleitner *et al.*, (2015).

Related to the resonances of the vibrational modes of turbine blades, is the rotational speeds at which they occur. As mentioned previously, EO vibration is of interest as it is ever present in turbine operation. To explain this, the Campbell diagram is introduced. The Campbell diagram is a representation of the blade natural frequencies as a function of revolution harmonics (or engine orders) over a range of shaft speeds. The shifting of the natural frequency can be attributed to the stress stiffening caused by the operational speed (Mohan, Sarkar and Sekhar, 2014). Figure 1.3 shows an example of a Campbell diagram for an arbitrary blade for the first and second modes. The critical speeds of the system are then identified as the positions on the Campbell diagram where the mode natural frequency intercepts the EO lines.

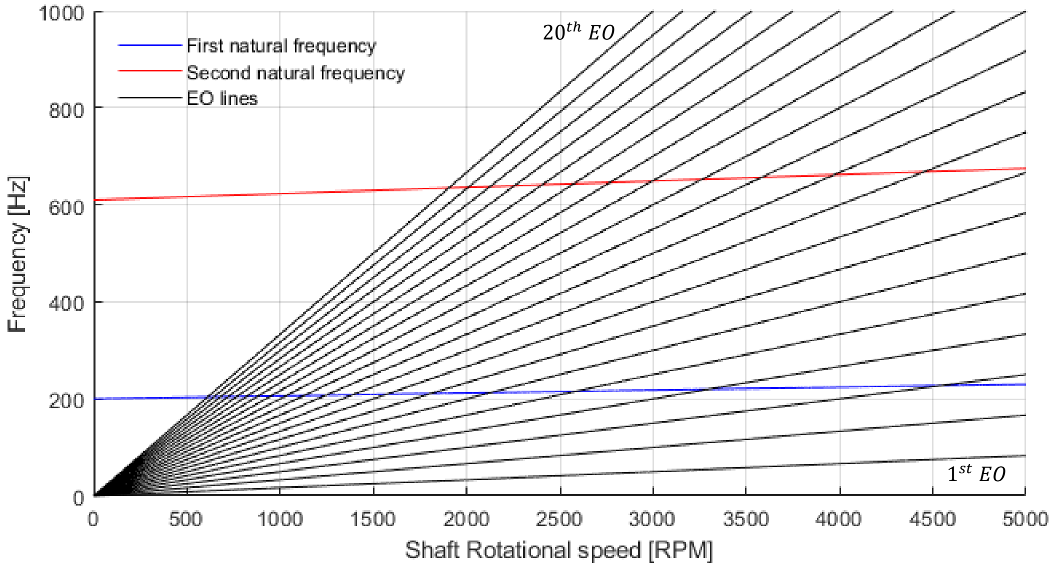

Figure 1.3. Campbell diagram for the first and second modes of a turbine blade

Generally, lower modes of vibration have higher associated energy whereas lower dynamic forces are produced at higher modes (Logan and Roy, 2003). The Campbell diagram can be used to predict natural frequencies of individual blades or groups of blades which are attached to rigid drum-type rotors when paired with a FE model, but this technique suffers from accuracy when more flexible rotors are used due to the structural effects (Logan and Roy, 2003). Tracking the change in vibrational frequencies of the blades could give insight to the health of the rotor blades. Thus, the next section covers vibration measurement techniques that utilise this feature on operating turbine blades.

1.2.2 Blade Vibration Measurement Methods

Blades are integral to the operation of any turbomachine. The vibrations they experience can cause severe damage to the machine. In the context of industrial use, this will put the health and safety of personnel at risk and hinder productive operation of the plant. It has been reported by Meher-Homji (1995) that 42% of gas turbine failures are caused by blade faults. Steam turbines are just as susceptible to blade failures – a survey performed in 1985 by EPRI (1985) reported that 75% of these blade failures occurred in LP turbines and that 30% thereof is contributed to HCF. Hence, many methods of detecting blade vibration have been developed and used over the years. These include the old work horse strain gauge measurement systems, dating back to the 1930s (Russhard, 2015), which are usually limited to the design phase of turbomachines (Forbes and Randall, 2013), and the non-intrusive family of measurement techniques such as that based on blade tip timing, casing pressure signal and casing vibration signal monitoring.

Turbine blade vibration is governed by aeroelastic effects of unsteady flow and the fluid-structure interaction effects of the high-velocity compressible fluid (Beauseroy and Lengellé, 2007). The vibrational characteristics - amplitude, frequency and phase - largely influence the fatigue life, performance and integrity of the turbomachine (Salhi *et al.*, 2008). The next few sections will cover the various well-known vibration measurement techniques that are used to extract blade vibration information.

1.2.2.1 Strain Gauge Measuring Technique

Usage of strain gauges to measure blade vibration is the conventional technique that forms part of the intrusive technologies (Agilis, 2014; Diamond and Heyns, 2018). Local deformation is measured through resistance changes in the strain gauge which transmits a signal related to the displacement to a fairly costly telemetry system (Beauseroy and Lengellé, 2007). The gauges are positioned at key points on the surface of the blades, typically at the root, as can be seen in Figure 1.4.

Strain gauge systems are reliable and produce accurate readings at light operating conditions (Russhard, 2015; Battiato, Firrone and Berruti, 2017) but, they do, however, suffer from a few drawbacks. Strain gauges are normally installed on a few blades only due to the high costs involved, the influence the routing wires have on the vibratory characteristics of the system and the time-consuming installation procedure (Beauseroy and Lengellé, 2007; Agilis, 2014; Diamond and Heyns, 2018). Another a drawback of using strain gauges is that each strain gauge can only collect vibrational data of the single blade that it is attached to which leaves the user with the issue of inferring vibrational information to non-monitored blades (Beauseroy and Lengellé, 2007).

In Industry, the use of strain gauges for measuring blade vibration is normally limited to the design phase of the turbine as their usable life is limited by exposure to harsh temperature and pressure conditions (Russhard, 2015; Du Toit, 2017). For academic research purposes, strain gauges are used in conjunction with other blade vibration identification techniques such as blade tip timing and these methods are subsequently used to cross-validate one another (Knappett and Garcia, 2008; Allport *et al.*, 2012; Battiato, Firrone and Berruti, 2017; Rigosi, Battiato and Berruti, 2017).

Figure 1.4. Typical rotor strain gauge installation (Adapted from Russhard, 2015)

1.2.2.2 Frequency Modulated Grid Systems

The Frequency Modulated Grid System (FMGS) was introduced by Bristol Siddeley Engines Ltd. in 1962 (Russhard, 2015). Stress in the rotor blade was quantified by indirect measurement of the blade tip displacement. The amplitude, a, and frequency, f, of the vibration were shown to be directly proportional to the maximum bending stress in the rotor blade. According to Russhard (2015), industry still uses the notion that the product af, which indicates a blade failure, is constant for any given material.

Permanent magnets are installed on the tips of a few blades with the receiver wires being embedded in the particular rotor stage's case. The rotation of the rotor induces an alternating current in the wire grid (Sabbatini *et al.*, 2012). The frequency of the induced signal is affected by blade vibrations which in turn cause frequency modulation that is directly proportional to the blade vibration constant, af.

By fitting multiple grids in the rotor path, data can be obtained from multiple points on the blade. This data can then be used to confirm the mode shapes and hence the vibrational characteristics at specific operating conditions (Russhard, 2015). Figure 1.5 shows a schematic of the FMGS. This method, as with the strain gauge method, imposes a few problems. The installation process is time-consuming and a complex process. The addition of magnets to the tips of the blades alter the vibrational characteristics of the blades and hinder the flow past the blades (Zielinski and Ziller, 2000).

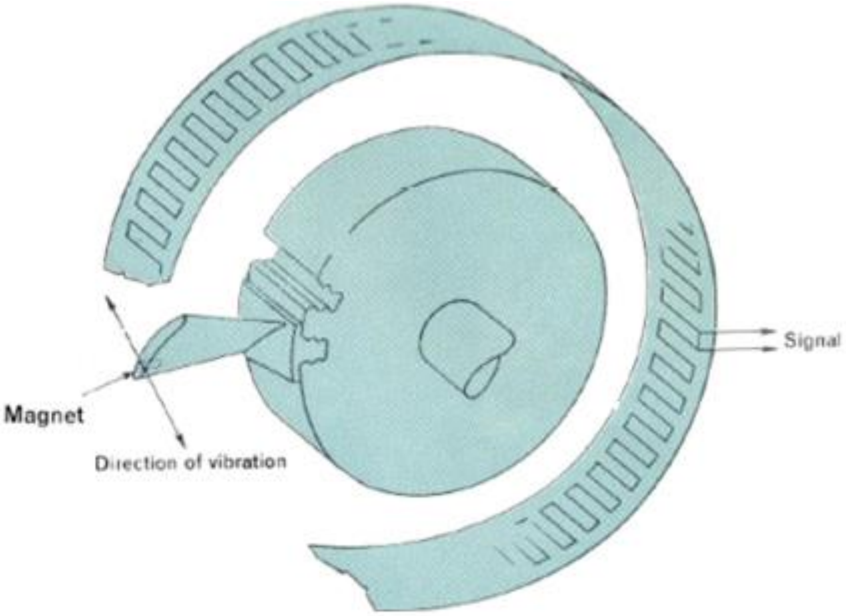

Figure 1.5. FM Grid arrangement (Russhard, 2015)

1.2.2.3 Blade Tip Timing Techniques

Blade tip timing (BTT) is a nonintrusive method of measuring turbomachinery blade vibration during operation that has been around since the 1970s (Rigosi, Battiato and Berruti, 2017). Due to the faster turbomachine development cycles, a decreasing trend in the use of strain gauge systems has been observed while BTT systems coupled with FE models have been receiving more attention (Russhard, 2015).

Blade tip timing utilises proximity sensors spaced circumferentially on the casing of a rotor stage (Diamond and Heyns, 2018). The proximity sensors are usually of the optical, magnetic, capacitive or inductive type (Dimitriadis *et al.*, 2002; Beauseroy and Lengellé, 2007). The time of arrival (ToA) of each blade is measured as it passes the proximity probe relative to a once-per-revolution (OPR) or multiple-per-revolution (MPR) shaft mounted encoder. A reference or expected ToA is calculated based on the shaft speed. Vibration of a blade will result in the blade arriving either earlier or later due to the deflected tip (see Figure 1.6). The blade tip displacement is calculated taking the difference of the two ToAs through

$$x = \Delta t \Omega \mathrm{R} \tag{2}$$

where x is the tip deflection, Δt is the difference in ToA, Ω is the shaft rotational speed and R is the outer radius of the rotor. Measurement data from several sensors can then be used to infer the blade vibration characteristics over multiples of shaft rotation (Diamond and Heyns, 2018). This is, however, notoriously difficult if the vibration is an EO of the shaft speed (Dimitriadis *et al.*, 2002). This is due to the blade tips having essentially the same displacement each time they pass the sensors while the system is running at constant speed and the resulting displacement data effectively repeats itself (Dimitriadis *et al.*, 2002).

Another shortcoming regarding the difficulty of post-processing BTT data is aliasing (Beauseroy and Lengellé, 2007). This is caused by the limitation in data acquisition sampling rate which is dependent on the rotational speed of the rotor, the number of sensors and the circumferential spacing between the probes around the rotor casing (Diamond and Heyns, 2018).

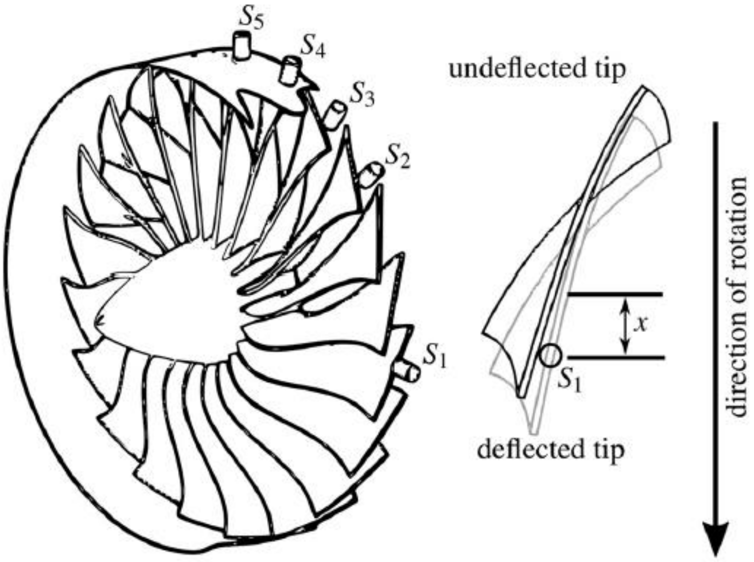

Figure 1.6. BTT principle: a compressor fan row with a sectioned casing showing five proximity probes (left); difference in time of arrival of tip of vibrating blade (right) (Diamond and Heyns, 2018)

A noticeable advantage that the BTT method has over the traditional strain gauge method - other than it being non-intrusive - is that all the blades on a rotor assembly can be monitored simultaneously (Rigosi, Battiato and Berruti, 2017).

1.2.2.4 Casing Pressure Signal and Casing Vibration Signal Methods

Forbes and Randall (2007) suggested that the measurement of the casing vibration could provide means of blade condition monitoring and modal parameter estimation, i.e. modal frequency, modal damping and mode shape. This led to the investigation of whether blade condition information could possibly be extracted from the casing vibration signal (CVS) and casing pressure signal (CPS) measurements.

Proof of Concept of CVS and CPS Measurement Method

An analytical model of the case vibration and simulated pressure signal associated with blade vibrations was presented by Forbes and Randall (2007). The formulation of the excitation forces comprised of those transmitted through casing attachments to the engine and running gear with the exclusion of any fluid flow effects. Hence, the fluid-structure interaction was completely uncoupled, i.e. the casing motion and pressure distributions did not influence each other.

A very general assumption is made that this static pressure force has a sinusoidal shape as the rotor blades act as simple oscillators. Blade motion causes phase modulation of the pressure peaks linked to each rotor blade. Essentially, the rotor blade vibration is modelled to vibrate about its equilibrium position in the rotating reference frame with the characteristics of the blade's forced response. The reader is suggested to see Forbes and Randall (2007) for the exact derivation of the analytical model constituents.

Verification of the analytical model is accomplished by comparing results to a very simplified FEA for different rotor speeds. The FE model had soft spring supports and damping added at the stator blade locations whereas the analytical model was based on free-free boundary conditions. The results showed that the analytical and FE model corresponded well. The natural frequency of the blade was chosen as 500 Hz and can be shown to appear in the spectral analysis plots shown in Figure 1.7.

The response showed peaks when the blade's natural frequency was traversed. This together with the validation of the FE model showed that the casing contains information about the vibrational characteristics of the rotor blade. This would allow for blade vibration monitoring through a non-intrusive technique whereby the casing vibrations could be used.

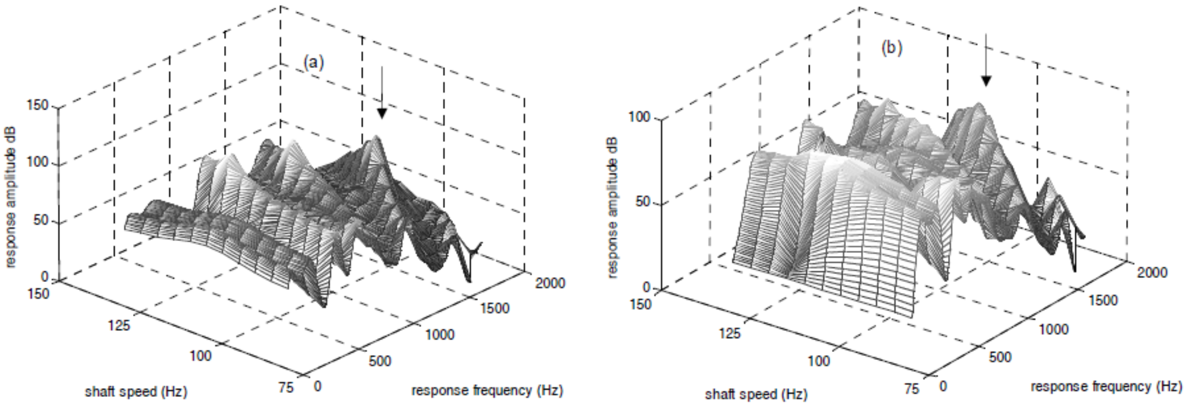

Figure 1.7. Radial casing response at shaft speed of 80 Hz: Analytical (left); FE model (right) (Forbes and Randall, 2007)

Forbes and Randall (2013) extended their investigations to estimate turbine blade natural frequencies from casing pressure and vibration measurements. Again, a simulated internal CPS was derived that included blade vibration effects. The work of Forbes and Randall (2013) was based on results seen in the work of Rao and Dutta (2010). Rao and Dutta (2010) found that the casing pressure spectrum contained sidebands around some multiples of shaft rotational speed at frequencies at which rotor blades of a simplified experimental setup were excited. The estimation of rotor blade natural frequencies by Forbes and Randall (2013) was based on the measurement of the aforementioned sidebands found in the vibration and pressure spectrum.

The updated analytical formulation included the fluid flow's turbulence effect on the pressure signal as a white random variable with zero mean as well as the influence of the blade's motion. Only the stochastic part of the pressure and casing vibration signals were used in the formulation. For further insight as to how the discrete portion of the signal was derived see Forbes (2010).

Experimental estimation of the blade natural frequencies was achieved through excitation of a single blade row in a simplified test rig. Among the collected data, a simulated faulty blade case was also investigated whereby a single blade of reduced thickness was inserted in the rotor. The rotor consisted out of 19 flat blades with the upstream stator being represented by 6 jets emitting high velocity air.

Overall, the CPS method presented by Forbes and Randall (2013) estimated the rotor blade natural frequencies relatively well in comparison to the analytically derived results. The estimation of these frequencies, however, depend on the knowledge of the natural frequency to within ± half of the shaft speed. The natural frequency of the single faulty blade was also estimated successfully. The work of Forbes and Randall (2013) presented the first non-intrusive method for turbine blade natural frequencies determination from CPS measurements taken at constant shaft operating speed.

CPS and CVS Signal Processing Methods

The method proposed here is based on the work of Forbes and Randall (2013) for constant shaft speeds. The analysis consists of the following steps:

1) *Order tracking of the raw sampled data*.
2) *Synchronous averaging of order tracked data*. Synchronous averaging allows for separation of the discrete and random parts of the signal including noise. This also allows for the determination of the average non-vibrating signal over a single shaft revolution. This process is repeated to form a full-length signal, namely, the deterministic signal. The stochastic signal is then constructed through the subtraction of the deterministic signal from the full order tracked signal. The spectrum of a separated deterministic and stochastic CVS is shown in Figure 1.8. The red lines are the deterministic portion of the signal and the stochastic portion is shown in blue.

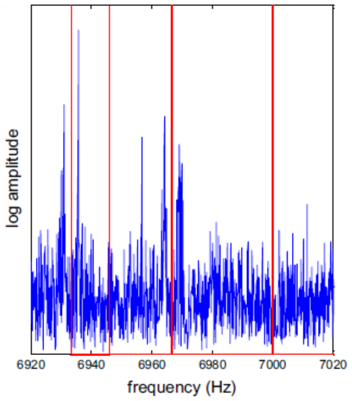

Figure 1.8. Stochastic and deterministic portions of casing vibration signal (Forbes and Randall, 2013)

3) *Ensemble averaging of pressure and vibration spectrum*. When viewing the spectrum, sideband peaks appear about the engine harmonics in the stochastic part of the signal (as seen in Figure 1.8). The engine harmonics are determined using the deterministic part of the signal as explained in step 2. The method presented by Forbes and Randall (2013) uses

a spectrum bandwidth of one shaft rotation, spanning from 0.5 to 1.5 multiples of shaft rotational speed. This process is similar to synchronous averaging of time domain signals. Figure 1.9 shows an ensemble average example. Ensemble averaging gives a robust estimate of the spacing between narrow band peaks in the pressure and vibration spectrums. This then allows for the estimation of the turbine blade natural frequency.

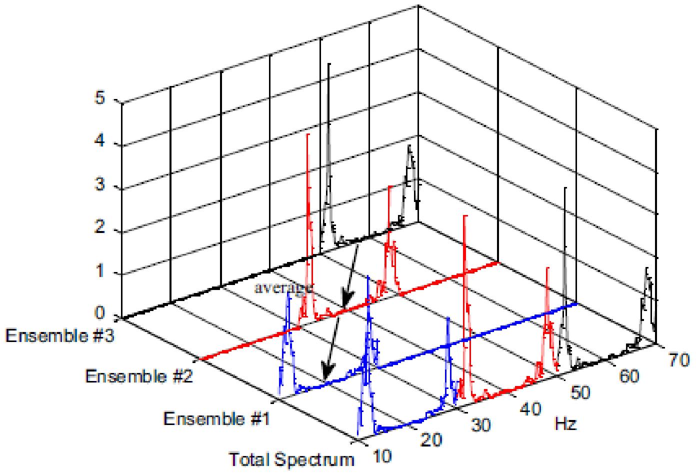

Figure 1.9. Ensemble averaging schematic (Forbes and Randall, 2013)

The blade natural frequency must be known to within ± half of the shaft rotational speed in order to estimate it (Forbes and Randall, 2013). Once this is known, the natural frequency can be calculated using the distance between the narrow band peaks as shown in figure 3.14. This is possible because the narrow band peaks lie at integer multiples of shaft speed ± the blade natural frequency. The blade natural frequency is estimated through the relation

$$f_{\tilde{n}} = \frac{\Delta f + (m - k)\Omega}{2} \tag{3}$$

and

$$\Delta f = (k\Omega + f_n) - (m\Omega - f_n) \tag{4}$$

where k and m are positive integers and $k < m$, Δf is the frequency difference of the sideband peaks and Ω is the shaft rotational speed. For visualisation of this method see Figure 1.10.

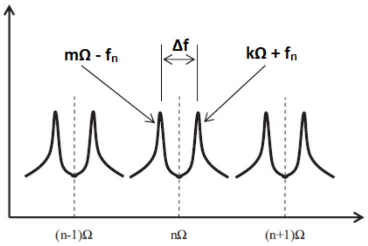

Figure 1.10. Schematic of narrowband peak harmonics and blade natural frequency (adapted from Forbes and Randall, 2013)

1.2.3 Modelling

Experimental procedures that measure turbine blade vibration as well as analyse the data have been discussed. Next, numerical modelling will be introduced to the reader. Numerical modelling in terms of the flow field through a turbine, the structural response of the blades as well as the fluid-structure interaction between the two domains will be discussed.

These models are commonly incorporated in studies along with experimental work and hence used to cross-validate each other. The discussion of this section will be focused on previous authors' work, although supplementary content will be provided regarding the underlying theory of the models especially in the case of the computational fluid dynamics.

1.2.3.1 Structural Aspects

Generally, only the turbine blades and rotor disks are modelled while excluding the casing and shaft geometries. The following section elaborates on the modelling of the turbine rotor blade and finite element modelling considerations.

Blade Profiles and Disk Configurations

The focus is placed here on LP steam turbines as they are quite commonly affected by their own vibration mechanisms but also that of downstream process equipment, such as condensers, in the power industry (Rao and Dutta, 2014). LP steam turbine blades are usually twisted and tapered from root to tip. Power utilities' LP turbine blades are generally of the impulse-reaction type (Eskom Holdings, 2019). The blades have an impulse-bucket shape at the root of the blade and twist through a changing cross-section to a reaction-type profile at the tip of the blade.

Modelling these highly twisted and tapered blades is quite challenging. Generally, if the CAD model of the blade is available, it might be seen that certain features such as the mounting bases and fillets are simplified and defeatured. This is done to avoid problematic meshing regions and to maintain mesh quality.

Finite Element Modelling and Associated Analyses

Structural modelling can be split up into two main categories when considering the turbine blade geometry. The basic type of analysis that should be carried out, either as validation or as part of a larger study, is the modal analysis. Modal analysis is used to determine the vibrational characteristics of a structure, i.e. natural frequencies and mode shapes. Modal analysis can be used as a starting point for a transient dynamic analysis. The basic form of the undamped modal analysis equation is given as

$$[\boldsymbol{K}]\tilde{\varphi}_i = \omega_n^2[\boldsymbol{M}]\tilde{\varphi}_i \tag{5}$$

where $[\boldsymbol{K}]$ is the global stiffness matrix, $[\boldsymbol{M}]$ is the global mass matrix, $\tilde{\varphi}_i$ is a mode shape vector of mode i and ω_n is the natural frequency of mode i. Equation (5) is also known as the classical eigenvalue problem which is derived from the equations of motion of a system. It is essential to know the natural frequencies and associated mode shapes in context of the dynamic environment of turbomachinery operating conditions. If the load frequencies coincide with the natural frequencies of the structure, resonance, and hence, failure can occur.

In the context of time-dependent loadings such as those encountered on turbine rotor blades, a transient dynamic analysis can be undertaken. Through this analysis, the displacement, stress and strain of the structure can be determined. The basic equation of motion for a MDOF is given by

$$[\boldsymbol{M}]\ddot{\tilde{u}} + [\boldsymbol{D}]\ddot{\tilde{u}} + [\boldsymbol{K}]\tilde{u} = \tilde{F}(t) \tag{6}$$

where $[\boldsymbol{M}], [\boldsymbol{D}]$ and $[\boldsymbol{K}]$ are the mass, damping and stiffness matrices, $\tilde{u}, \ddot{\tilde{u}}$ and $\ddot{\tilde{u}}$ are the displacement, velocity and acceleration vectors and $\tilde{F}(t)$ is the generalised time-dependent force vector. This system is discretised into elements and solved using the finite element method (FEM).

Geometrically Linear vs Nonlinear Formulations

It is important to know the envelope of the problem that is being dealt with. In the case of rotating turbomachinery blades, one would expect the vibration amplitude far under the $10mm$ mark. Modelling these vibrations is challenging as one does not know beforehand what displacements to expect and how significant they are with regard to size of the blade. In FEM, geometrically linear solvers can accommodate small structural displacements, whereas geometrically nonlinear solvers can accommodate large and small displacements, with the latter being computationally more expensive. This is an important consideration then not only from an accuracy point of view, but also a computational effort perspective.

1.2.3.2 Flow Aspects

Flow, in general, can be categorised into three major groups - laminar, transitional and turbulent. The flow regime can be identified by the dimensionless Reynolds number given by

$$Re = \frac{\rho|V|L}{\mu} \tag{7}$$

where ρ is the fluid density, $|V|$ is the velocity magnitude, L is the characteristic length and μ is the dynamic viscosity. The Reynolds number is physically interpreted as the ratio of the inertial forces to the viscous forces. A “high” and “low” Reynolds number has different orders of magnitude for different applications where for example, flow through a pipe is considered turbulent for a Reynolds number of 2300. Flows in turbomachines are predominantly turbulent and viscous due to the complex flow paths, but laminar and transitional regions can exist within the turbines (Logan and Roy, 2003).

In general, the mass, momentum - Navier-Stokes Equations (NSE) - and energy conservation equations must be solved to fully describe the fluid flow and heat transfer involved. The full set of conservation equations in their various forms and the associated derivations can be found in reference sources such as Chung (2009), ANSYS (2018) Fluent theory guide and Henningson and Berggren (2005) for more detail pertaining to the derivations. The governing equations are given next using Einstein summation convention.

Conservation of mass, or the continuity equation, is given by

$$\frac{D\rho}{Dt} + \rho\frac{\partial u_k}{\partial x_k} = 0 \tag{8}$$

where $\frac{D\rho}{Dt}$ is the total derivative of density with reference to space and time, u_k is the velocity component in the spatial direction k and x_k is the spatial direction. The three-dimensional momentum conservation equations are given compactly as

$$\rho \frac{\partial u_i}{\partial t} + \rho \left(\frac{\partial u_i u_j}{\partial x_j} \right) = -\frac{\partial p}{\partial x_i} + \frac{\partial}{\partial x_j} \tau_{ij} + \rho g_i + F_i \tag{9}$$

where p is the static pressure, τ_{ij} is the viscous stress tensor, and ρg_i and F_i are the body forces and externally exerted forces, respectively. The stress tensor τ_{ij} is given by

$$\tau_{ij} = \mu \left(\frac{\partial u_i}{\partial x_j} + \frac{\partial u_j}{\partial x_i} - \frac{2}{3} \frac{\partial u_k}{\partial x_k} \delta_{ij} \right) \tag{10}$$

and δ_{ij} is Kronecker's delta. The energy conservation equation is given by

$$\rho \frac{De}{Dt} = -p \frac{\partial u_i}{\partial x_i} + \frac{\partial}{\partial x_i} \left(k \frac{\partial T}{\partial x_i} \right) + \Phi \tag{11}$$

where $\frac{De}{Dt}$ is the total derivative of internal energy, k is the thermal conductivity which is usually a function of temperature and Φ is the positive definite dissipation function defined as

$$\Phi = \tau_{ij} \frac{\partial u_i}{\partial x_j} = \mu \left[\frac{\partial u_i}{\partial x_j} + \frac{\partial u_j}{\partial x_i} - \frac{2}{3} \left(\frac{\partial u_k}{\partial x_k} \right)^2 \right] \tag{12}$$

Equation (12) is defined using the assumption of a Newtonian fluid, i.e. the shear stress is proportional to the velocity gradient of the fluid.

It is well known that the NSE are one of the millennial problems as it has not been proved that a smooth solution always exists, and if it does, that they have bounded energy, i.e. that the solution is unique. Hence, the careful use of numerical models to model certain features or groups of features of fluid flow, each with their own set of assumptions which is especially important in turbulence modelling. These equations are solved similar to structural problems by discretising the domain, but under the broad spectrum of computational fluid dynamic methods available. These include finite difference methods, finite volume methods and control volume finite element methods.

Turbulence Modelling

Unsteady flow field fluctuations in time and space over many different scales are characteristic of real turbulence. In reality, turbulent flows would involve turbulent time and length scales that would be significantly smaller than the smallest practically generated finite volume mesh. Direct numerical simulation of the conservation equations has been performed academically for low-Reynolds number flows over flat plates, LP and HP turbines and other turbomachinery components. Although it has far superior accuracy, it is too computationally expensive for general engineering flows due to it resolving all scales of turbulent fluctuations (Argyropoulos and Markatos, 2015; Pichler *et al.*, 2016).

This brought the need for modelling turbulent flows through turbulence models. A commonly used turbulence model for industrial flows is the Reynolds-averaged Navier-Stokes (RANS) model in its various forms. RANS models do not resolve the small-scale fluctuations but rather model the effect the turbulence has on the flow through averaging. For RANS models, the solution variables of the instantaneous NSE are split into the mean (time-averaged) and fluctuating components. For scalar quantities such as velocity components, pressures and temperatures this can be represented as

$$\psi = \bar{\psi} + \psi' \tag{13}$$

where $\bar{\psi}$ is the mean component and ψ' is the fluctuating component. This gives rise to new terms which represent the effects of turbulence in the flow. Substituting the variables in the Cartesian tensor form of the momentum equation (16) and dropping the overbar on the mean velocity, $\bar{u}$, gives

$$\frac{\partial}{\partial t}(\rho u_i) + \frac{\partial}{\partial x_j}(\rho u_i u_j) = -\frac{\partial p}{\partial x_i} + \frac{\partial}{\partial x_j}\left[\mu\left(\frac{\partial u_i}{\partial x_j} + \frac{\partial u_j}{\partial x_i} - \frac{2}{3}\delta_{ij}\frac{\partial u_k}{\partial x_k}\right)\right] + \frac{\partial}{\partial x_j}\left(-\rho\overline{u_i'}\overline{u_j'}\right) \tag{14}$$

where δ_{ij} is again Kronecker's delta. Equation (14) can be rewritten to account for variable density flow as well (see Favre-averaged NSEs in ANSYS, 2018). The term $\rho\overline{u_i'}\overline{u_j'}$ has been dubbed Reynolds stresses and can be modelled in various ways. One way of modelling these turbulence-induced stresses is to apply the Boussinesq hypothesis to relate the Reynolds stresses to the mean velocity gradients through the relation

$$-\rho\overline{u_i'}\overline{u_j'} = \mu_t\left(\frac{\partial u_i}{\partial x_j} + \frac{\partial u_j}{\partial x_i}\right) - \frac{2}{3}\left(\rho k + \mu_t\frac{\partial u_k}{\partial x_k}\right)\delta_{ij} \tag{15}$$

where μ_t is the turbulent viscosity and k is the turbulent kinetic energy. A disadvantage of using the Boussinesq hypothesis is that μ_t is assumed as an isotropic quantity, which may not always be the case (ANSYS, 2018d). It can, however, work well in cases that are dominated by only one of the turbulent shear stresses which, according to ANSYS (2018a), covers most technical flows. An alternative method to the Boussinesq approach is to solve the transport equations in terms of the Reynolds stresses which is known as the Reynolds Stress Model, but is not part of the scope of this study (see ANSYS, 2018b, p. 42).

Arising from Equation (15) is the turbulent kinetic energy and turbulent viscosity, both of which also need to be modelled appropriately. Hence, the introduction of two variants of the RANS model that are used widely in industry for many different types of engineering flow calculations due to their robustness, economy and reasonable accuracy (ANSYS, 2018d). These are the $k - \varepsilon$ and the $k - \omega$ models. Both models have modified versions, whereby various other flow effects are included in the transport equations, which have been brought about over the years.

Both the $k - \varepsilon$ and the $k - \omega$ models relate the Reynolds stresses to the mean velocity gradients and the turbulent viscosity. These models differ by the way in which the turbulent viscosity is calculated. The turbulent viscosity for the $k - \varepsilon$ model is linked to the turbulent kinetic energy and dissipation rate through the relation

$$\mu_t = \rho C_\mu \frac{k^2}{\varepsilon} \tag{16}$$

where C_μ is a constant quantity computed from strain rates and other model constants and ε is the turbulent energy dissipation rate. Both k and ε are included in the transport equations that also need to be solved for (ANSYS, 2018b, p. 81). The turbulent viscosity for the $k - \omega$ model is linked to the turbulent kinetic energy and turbulent frequency through the relation

$$\mu_t = \rho\frac{k}{\omega} \tag{17}$$

where ω is the turbulent frequency. Both k and ω are included in the transport equations that also need to be solved for (ANSYS, 2018b, p. 84). More specifically, the realizable $k - \varepsilon$ and shear stress transport $k - \omega$ models have become the work horses of industry (ANSYS, 2018c, p. 96). More detail pertaining to which turbulence models were used in this study will be presented in section 3.1.

Near-wall Treatments

Turbulent flows are significantly affected by the presence of walls. In the near-wall region, the solution variables have large gradients. This makes it important for having an accurate representation of the flow in the near-wall region. A commonly used approach for modelling the wall bounded turbulent flow is to use a set of semi-empirical formulas called *wall functions*, which are used to link the viscosity-affected region between the wall and fully turbulent region. This avoids having to resolve flow in the boundary layer and thus saves computational resources (ANSYS, 2018a, p. 172).

As the viscosity-affected region and fully turbulent region will be modelled differently, a link to the boundary between these two regions was developed as a dimensionless distance from the wall known as the y^+ value given by

$$y^+ = \frac{\rho \, \Delta y \, u_\tau}{\mu} \tag{18}$$

and

$$u_\tau = \left(\frac{\tau_\omega}{\rho}\right)^{\frac{1}{2}} \tag{19}$$

where u_τ is the friction velocity at a distance of Δy from the wall and τ_ω is the wall shear stress. The y^+ value can be viewed as a local Reynolds number. The sought y^+ value for a CFD simulation is dependent on the type of simulation (flat plate flow, turbomachinery blades, heat transfer, etc.), the turbulence model used and whether a wall function is used or not. The y^+ value is used to set the first cell height normal to the wall.

The shear stress transport $k - \omega$ model (SSTKO) of CFX employs an automatically switching near-wall treatment depending on the calculated y^+ value. A switch is made between a wall-function and low-Re number formulation to smoothly resolve the boundary layer (ANSYS, 2018a).

To ensure proper mesh refinement in the boundary layer, TurboGrid - the meshing software used for the fluid domain, allows one to set a y^+ value based on an inflow Re number to compute the near wall spacing of the mesh. This ensures an appropriate number of nodes in the boundary layer and thus a reduction in errors offered by the automatic switching near-wall treatment method.

Mesh Quality

Mesh quality is important in both FEA as well as CFD studies. It will be discussed briefly here in context of a three-dimensional fluid domain, but it can be directly applied to a structural mesh. Many mesh quality metrics exist, therefore a few key metrics will be outlined below.

The first metric, *face angle*, is calculated as the angle of the two edges that touch a node for each face. The maximum face angle can be considered to be a measure of skewness. A face angle of 90° would be ideal for all elements but this would not be possible to achieve throughout the entire mesh of a turbomachine passage. Staying within the limits of $15°$ and $165°$ is generally an indication of a good quality mesh (ANSYS, 2018e).

The second metric, *edge length ratio*, is the ratio of longest edge of a face to the shortest edge of a face. For each face,

$$\frac{\max(l_1, l_2)}{\min(l_1, l_2)}$$

is calculated for the two edges of the face that touch a node. The edge length ratio can be considered to be a measure of aspect ratio. A generally accepted value for the edge length ratio is 1000 in the case of a smooth transitioning mesh (ANSYS, 2018e). For complex cavities as well as fluid domains around highly twisted blades, lower edge length ratios are sought.

Lastly, the *element volume ratio* is the ratio of the maximum element volume that touches a node to the minimum element volume that touches a node. This can be used as a measure of local expansion factor. An acceptable limit on this metric is 20 (ANSYS, 2018e). In high curvature areas, one would need to limit the element volume ratio, as with the *edge length ratio*, to capture the domain correctly. Larger element volume ratios are thus less problematic in large planar regions.

The type of mesh employed is very important when it comes to any type of numerical simulation as it is directly linked to solving time and numerical accuracy. Unstructured meshes, such as tetrahedral meshes, offer flexibility when it comes to complex domains. Structured meshes on the other hand, offer higher numerical accuracy and require less storage space than an unstructured mesh (Ali *et al.*, 2016). Topology blocking along with a structured mesh is a mainstream meshing approach to many flow simulations carried out recently (Ali *et al.*, 2016). Partitioning a complex domain allows for better mesh quality as the simpler sub-domains are meshed more easily with a structured mesh. The meshing approach of this study is elaborated on in section 3.1.1 of the Numerical Model chapter.

Mesh Independence and Convergence

As with any numerical method, whether spatially- or time-discretised, there exists an error caused by the discretisation of the scheme. This makes it necessary for grid convergence studies or some type of uncertainty estimation of the solutions obtained from CFD in order to test mesh-independence of the solutions. According Roache (1994), *"systematic grid refinement studies are the most common, most straightforward and arguably the most reliable".* Roache (1994) proposed the use of a grid convergence index (GCI) for the uniform reporting of grid refinement studies. This would allow for the estimation of the grid convergence accuracy of a particular discretised solution. This method is outlined below.

Through Richardson Extrapolation, the pth-order discrete solution h is given by

$$h_{exact} \cong h_1 + \frac{h_1 - h_2}{r^p - 1} \tag{20}$$

where h_1 and h_2 are the discrete solutions of two different uniform grid spacings (with h_1 relating to the fine grid) and r is the grid refinement ratio in terms of the spacings of the two grids. This extrapolation is generally $(p + 1)$ order accurate. The order of convergence, p, is calculated as

$$p = \frac{\ln\left(\frac{h_3 - h_2}{h_2 - h_1}\right)}{\ln(r)} \tag{21}$$

where h_1, h_2 and h_3 are the performance parameters ranging from a fine to coarse grid. The GCI for three solutions can be expressed as

$$GCI_{12} = \frac{F_s \left|\frac{h_2 - h_1}{h_1}\right|}{r^p - 1} \tag{22}$$

and

$$GCI_{23} = \frac{F_s \left|\frac{h_3 - h_2}{h_2}\right|}{r^p - 1} \tag{23}$$

where F_s is a safety factor of 1.25 when a minimum of three solutions are available and 3 if only two mesh refinements are available. If three refinements are performed and

$$\frac{GCI_{23}}{r^p GCI_{12}} \approx 1, \tag{24}$$

then mesh independence is achieved and the solution is in the asymptotic range of convergence. In the case of two-grid refinements, the GCI can be converted to a percentage

$$GCI_{12} = x\ [\%] \tag{25}$$

resulting in the performance parameter, h, being within x-percent of the exact value. This is based on empirical studies by Roache (1994) that suggest a confidence interval of 95% is applicable.

Furthermore, this method can be extended to FEM solutions as well as either finite volume methods or finite difference methods. It is extremely important in the author's opinion to ensure that mesh-independent solutions are obtained. Discretisation error will always be present, and hence the need to minimise it as far as practically possible, especially in the case that two numerical solvers, in the fluid domain and structural domain, will have crosstalk of information between each other and hence these errors will be carried back and forth between the solvers.

Temporal Discretisation Independence

The Courant number or CFL (Courant-Friedrichs-Levy) number is of vital importance for transient flow analyses. This non-dimensional number for a one-dimensional grid is calculated using

$$CFL = \frac{u\Delta t}{\Delta x} \tag{26}$$

where u is the fluid speed, Δt is the timestep and Δx is the mesh size. For a fully explicit solver, the $CFL = 1$ condition is usually imposed to ensure stability of the solution (ANSYS, 2018b).

CFX calculates the CFL number based on a multidimensional generalisation of equation (26) by using a velocity and length scale based on the mass flow into a control volume and the dimension of the control volume (ANSYS, 2018b). CFX, however, makes use of an implicit solver and hence does not require the CFL number to be small for stability purposes (ANSYS, 2018b), especially in the case of RANS models being used where small-scale transient fluctuations are not resolved.

For the purpose of a timestep independence study, similar to the grid independence study, the CFL number can still be used to determine the time step size required for an accurate solution when using uniformly sized timesteps.

1.2.3.3 Fluid-structure Interaction Modelling

Many studies on turbine blade vibration incorporate a FE model coupled with either an analytical model (Forbes and Randall, 2007) or experimental studies (Heinz *et al.*, 2010; Ratz, Forbes and Randall, 2013; Drozdowski *et al.*, 2016; Lin *et al.*, 2016, as examples). CFD studies regarding turbulence modelling of the flow within turbines are usually conducted with experiments (Denton, 2010; Zhang, He and Stüer, 2012; Megerle, 2014; Argyropoulos and Markatos, 2015, as examples).

Many engineering problems can be defined by multiphysics phenomena (Benra *et al.*, 2011), but are usually solved separately in each domain due to the computational costs involved with the transferring of data between the solvers for general engineering problems (Alshroof *et al.*, 2012). Benra *et al.* (2011) describe this multiphyiscs phenomena in terms of fluid-structure interaction (FSI) as the interchange of flow effects on a body and the structural motion effect of the body on the flow. This is achieved through the passing of boundary conditions from one domain to the other at each computational step (Alshroof *et al.*, 2012).

A FSI problem can be solved in two ways: using a monolithic or partitioned approach. A monolithic approach involves the simultaneous solving of the flow and structural equations such that their mutual influences are taken into account directly, which helps with stability of the solution (Degroote, Bathe and Vierendeels, 2009). The monolithic approach is more robust than the partitioned approach but is more computationally expensive. In a partitioned approach, the flow and structural equations are solved separately, negating the influence on each domain whilst the solving of each of the domains is underway (Degroote, Bathe and Vierendeels, 2009). This makes it necessary for the partitioned approach to have some type of coupling algorithm for the interaction of the two domains and to provide a coupled solution. Partitioned methods are subdivided further into one-way and two-way coupling. In one-way coupling, the fluid pressure for instance, acting on the structure is transferred to the structural solver. Two-way coupling involves the transfer of the structural displacement to the fluid solver as well (Benra *et al.*, 2011). Two-way coupling can then be subcategorised into weak and strong coupling. Benra *et al.* (2011) highlight the differences between weak and strong two-way coupling. Some general advantages and disadvantages of one-and two-way coupling methods are outlined by Benra *et al.* (2011):

1. Two-way coupling is generally more accurate, especially when geometric nonlinearities, i.e. large deflections, are present
2. Energy conservation is ensured by two-way coupling, but not necessarily by one-way coupling
3. One-way coupling simulations have much lower computation times
4. Mesh quality is preserved in one-way coupling as the deformation of the fluid mesh does not need to be calculated

Numerical investigations of the fluid-structure interaction of turbine flow and blade motion are usually limited to investigations of blade flutter (Forbes, Alshroof and Randall, 2011). The majority of these investigations make use of one-way coupling between the fluid and structural solvers such as that by Rama and Dutta (2014) and Alshroof *et al.* (2012). There have however, been investigations involving two-way coupling such as that by Forbes, Alshroof and Randall (2011), Zhang *et al.* (2011) and Ubulom, Neely and Shankar (2017).

The work of Forbes, Alshroof and Randall (2011) investigated whether the pressure profile around the rotor blades follows blade motion whilst they oscillate around their equilibrium position. A secondary investigation considered the difference between using one-way and two- way coupled solvers. The simulations were conducted using a simplified pseudo two-dimensional flow-scenario of a single blade modelled with one degree of freedom and a single stator blade passage. The SSTKO turbulence model was used to model the flow.

The change in pressure over time at a specific pressure tap location on the blade is shown in Figure 1.11. Both pressure profiles have the same trend although they are different in magnitude. This could be due to the incorrect aerodynamic damping lacking in the one-way coupled case. It was cautiously concluded that the rotor blade pressure profile follows the blade motion. The authors, however, recommended longer computation time to obtain complete convergence to the quasi-steady state solution as well as refining the CFD Mesh.

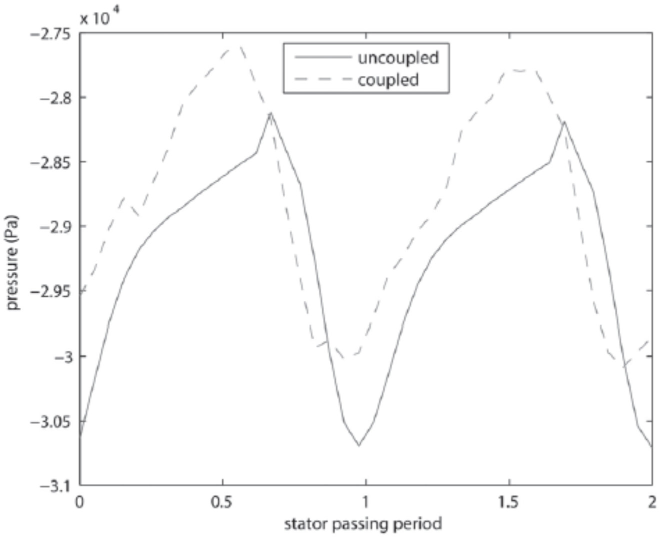

Figure 1.11. One-way and two-way case pressure over two stator passing periods (Forbes, Alshroof and Randall, 2011)

Rama and Dutta (2014) investigated self-excitation of long steam turbine blades during low load and high back pressure operating conditions. Self-excitation of the blades was modelled through the change in steam inlet angle to the blades. During low steam flow the steam inlet flow angle on the blade is larger than during normal operation (Rao and Dutta, 2014). The larger angle of the steam inlet flow causes flow separation over the blade leading to stall flutter.

A single blade was modelled with a rectangular fluid domain surrounding the blade in three dimensions. The fluid and structural meshes were generated independently without common nodes at the fluid-structure interface. This was done to simplify modelling and allow for large displacements without mesh distortion. The fluid domain was solved for first with the structural domain solved next with the transfer of the fluid solution, hence a one-way coupled approach.

Figure 1.12 shows the gross oscillatory nature of the turbine blade at different steam flow inlet angles. Larger inlet angles lead to larger amplitudes of vibration and hence more severe self-excitation as in the case of low load and high back pressure operating conditions. This serves as an example of a complex phenomenon - self-excitation of turbine blades - that can lead to damage of the blades, which was successfully modelled. The importance of fluid-structure interaction is highlighted here.

Ubulom, Neely and Shankar (2017) analysed the influence of varying levels of coupling (two-way and one-way coupling) on the high-cycle fatigue life estimation of a turbine blade. For the one-way coupled case, the fluid domain was solved prior to solving blade displacements and superimposed on the FSI interface of the blade.

The study showed a stronger influence of aerodynamic damping on the predicted stress response from the two-way coupled case, with a lower fluctuating stress amplitude as compared to the one-way coupled case. Ubulom, Neely and Shankar (2017) stated that the exclusion of the interaction of the structural blade motion and aerodynamic flow field neglects potentially more dangerous aeroelasticity issues including flutter and limit cycle vibrations, which are key components of HCF failure modes. The one-way analysis could potentially not capture these problems as they are highly dependent on modal instability and energy exchange between the two domains (Ubulom, Neely and Shankar, 2017). The authors concluded that a decoupled, or one-way coupled, approach to FSI is highly conservative and that much economic benefit can be attained through full two-way coupled analyses when predicting high cycle fatigue.

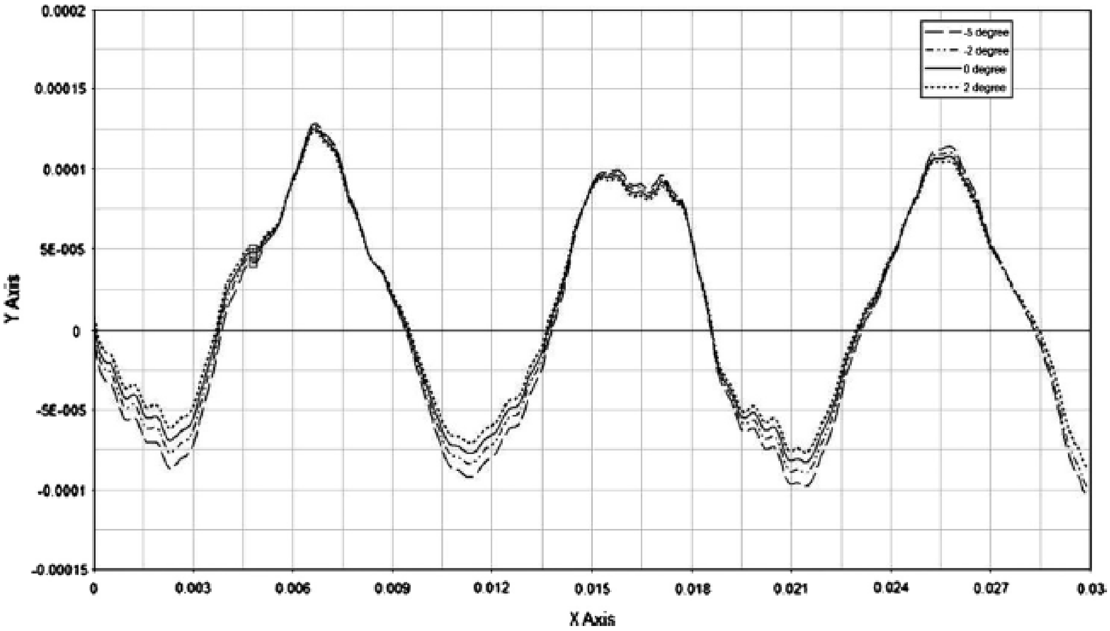

Figure 1.12. Increase in blade vibration amplitude at different inlet flow angles over time (Rama and Dutta, 2014)

The work of Alshroof *et al.* (2012) was a continuation of the study by Forbes, Alshroof and Randall (2011). This study presented a "tuned" three-dimensional one-way FSI model of a vibrating turbine blade. This one-way model enforced blade motion onto the fluid domain. The computational domain was limited to a single rotor blade passage comprised of approximately 1.2 million cells and took roughly four weeks to simulate. The investigation sought to quantify the relationship of the pressure at the turbine casing surface and the vibrating blade motion by varying the distance between the casing and the blade tip. The secondary objective was to investigate if the pressure profile around the rotor blade followed its vibratory motion. The model developed by Alshroof *et al.* (2012) is believed to have the computational efficiency of a moving boundary CFD model.

The results obtained show that the pressure distribution at the casing surface does not differ significantly, in its general form, from the pressure at the vibrating rotor blade tip. In fact, these pressure distributions are almost identical for the first spatial harmonic of the pressure distribution. The difference exists due to the flow leakage at the tip of the blade inducing vortices. This difference becomes more apparent as the clearance distance increases as seen in Figure 1.13.

These results coincided with the enforced motion of the rotor blades and it was concluded that the pressure profile around the rotor blades follow its motion. This is a similar conclusion by Forbes, Alshroof and Randall (2011) with the investigation of their 2D two-way FSI model.

A need for further work was realised as this study made use of a unity pitch ratio, which is not a realistic representation of a physical turbine, and only small dynamic blade deflections were investigated.

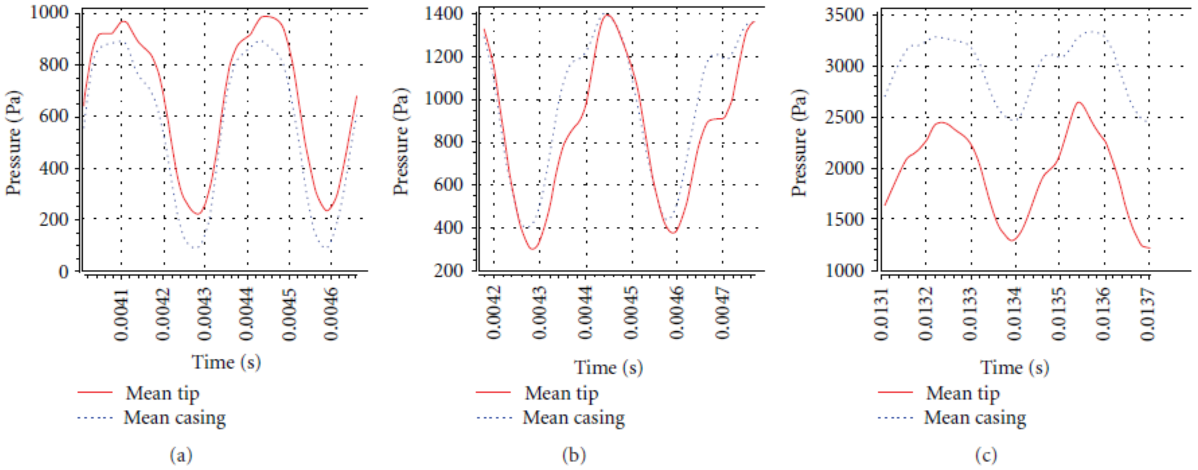

Figure 1.13. Pressure distributions over time at the casing and blade tip for (a) 0.5 mm, (b) 1.0 mm and (c) 1.5 mm gap (Alshroof et al., 2012)

The investigation by Alshroof et al., (2012) portrayed the importance of reducing the computational domain by enforcing a one-way structure-fluid interface. These results showed that it is possible to capture blade motion in the pressure field around a rotor blade and even at the casing of the turbine. This type of blade motion is essentially flow-induced vibration and one can use this data to identify significant frequencies in the associated spectra. As damage will alter the natural frequency of the blade, one can then track these changes in the frequency domain using the pressure profile.

1.3 Problem Statement and Objectives

Blade vibration condition monitoring is capable of indicating blade damage through the correct signal processing techniques. The motion of the blades is a direct result of fluid-structure interaction and therefore makes it an attractive avenue of investigation through numerical modelling.

The following void has been identified from literature: establishing a relationship between rotor blade damage and the pressure field of a fluid-structure interaction model of a steam turbine stage while minimising the computational effort.

The aim of this study is to establish to what extent the flow field of a three-dimensional two-way fluid-structure interaction model of a turbine stage can be used to extract blade vibration information. The results from this research study are applicable to the power industry.

1.4 Scope of Research

The key question that will be addressed throughout this research dissertation is:

To what extent can we link turbine blade response information to the pressure field when modelling the fluid-structure interaction of the flow through a turbine stage?

The outcomes of this study are to develop a three-dimensional two-way fluid-structure-interaction model of a single stage turbine passage that,

1. Can be used to investigate blade vibration in the pressure field
2. Is computationally efficient while retaining accuracy
3. Is validated against an experimental model

4. Is developed using commercial code, specifically the multiphysics environment of ANSYS Workbench (R2 2019) where ANSYS Mechanical is used for the structural domain and ANSYS CFX is used for the fluid domain.

The exclusions of the study are outlined below:

1. A numerical model of the full annulus of a turbine stage. Reduced geometry will be exploited where possible to reduce computation time.
2. An analytical model will not be developed, nor will an existing analytical model be used for comparison. The analytical model referred to is that which describes a pressure field including effects of blade vibration.
3. New signal processing techniques as well as modifying existing signal processing techniques. The aim of the study does not focus on signal processing, but it will form part of the experimental work to validate the numerical model. Thus, the simplest techniques will be used.
4. Damage classification. The aim of the study is to extract blade vibration information out of a FSI pressure field. The blade vibration can be linked to any type of damage, or even flow induced flutter.

The contribution, in short, will be an investigation into the extent that blade damage information can be obtained from the pressure field of a two-way fluid-structure interaction model of a steam or gas turbine stage, while sensibly minimising computational costs.

1.5 Document Overview

The remainder of the document is broken up into four sections that are briefly described below.

Chapter 2 presents the experimental testing section of this study. The vibration measurement techniques are shown along with the static modal analysis results of the rotor blades and some preliminary post-processing of the data.

Chapter 3 presents the numerical model. In this section, the geometry, mesh, boundary conditions and materials are discussed as well as key settings used for the fluid and structural solvers. This chapter also supplies investigations for mesh independent solutions, timestep size selection and solver type selection for the fluid and structural domain. The chapter is concluded with a section on how the FSI model is set up with a short section on how solver coupling, and fluid mesh deformation is handled in ANSYS.

The discussion of all the FSI simulation results are presented in Chapter 4. This section is split up into three investigations, namely, uncertainty quantification of the measured stage inlet velocity; a healthy rotor blade analysis; and a supplementary damaged rotor blade analysis.

The study is concluded in Chapter 5 and recommendations are listed for future work on this topic. Four appendices are included at the end of this dissertation that contain,

- the computational solve times for the FSI simulations,
- supplementary modal analysis data,
- additional FSI simulation data,
- and drawings for the experimental set up of the test turbine.

2 Experimental Testing

This chapter presents the experimental part of the study. The intention of performing experiments was to validate the numerical model. A key area of concern was the detection of the change in pressure at the rotor blade's tip. The casing vibration was also measured as a supplementary dataset.

2.1 Layout and Equipment

The test bench consisted of a single turbine stage - an upstream stator blade row and a rotor blade row. Due to air pressure supply limits, the turbine rotor was not powered by airflow. Instead, air was passed over the stator blades through a circular arrangement of nozzles inside the turbine casing, from a high-pressure air supply while an electric motor was used to turn the rotor assembly. The test bench can be viewed in Figure 2.1.

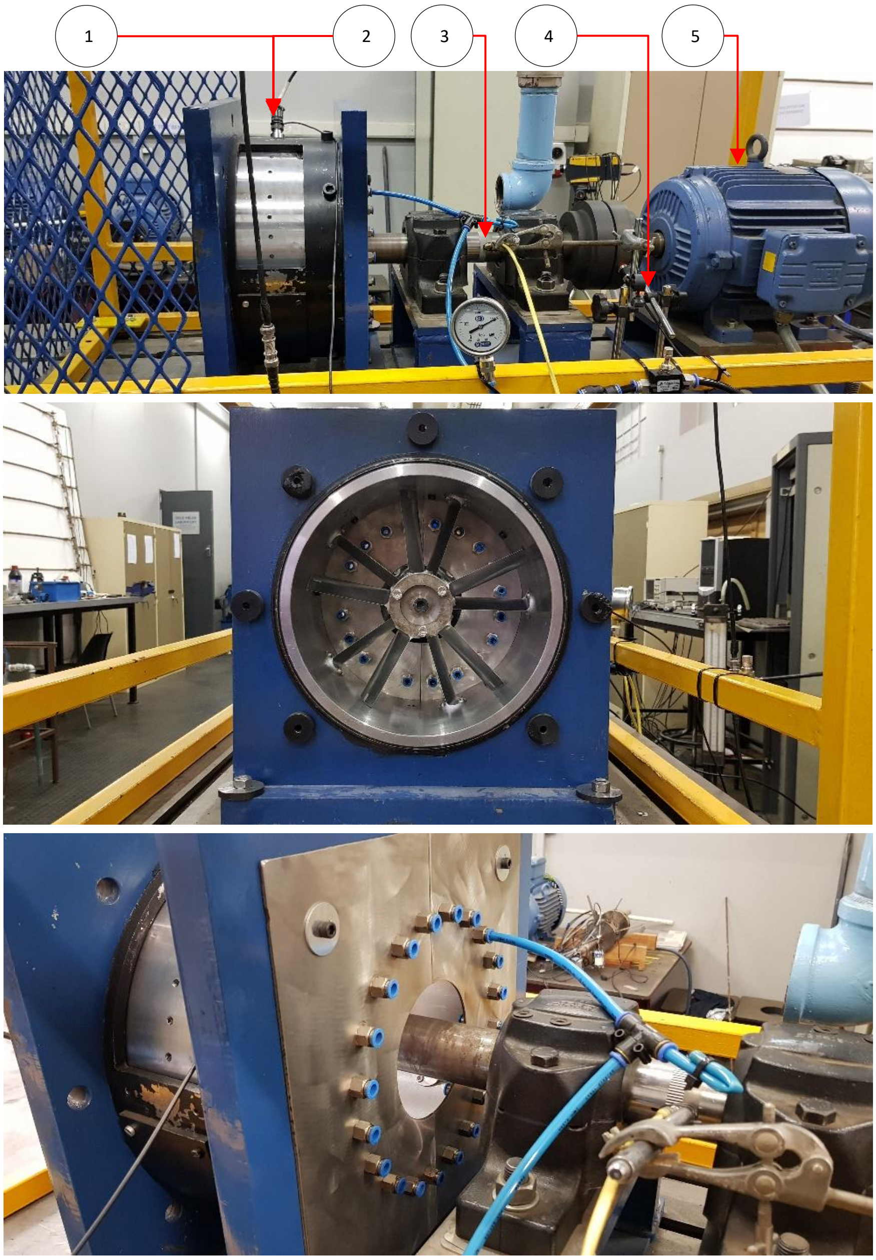

Figure 2.1. Experimental test bench. Overview of test bench (top); Blade arrangement (middle); Nozzle inlets (bottom)

The assembly included five stator and five rotor blades, which can also be viewed in Figure 2.1. This configuration was based solely on the existing test bench that was available. Furthermore, two rotor configurations were tested. A healthy configuration consisting of five identical healthy rotor blades and a damaged configuration consisting of four healthy rotor blades and a single damaged rotor blade.

The encoder data was used to sync the test data for different runs. The tachometer served as a reference for the encoder to ensure repeatability of the tests. A list of numbered items in Figure 2.1 are given in Table 2.1. It must be noted that auxiliary equipment such as a handheld anemometer were used to measure air velocity, etc., that are not added to the list in Table 2.1.

Table 2.1. Test bench equipment and sensor list

Placement	Sensor/equipment	Sensitivity/Information
1	*Microphone (ICP 378C01)*	$2\ mV/Pa$
2	*Accelerometer*	$100\ mV/g$
3	*Zebra tape encoder*	$79\ pulses\ per\ revolution$
4	*Tachometer*	$1\ pulse\ per\ revolution$
5	*Electric motor*	$Three - phase, 5.5\ kW$
6	*Quantum MX410 DAQ*	$4\ channels$

The response of the turbine rotor blades was measured using a microphone at the rotor blade tips and a casing accelerometer. The microphone was mounted flush with the casing's inner surface to detect pressure changes as the blades passed. The accelerometer was attached to the casing using wax and was also used as the secondary sensor for data capture as it was unsure at first whether it would produce any significant information of the rotor blade's response. An important note here is that only a single air nozzle was used to excite the rotor blades. This was done to produce the largest excitation from the available air supply. The nozzle (seen in Figure 2.2) was strategically chosen as the nozzle preceding the microphone (in the direction of rotation of the rotor blades) situated directly over a stator blade. This would also try to mimic the numerical model of chapter 3, whereby a single blade passage was modelled. The air velocity was measured by a handheld anemometer at the nozzle outlet as $65\ m/s$. There is, however, uncertainty in this measurement which will be numerically investigated in chapter 4.

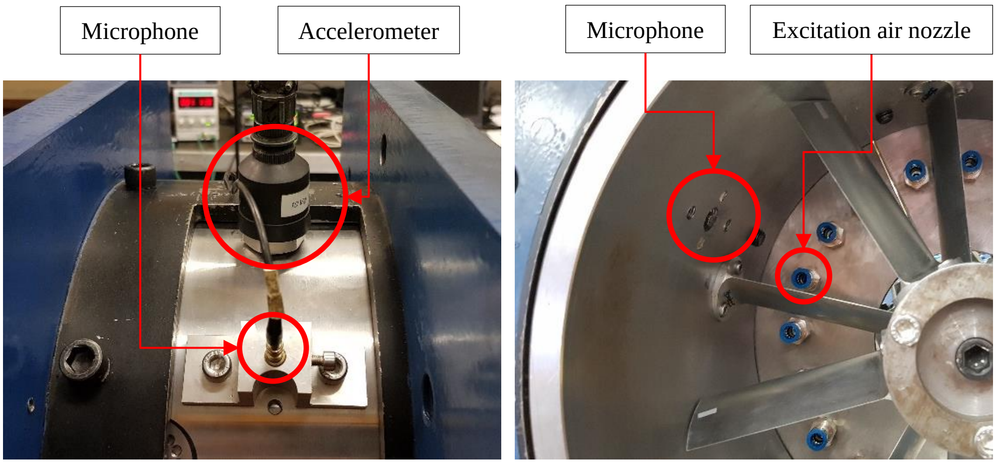

Figure 2.2. Measurement sensor placement

Although industrial turbine blades are normally twisted and tapered to optimal profiles shapes, manufacturing such blades is quite a tedious and expensive process. It was thus decided to make use of a simple blade profile that would still fulfil part an industrial turbine blade requirement. As stated in section 1.2.3.1, power utilities generally use blades that have an impulse design at the root which then twist into a reaction profile at the tip (Eskom Holdings, 2019). The blades used for the experimental testing are of the reaction-type, airfoil profile that have a uniform cross-section over the span of the blade. Thus, the section where the experimental blades are similar to industrial blades coincides with the key area of concern - the flow field around the tip - making it representative of an industrial setup.

The profile that was used for the stator and rotor blades was the NACA 4506 airfoil profile similar to the work of Alshroof *et al.* (2012), but here the chord length was chosen as $40\ mm$ as viewed in Figure 2.3. A portion ($\sim 5\%$) of the trailing edge (TE) was cut off to avoid having a sharp point and thus meshing complications in the numerical model of chapter 3.

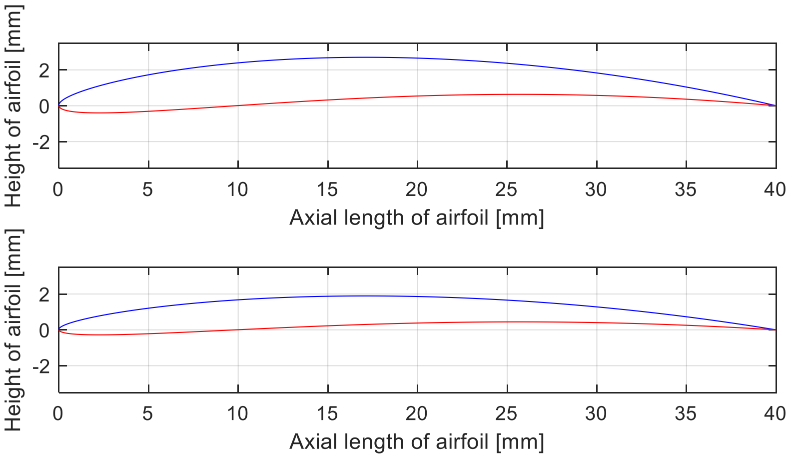

Figure 2.3. NACA 4506 Airfoil blade cross-section with chord length of 40 mm. Healthy blade (top); Damaged blade (bottom).

Also shown in Figure 2.3, are the profiles of the healthy and damaged rotor blades. The damaged rotor blade was made 70% of the thickness of the healthy blade both experimentally and numerically. The reason for describing the damaged blade in this manner is two-fold, namely: it assists in the meshing process of the numerical model described in chapter 3.1 as opposed to a damaged blade that is modelled as having a cut-out or notch somewhere along its span; and it still portrays a damaged state in terms of wear of the blade as it alters its mechanical response.

The manufactured blades can be seen in Figure 2.4. These blades were manufactured from aluminium alloy (6082 - T6) round bar which has a Young's modulus of $\mathbf{71\ GPa}$, a density of $\mathbf{2770\ kg/m^3}$ and Poisson's ratio of $\mathbf{0.33}$. A detailed mechanical drawing for the blades can be found in Appendix D: Test Turbine Technical Drawings, along with other drawings of the test turbine setup. The total height of the blades, from root (including $10\ mm$ hub mounting) to tip, is approximately $116.4\ mm$.

Figure 2.4. Manufactured blades showing the healthy and damaged blade (left) and the curved tips (right) to account for the casing curvature

2.2 Static Modal Analyses of Blades

A static modal analysis was performed on the rotor blades as assembled in the hub shown in Figure 2.1. A Polytec PSV 100 portable digital laser vibrometer was used to track the response velocity close to the tip of the blades while a modal hammer was used to excite the blades. Figure 2.5 shows the frequency response function (FRF) magnitude for the modal testing of the healthy and damaged rotor blades. Five healthy and two damaged blades were tested with the first static natural frequencies determined as 202.5 Hz and 131.1 Hz, respectively.

Quite a distinct difference exists between the natural frequencies of the healthy and damaged blades. This can be attributed mainly due to the difference in stiffness as the cross-sectional areas are different. The reduction in mass of the blades due to the difference in cross-sectional area is small as the masses only differ by approximately nine grams.

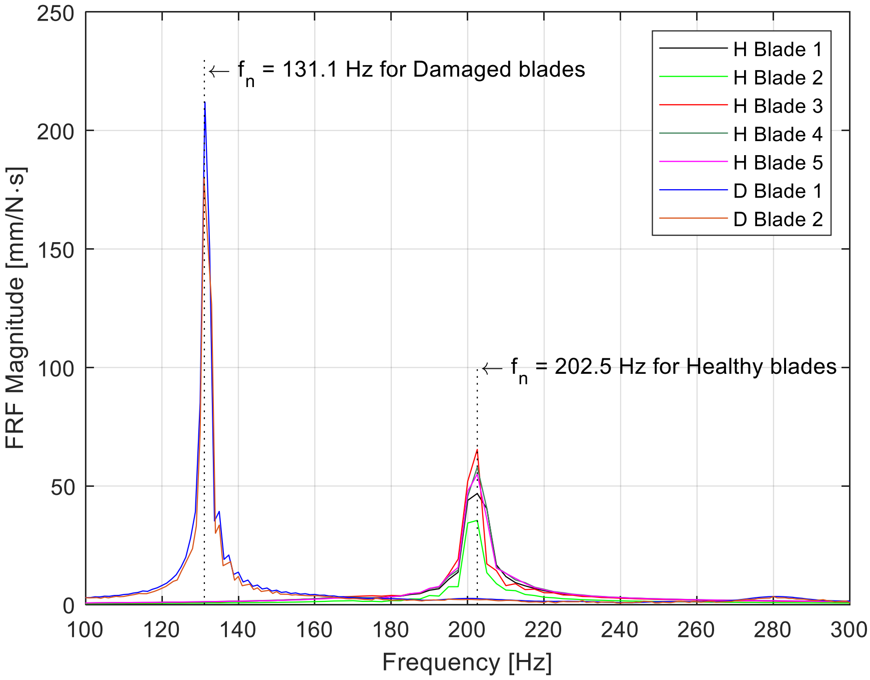

Figure 2.5. First static natural frequencies of healthy (H) and damaged (D) rotor blades

2.3 Experimental Methodology

The experimental tests on the mock-up turbine rig were split into two main groups. These included constant shaft rotational speed tests and varying rotational speed tests. The constant rotational speed tests were conducted 30 times for $5s$ at each shaft speed tested. The varying rotational speed tests were conducted using a digital triangular wave input from a signal generator. A total of 12 ramping tests were done over a period of $25s$ each whereby 6 tests were ramped up from 0 rpm to ~1378 rpm and 6 tests ramped down from ~1378 rpm to 0 rpm. All datasets were sampled at a frequency of $9600\ Hz$.

2.3.1 Measuring Shaft Speed

Although the linearly increasing wave input from the signal generator was not a pure analogue signal, the quantization effect on the experimental data was seen to be negligible. For instance, Figure 2.6 shows the quantization of the input voltage to the motor compared to the *ideal* analogue signal.

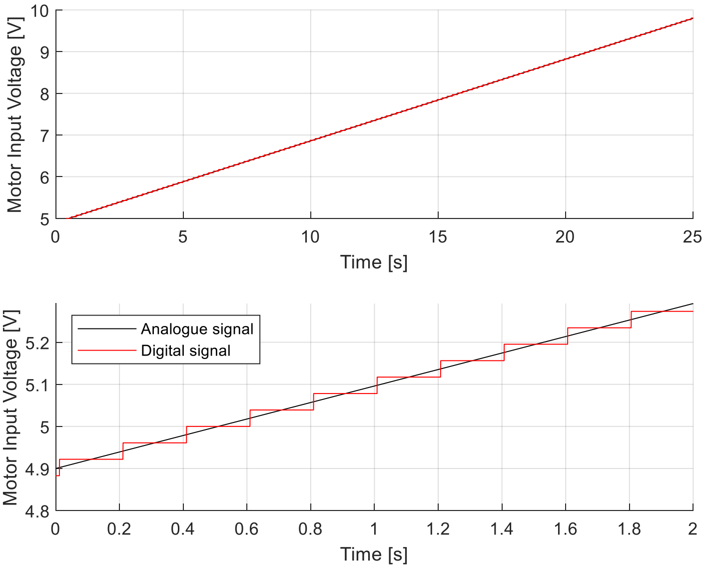

Figure 2.6. Quantization of motor input voltage for varying rotational speed tests. Full signal (top), zoomed-in view (bottom)

Converting the tachometer and optical shaft encoder data to time-dependent rotational speed series' yields sufficiently smooth data. The shaft shuddered slightly at low speeds ($< 150\ rpm$) due to the bearing and motor influences. This made it necessary to limit the data processing window to speeds above $150\ rpm$ including the speed ramping tests. Figure 2.7 shows the tachometer and encoder signals for a run-up run-down test.

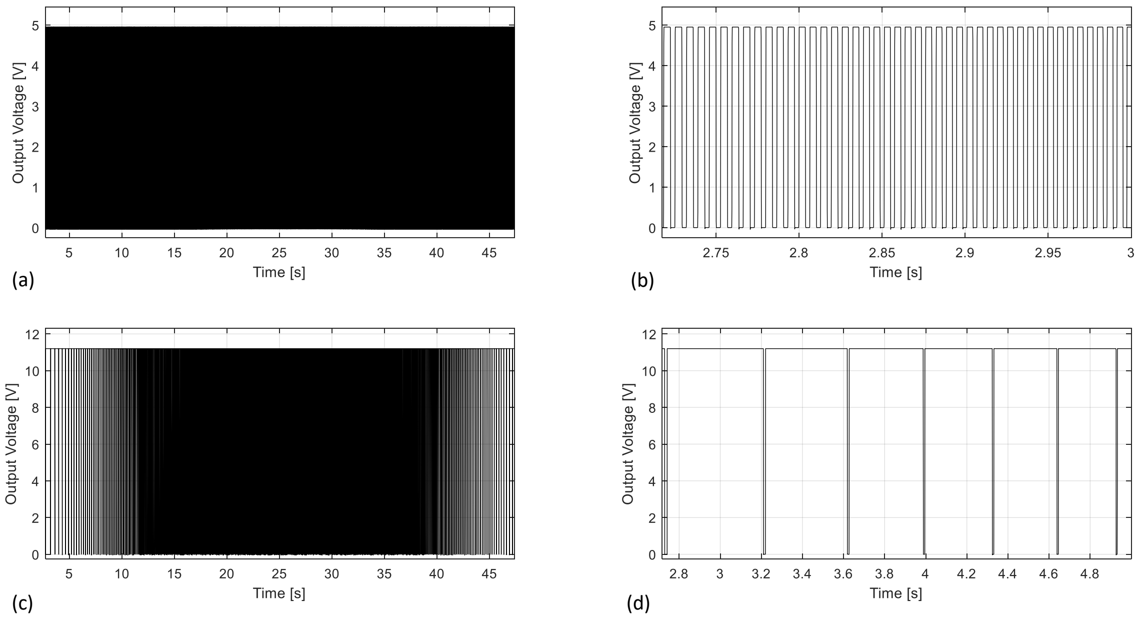

Figure 2.7. (a) Tachometer; (b) zoomed in tachometer; (c) encoder; and (d) zoomed-in encoder signals for ramp-up-ramp-down test

Figure 2.8 shows the shaft rotational speed computed from the tachometer and encoder signals of Figure 2.7. The resolution of the encoder is higher and thus a more defined signal is produced. Both signals contain information of the position and instantaneous speed of the shaft and rotor blades. One of the rotor blades were lined up with a marker on the shaft that was used by the tachometer. This was also the same position that the damaged blade was placed in the damaged configuration runs. This allowed the use of a trigger on the data acquisition device to start recording data every time the tachometer sent out a pulse resulting in starting each of the tests at the same angular shaft position. This meant that the results for constant rotational speed tests were already synchronised and readily comparable.

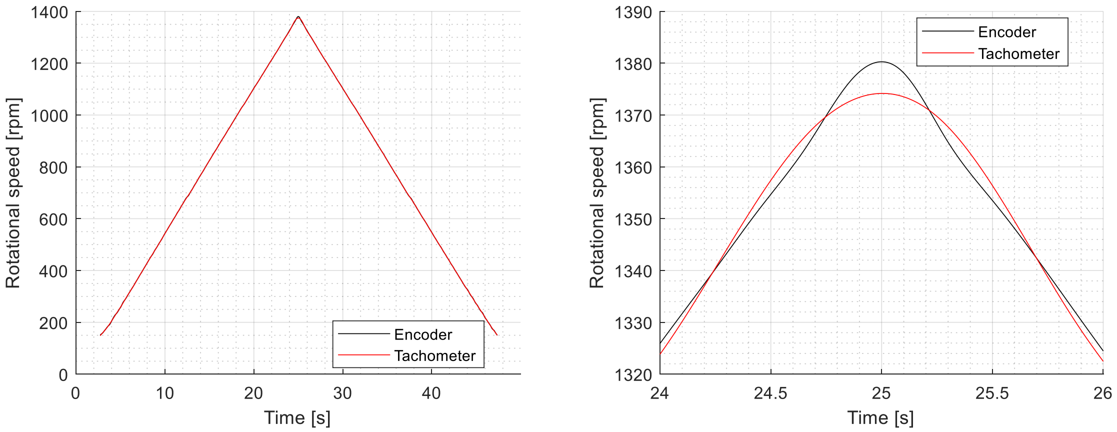

Figure 2.8. Shaft rotational speed computed from tachometer and encoder signals for ramping tests. Full signal (left); zoomed-in signal (right) showing the difference between the tachometer and encoder data

2.3.2 Critical Shaft Speeds

Recall from section 1.2.1.1 that an engine order (EO) is given by,

$$EO = \frac{f_{ex}}{f_s} \tag{27}$$

where EO is the ratio of the excitation frequency, f_{ex}, to the rotational frequency of the shaft, f_s. If the excitation frequency of interest is the natural frequency of the blade ($f_{ex} = f_n$), one would expect this to occur at a speed of $f_s \cdot 60\ [rpm]$.

For the healthy blade, that has a natural frequency of $202.5\ Hz$, a shaft speed of $12150\ rpm$ would result in resonance of the blade when neglecting damping and centrifugal stiffening. But there are stator row blades preceding the rotor blade row. Operating the turbine at $2430\ rpm$ would excite the first natural frequency of the rotor blade as $5 \times 2430 = 12150\ rpm$. In this case, $EO = 5$, which is representative of the stator or blade passing frequency (BPF). The BPF harmonic speeds, particularly the first harmonic speed, also produces resonance of the rotor blades as will be seen in chapter 4. Here the shaft speed of first BPF harmonic is $1215\ rpm$ and can be calculated in general for the h^{th} harmonic as,

$$N_{crit} = \frac{f_n \cdot 60}{5 \cdot (h+1)}\ [rpm] \tag{28}$$

where N_{crit} is now noted as the critical speed and $5 \cdot h$ is the EO (note: $h = 0$ for the blade passing frequency). These critical speeds are best viewed on a Campbell diagram such as that shown in Figure 1.3. Equation (28) was used to select constant shaft rotational speeds for the experimental tests. These speeds were not exactly equal to the critical speeds as the equation does not take damping, centrifugal stiffening of the rotor blade or pre-loads due to flow effects into account. The centrifugal stiffening of the rotor blade would lead to a higher first natural frequency and thus a higher critical speed for a specific EO. Nonetheless, these speeds would still be in the vicinity of the blade resonance frequency and thus still valid in producing data that would show some sign of resonance.

2.3.3 Preliminary Data Post-processing

As with most experimental datasets, filtering out some component of the data is always necessary, whether it be with a low-pass, bandwidth or high-pass filter. In this case, the first natural frequencies of the rotor blades were noted as the most important frequencies as they were most likely to be encountered. This led to using a low-pass filter on all the data to attenuate all high frequencies. It is important to mention that the signals were filtered in the forward and reverse directions to produce zero-phase distortion.

Figure 2.10 shows the filter experimental data for constant rotational speed runs of $1350\ rpm$. A 6th-order lowpass Butterworth filter was employed with a cut-off frequency of $600\ Hz$. It is evident that a great deal of high frequency content is present in the broadband signals.

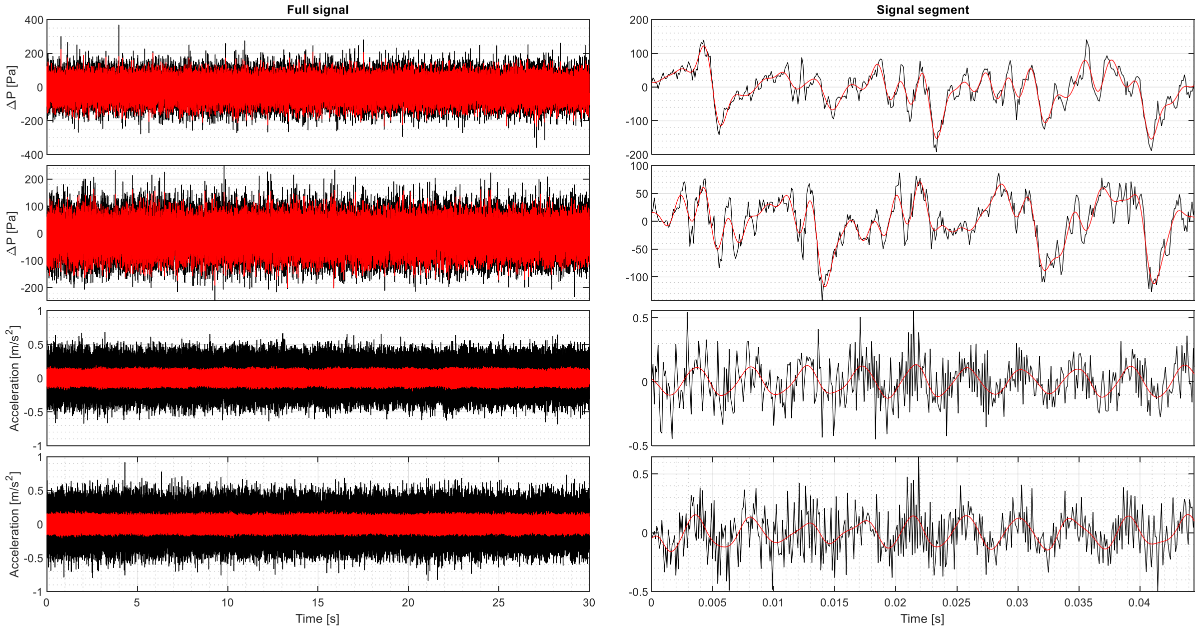

Figure 2.10. Filtered (red) and unfiltered (black) microphone and casing accelerometer data for constant rotational speed of $1350\ rpm$. From top to bottom: microphone (healthy configuration), microphone (damaged configuration), accelerometer (healthy configuration) and accelerometer (damaged configuration).

The same filtering process was followed for the linearly varying rotational speed tests. Figure 2.9 shows filtered and unfiltered sensor data for a single run. The accelerometer data shows clear peaks at specific times and hence specific shaft speeds. This will be elaborated on in chapter 4, as they signify critical speeds and amplified blade response.

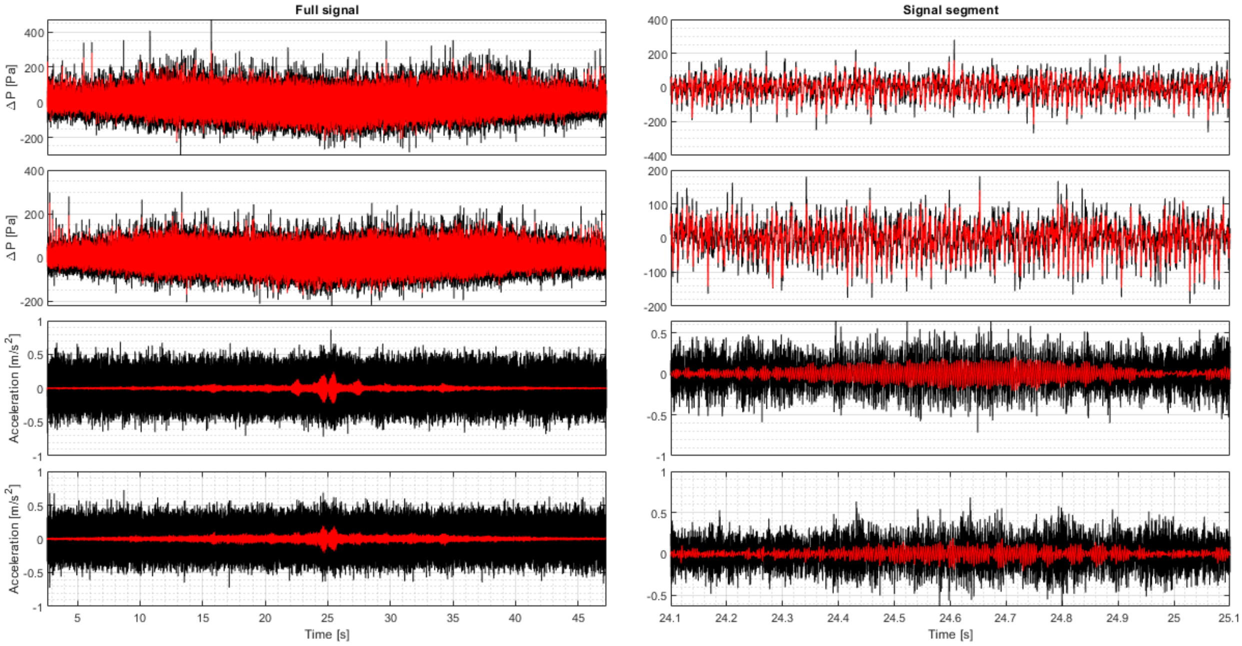

Figure 2.9. Filtered (red) and unfiltered (black) microphone and casing accelerometer data for linearly varying rotational speed. From top to bottom: microphone (healthy configuration), microphone (damaged configuration), accelerometer (healthy configuration) and accelerometer (damaged configuration).

2.4 Conclusion of Experimental Testing Section

The experimental testing methodology and data preparation was presented in this chapter. Two rotor configurations were tested - a healthy configuration consisting of five identical healthy rotor blades and a damaged configuration consisting of four healthy rotor blades and a single damaged rotor blade. Initially, static modal analyses were carried out on the two rotor configurations showing the first static natural frequency of the healthy and damaged blades to be $202.5\ Hz$ and $131.1\ Hz$, respectively. Only, the first natural frequencies of the blades were noted as they were most likely to be encountered considering the operational range of the test bench.

The experimental tests were split into two main groups: linearly varying and constant rotational speed tests at estimated critical speeds. Low pass filtering was employed to all the data collected to remove all frequencies above $600\ Hz$. Further discussions and post-processing will be presented in chapter 4.

3 Numerical Model

This chapter presents the numerical model used for the study. The structural domain, fluid domain and FSI coupling setup is described here. Mesh refinement studies, a timestep sensitivity study and structural solver type study are presented next. Lastly, some post-processing of the simulation data is shown.

This chapter contains some terms and definitions not covered in the literature review that are relevant to the ANSYS multiphysics environment (version R2 2019).

The computer used for all simulations has the following build: AMD Ryzen 7 2700X CPU (8 x cores, 16 threads, 3.7 (4.3 GHz Turbo)) and 32GB DDR4 RAM. All models include the NACA 4506 airfoil profile for stator and rotor blade cross-sections with a chord length of $40\,mm$ as seen in Figure 2.3. Approximately 5% of the trailing edge (TE) was cut off to avoid having a sharp point. The straight cut-off TE was then rounded in the numerical model to produce a higher quality mesh.

3.1 Fluid Domain

This section will give a through overview of the fluid domain geometry, mesh and boundary conditions. Furthermore, the mesh refinement study and timestep sensitivity study setup and results are presented.

3.1.1 Geometry and Mesh

The geometry consists of one flow passage, i.e. a 72° slice, of the experimental annulus of Chapter 2 with one stator blade and one rotor blade. This was chosen to reduce the computational domain. It does, however, imply that the flow effects simulated are identical in each flow passage, which is not the case when one of the blades in the assembly are damaged. It also implies that if a single damaged

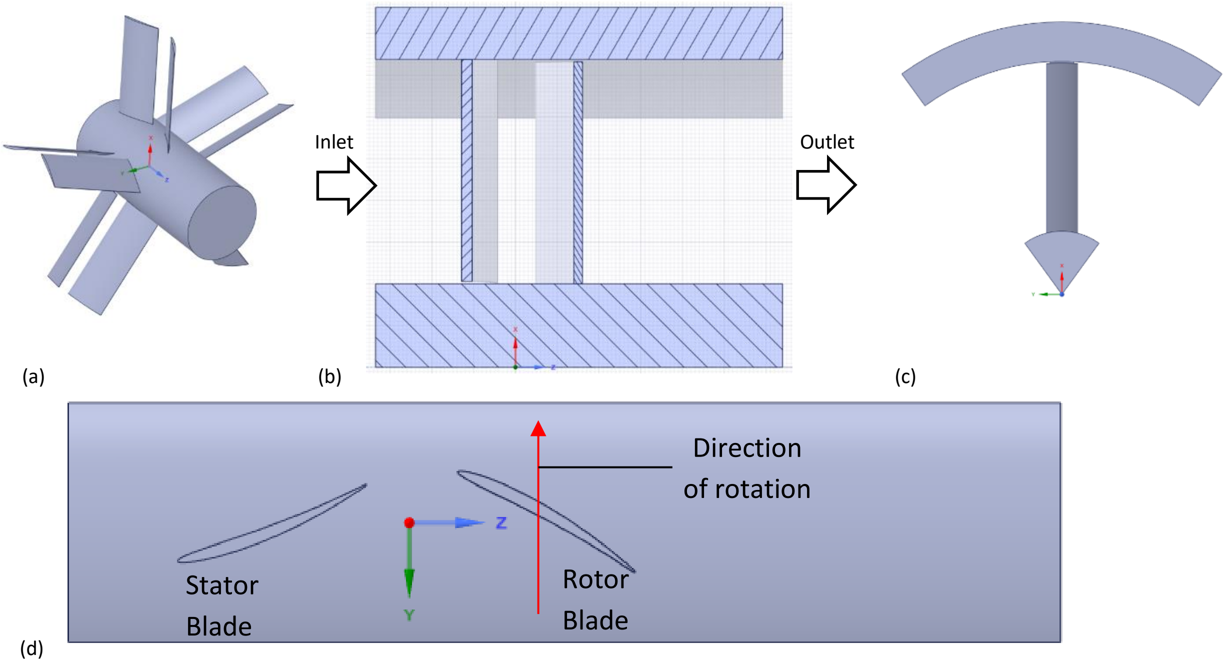

Figure 3.1. Geometry that the fluid domain is based on. Rotor assembly and stator blade row (a); Axial cross-sectional view of turbine stage showing direction of flow (b); Front view of simulated annular section (c); Top view of annular section showing blade angles and direction of rotation (d)

rotor blade is simulated, that all other blades and flow paths are identical. It will, however, suffice as the study attempts to obtain blade condition information in the pressure field in close proximity to the blade and hence, studying the effect of the two-way FSI pressure field on a single blade is acceptable.

Figure 3.1 shows the geometry that the fluid domain is based on as well as the rotor and stator blades. All dimensions are based on the actual experimental test rig of chapter 2 and are documented in Table 3.1. It must be noted that the hub, casing and stator blade were never simulated - their geometrical influences were, however, accounted for by making use of the model in Figure 3.1.

Table 3.1. Geometrical dimensions of numerical fluid domain

Dimension	**Value**
Stator blade stagger angle	$22.5°$
Rotor blade stagger angle	$30°$
Centre distance between blade rows	$54\ mm$
Inlet length with respect to the stator blade centre	$40\ mm$
Outlet length with respect to the rotor blade centre	$101\ mm$
Hub diameter	$80\ mm$
Casing diameter	$295\ mm$
Blade length (stator and rotor)	$106.4\ mm$

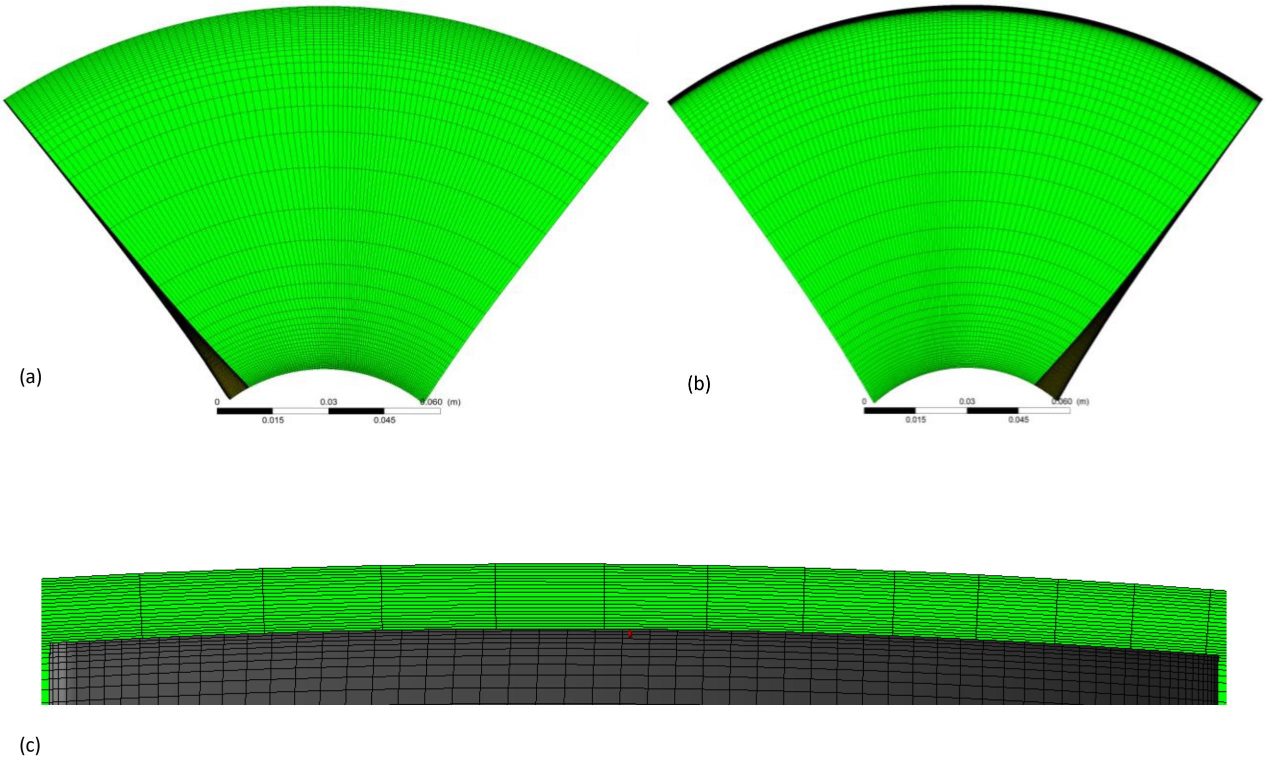

Figure 3.2. Fluid domain mesh. Stator domain inlet (a); Rotor domain inlet (b); Rotor domain mesh refinement at blade tip (c)

The fluid domain was extracted from the model shown in Figure 3.1 and subsequently meshed. The mesh of the fluid domain was created using Ansys TurboGrid which employs an optimised automated topology and meshing approach to provide a high quality anisotropic hexahedral mesh (ANSYS, 2018e).

Figure 3.2 shows the differences in the stator and rotor domain inlets (note that the rotor domain inlet is connected to the stator domain outlet through a boundary condition elaborated on in section 3.1.2). More emphasis was placed on the rotor domain mesh as can be seen with the increased mesh refinement in the layer between the blade tip and casing. This was done to ensure the flow effects were captured properly through the small blade tip gap. Figure 3.3 shows the full fluid domain meshes. Also seen in Figure 3.3 is the boundary layer mesh refinement at the rotor blade tip. A non-conformal mesh is implemented at the tip to preserve mesh quality. The fluid meshes are pure structured hexahedral meshes with grid spacing and refinement implemented sensibly in areas of importance. The meshes shown in Figure 3.2 and Figure 3.3 were the meshes used for all remaining simulations after the mesh refinement study (MRS) was performed.

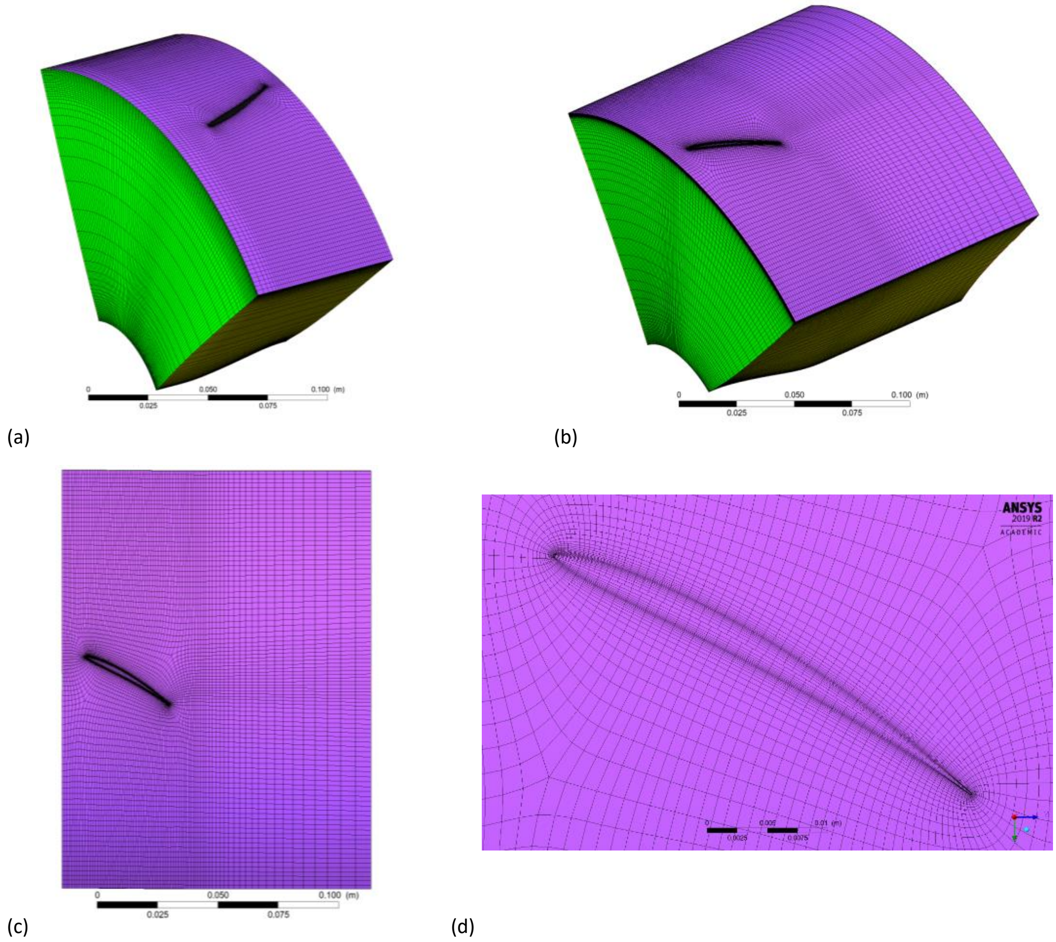

Figure 3.3. Fluid domain mesh. Stator domain (a); Rotor domain (b); Axial view of rotor domain (c); Boundary layer mesh and non-conformal mesh at rotor blade tip (d)

3.1.2 Boundary Conditions

The main boundary conditions for the fluid domain are illustrated in Figure 3.4. A detailed list of all the boundary conditions for the fluid domain are given in Table 3.2. The rotational periodic boundary is a special type of boundary condition that allows the flow to continuously flow through the boundary and into the “next” passage. This is perhaps better visualised by the velocity vector plot in Figure 3.5. It thus allows for the modelling of a reduced domain by assuming that the flow characteristics are cyclically identical.

The transient rotor-stator boundary condition is similar to the rotational periodic boundary condition in that it accounts for the interaction effects at the sliding interface between the stator and rotor passage. The rotor blade walls were set as rotating walls to account for the Coriolis forces acting on the fluid as the fluid swirls.

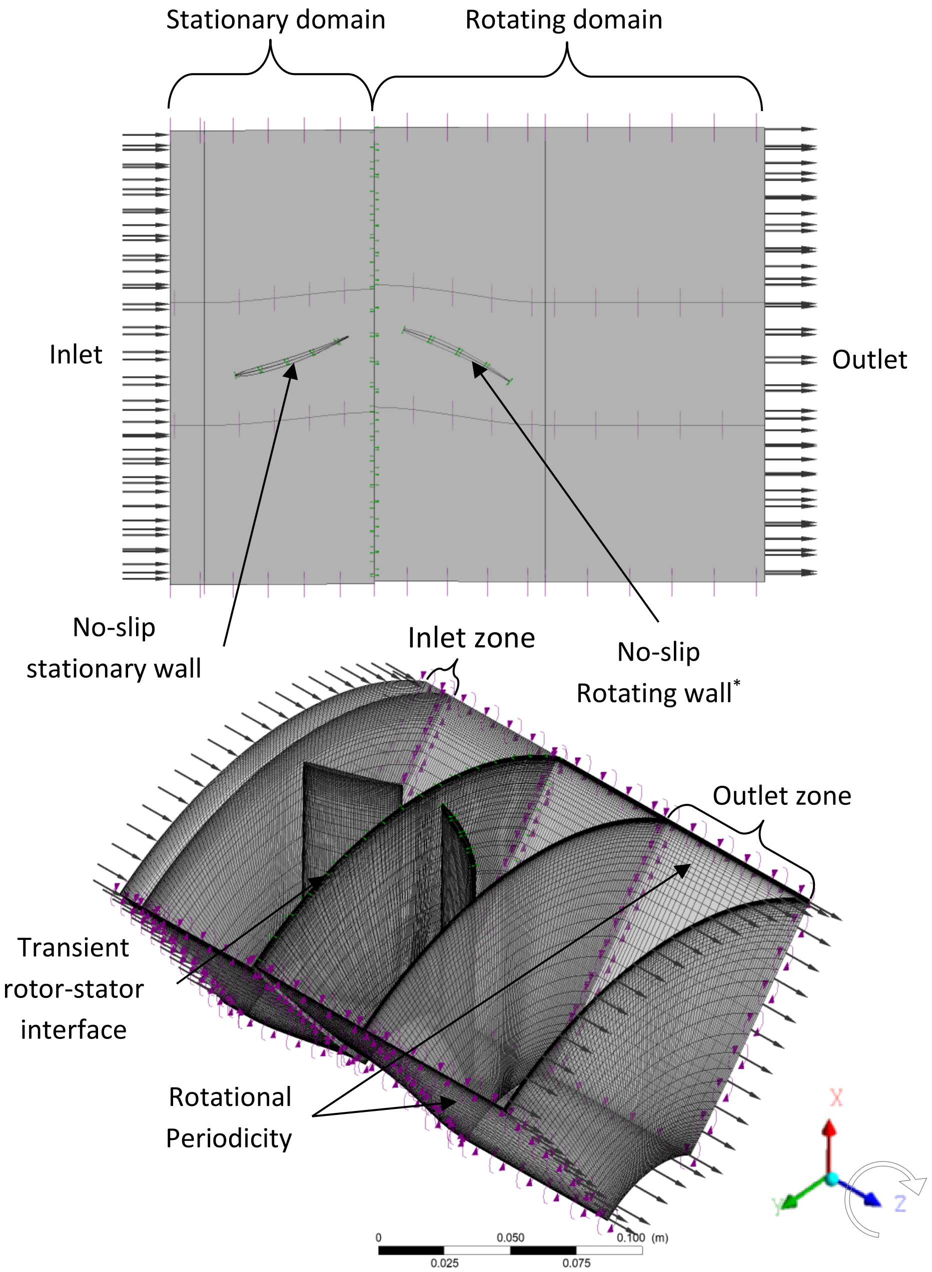

*Figure 3.4. Fluid domain boundary conditions. *Doubles as a fluid-structure coupling boundary in FSI simulations*

The inlet is set to a near-uniform velocity boundary condition. A small 5% radial variation is taken into account through CFX. It is important to note here that an assumption is made on using a near-uniform flow field which differs from the experimental test bench of chapter 2. The effect of the magnitude of this uniform inlet velocity will be studied in chapter 4.

Table 3.2. Fluid domain boundary conditions

Boundary	**Condition**
Inlet	Velocity inlet
Outlet	Average static pressure = 0
Casing surface	Stationary no-slip wall
Hub surface	Rotating no-slip wall
Stator blade surface	Stationary no-slip wall
Rotor blade surface	Rotating no-slip wall at a specified rotational speed
Rotor fluid domain	Rotating domain at a specified rotational speed about the z-axis
Stator fluid domain	Stationary domain

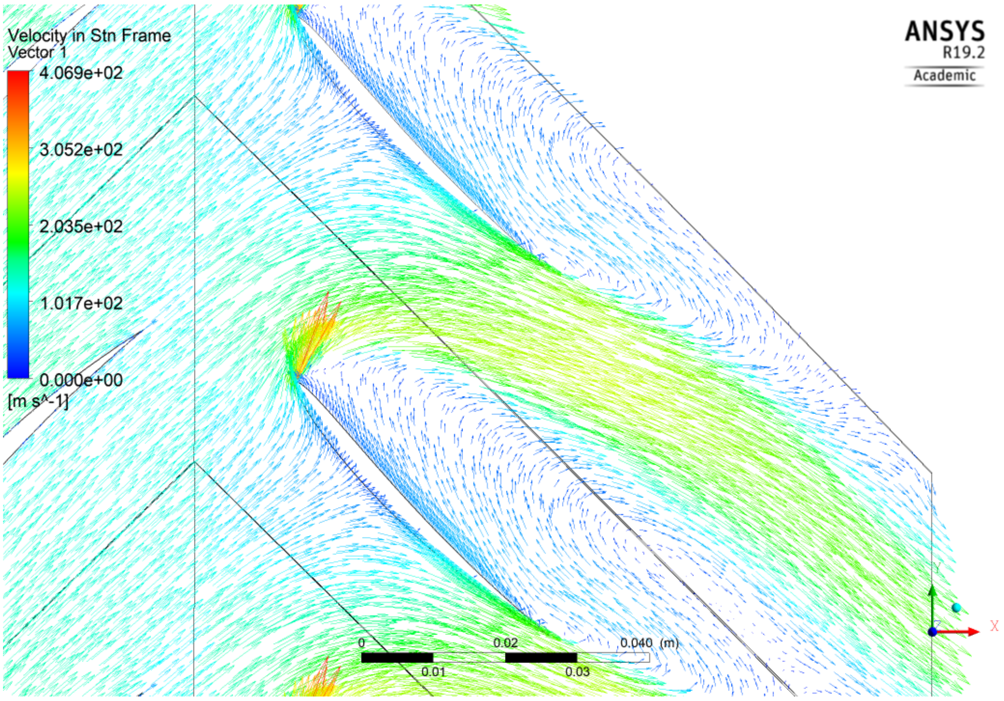

Figure 3.5. Velocity vector plot of the flow through three rotor blade passages illustrating the rotationally periodic boundary condition (rotor blade motion is clockwise around the positive x-axis)

3.1.3 Fluid Material Properties

This section contains the finer details of setting up the fluid domain solver. As previously discussed, the flow through a turbine contains laminar, transition as well as turbulent regions. Although the flow is comprised of different flow regimes in different regions, the focus of this study is the blade loading information and not prediction of the boundary state. Thus, only turbulent modelling will be considered. A major challenge that turbulence modelling faces is the accurate prediction of flow separation over smooth surfaces (ANSYS, 2018a). In general, two-equation RANS turbulence models underpredict turbulence effects in regions of strong pressure gradients (ANSYS, 2018a). The SSTKO turbulence model was thus developed to give highly accurate predictions of flow separation in regions of strong pressure gradients through inclusions of the effects in the turbulent viscosity formulation. Hence, it will be used to model turbulence in this work as there exists such adverse pressure gradients over the rotor blades due to the flow separation produced by the stagger angle of the blades.

The properties of the fluid can be found in Table 3.3. The air properties were based on the ambient temperature and pressure measured in the laboratory. The properties were attained using the information presented by Engineering ToolBox (2005). The compressibility of air was neglected for all simulations.

Table 3.3. Inlet air properties

Dry air (At 18°C, subsonic flow)	
Properties	**Value**
Density, ρ	$1.212\ kg/m^3$
Dynamic viscosity, μ	$1.803 \times 10^{-5}\ Pa \cdot s$
Pressure, P	$1.025\ bar$
Reynolds number	$Re = \frac{\rho\lvert V\rvert L}{\mu} \approx 174775 \rightarrow Turbulent\ flow$ L is the chord length of the blade cross-section

3.1.4 Mesh Refinement Study

As with any numerical method, whether spatially- or time-discretised, there exists an error caused by the discretisation of the scheme. This makes it necessary for grid convergence studies or some type of uncertainty estimation of the solutions obtained from CFD in order to test mesh-independence of the solutions. The GCI method presented in section 1.2.3.2 is implemented next to estimate the grid convergence accuracy of the fluid domain model presented in this study.

A set of steady state CFD simulations were run using the same boundary conditions with varying mesh densities as part of a mesh refinement study (MRS). A fixed ratio of approximately 1.265 was used to refine the mesh and a total of 3 mesh refinements were made. The stator-rotor interface boundary was now set to a mixing plane model instead of the *transient rotor-stator* shown in Figure 3.4. The mixing plane interface model is used for steady state CFD simulations. It averages, or *"mixes out"* the circumferential non-uniform flow profiles at the stage interface by calculating these averaged profiles on the upstream side of the interface and then applying it to the downstream side of the interface. The circumferential profile average is a function of the radius only (hub to casing spanwise direction) and subsequently cannot model the effects of wakes and shock wave interactions.

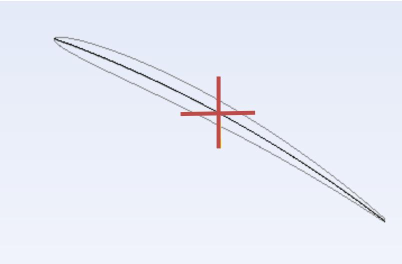

Figure 3.6. Pressure monitor point used in MRS simulations.

Table 3.4 shows the solver setup parameter and boundary conditions used for the MRS simulations. The rotational speed was chosen as $1418\ rpm$ as this was the maximum possible rotational speed achievable with the experimental test bench. Hence, it was chosen as the benchmark speed for the MRS and timestep sensitivity study. Figure 3.6 shows the pressure monitor point used for the MRS simulations. The point was placed in the centre of the blade up against the casing such that it mimics the experimental test bench microphone placement.

Table 3.4. MRS Solver setup and boundary conditions

Analysis Setting/Boundary Condition	**Property/Scheme**
Rotational speed	$1418\ rpm$
Inlet velocity magnitude	$65\ m/s$
Turbulence model of all quantities	SSTKO
Turbulent kinetic energy, k	High Resolution[1]
Specific dissipation rate, ω	High Resolution
RMS residual convergence tolerance	$1E-6$ for all residuals

The mesh parameters for the MRS simulations are given in Table 3.5. Following the systematic GCI method of Roache (1994) by using equations (20) to (24), the results of the MRS are presented in Table 3.6 using the pressure monitor point of Figure 3.6.

Table 3.5. MRS mesh parameters for fluid domain

	Mesh A		**Mesh B**		**Mesh C**	
	Rotor	Stator	Rotor	Stator	Rotor	Stator
Hub boundary layer elements	15	15	15	15	15	15
Elements between boundary layers	12	10	20	18	30	25
Shroud boundary layer elements	18	16	20	20	25	24
Shroud/Hub tip elements	16	4	20	4	25	4
Stator inlet/Rotor outlet elements	22	5	24	6	26	8
Elements per component	*519389*	*326218*	*652715*	*417415*	*843925*	*509824*
Total elements	**845607**		**1070130**		***1353749***	
Total Pressure at tip [Pa]	806.7		816.4		819.1	

Focusing on the result of the GCI method in Table 3.6, the ratio $\frac{GCI_{23}}{r^p GCI_{12}}$ is approximately unity, indicating that even the coarsest mesh used in the MRS simulations would give satisfactory results. These results show that there is also a difference of only $\approx 0.16\%$ between the medium and fine mesh. It can be concluded that the solution is indeed in the asymptotic range of convergence. Furthermore, the static pressure distribution at the rotor midspan and the spanwise total pressure at

---

[1] The High Resolution transient scheme uses the second order backward Euler scheme whenever possible and reverts to the first order backward Euler scheme to maintain a bounded solution (ANSYS, 2018a)

different streamwise locations were reviewed in Figure 3.7 as supporting evidence as to which mesh would provide decent accuracy while minimising the number of elements used.

Taking a closer look at the pressure distribution at the rotor blade midspan, a good matching between all grids can be observed. There are no shocks present in the flow, but it is, however, evident that the coarse mesh overpredicts the pressure on the suction side and under predicts the pressure on pressure side of the rotor blade with respect to the finer meshes. Similar results are seen in Figure 3.7 (b) where the coarse radial meshing of mesh A does not capture the pressure profile as smoothly as the finer meshes.

Table 3.6. MRS results based on GCI method of Roache (1994).

	f_1 $(\boldsymbol{Mesh\ C})$	f_2 $(\boldsymbol{Mesh\ B})$	f_3 $(\boldsymbol{Mesh\ A})$
$P_{total}\ [Pa]$	806.725281	816.34845	819.074036
r	1.265		
p	5.3664		
f_{exact}	820.151		
GCI_{12}	0.001644 (0.1644 %) using $F_s = 1.25$		
GCI_{23}	0.005823(0.5823%) using $F_s = 1.25$		
$\frac{GCI_{23}}{r^p GCI_{12}}$	$= 1.0033 \approx 1$		

The predictions of the pressure profile as various streamwise locations is quite similar between the fine and medium mesh. Hence, the medium mesh - mesh B with $\approx$ 1.07 million cells - will be adequate for all further fluid flow simulations and will also save computation time with respect to the fine mesh of $\approx$ 1.35 million cells.

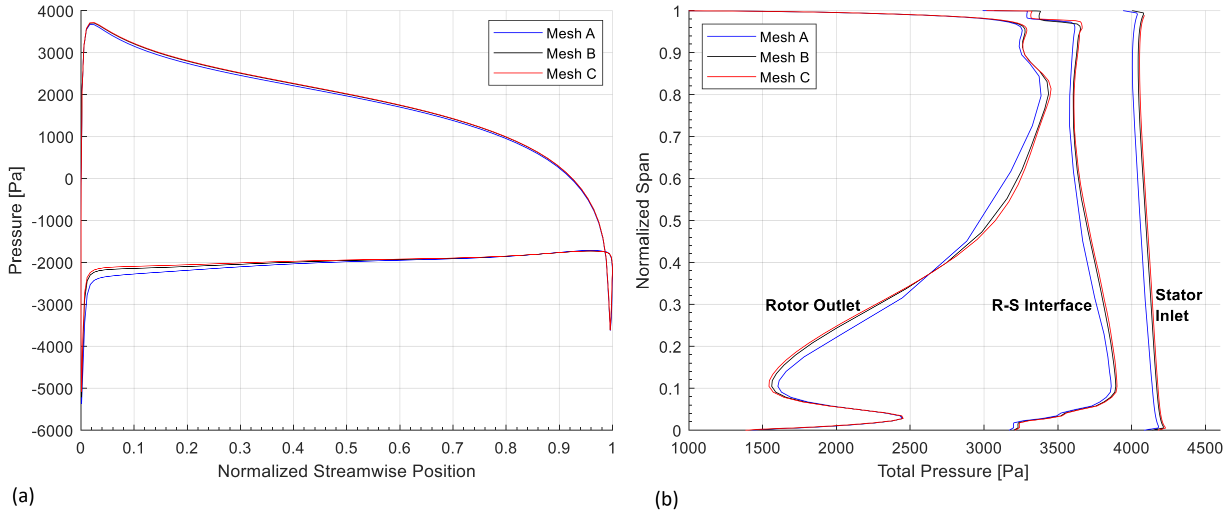

(a) (b)

Figure 3.7. MRS pressure distribution. Static pressure distribution at rotor midspan (a); Spanwise total pressure distribution at streamwise locations (b).

3.1.5 Timestep Sensitivity Study

As all the FSI simulations will be transient in nature, a timestep needs to be chosen to ensure the temporal discretisation adequately captures the unsteady flow characteristics. The CFD mesh is undoubtedly the larger and more important mesh and thus the timestep chosen for all of the analyses will be based on the outcome of this timestep sensitivity study.

The blade passing period (BPP) is divided into $12, 24, 48, 96$ and 192 equal steps. The corresponding timestep sizes are based on, once again, the maximum achievable shaft rotational speed of $1418\ rpm$ and its corresponding BPP of $0.008462623s$.

As the initial conditions for the transient case were set to a steady state result, with corresponding inlet velocities and rotational speeds, the first BPP includes a portion of erratic data. This arises from the fact that the steady state simulations were performed using the mixing plane model interface leading to wake interaction over the rotor-stator interface not being computed. Recall that this circumferential profile average of the mixing plane model is a function of the radius only. This led to simulating three BPPs and subsequently removing the first BPP data. The same approach was taken for all transient and FSI simulations. An example of the difference between the mixing plane model and the transient rotor-stator interface can be seen in the pressure contour plot of Figure 3.8.

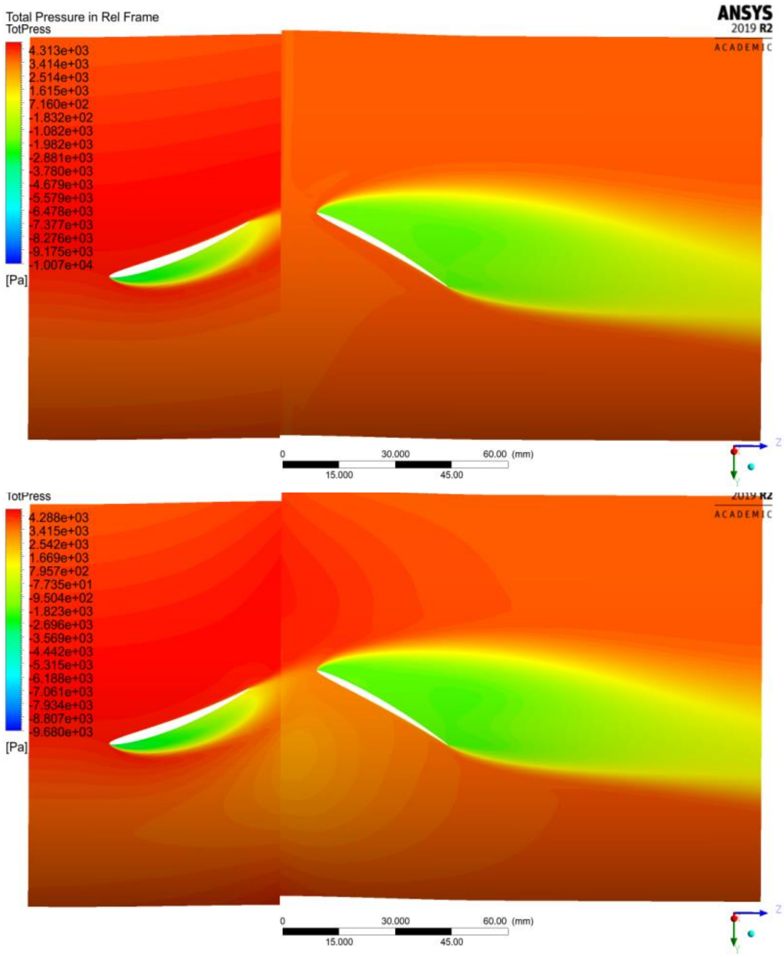

Figure 3.8. Pressure contour showing the difference between the mixing plane model (top) and transient rotor-stator interface (bottom) at rotor midspan.

It is clear that the mixing plane model does not take the stator domain's wakes into account, whereas the transient rotor-stator interface does calculate these profiles as a function of the radial, circumferential and axial directions.

Table 3.7 shows the solver setup parameter and boundary conditions used for timestep sensitivity simulations. Any solver setting not included here is set to a default CFX value. The total pressure was again monitored, but at various locations in close proximity to the rotor blade. Figure 3.8 shows the pressure monitor points used for the timestep sensitivity study. It includes points at the LE and the TE and then at the centre of the blade on the casing, at the blade tip and midway between the blade tip and casing. These monitor points were also used for the FSI simulations.

The pressures at the monitored points of Figure 3.9 are shown in Figure 3.10 for the various timestep sizes simulated. The monitor point that is located at the centre of the blade on the casing is representative of the microphone location on the experimental test turbine of chapter 2. It is clear that the refinement of the passing time periods allows for the prediction of the smaller oscillations in the pressure profiles. The simulations that used 12, 24 and 48 timesteps were not able to resolve these smaller fluctuations. The simulations that used 96 and 192 timesteps provided more resolution at all the monitor points where one would expect complex flow patterns. While the finest timestep would result in slightly more temporal accuracy, the computational time differed by a factor of approximately 1.8, nearly double the solve time of the second smallest timestep investigated.

Table 3.7. Timestep sensitivity study solver setup and boundary conditions

Analysis Setting/Boundary Condition	**Property/Scheme**
Rotational speed	$1418\ rpm$
Inlet velocity magnitude	$65\ m/s$
Temporal discretization	Second order Backward Euler Method
Turbulence model of all quantities	SSTKO
Turbulent kinetic energy, k	High Resolution
Specific dissipation rate, ω	High Resolution
Simulation time length	$0.025388\ s$
Time step size	Varying
RMS residual convergence tolerance	$1E-4$ for all residuals
Minimum coefficient loops (per timestep)	3
Maximum coefficient loops (per timestep)	6

Thus, to save computational time for the FSI simulations while achieving adequate temporal accuracy, the BPP would be divided into 92 timesteps resulting in a timestep size of $8.8152E-5$ seconds. This timestep would be used regardless of the rotational speeds investigated, as all speeds tested would be less than the benchmark of $1418\ rpm$. Temporal accuracy would thus be retained, or even better, for slower rotational speeds.

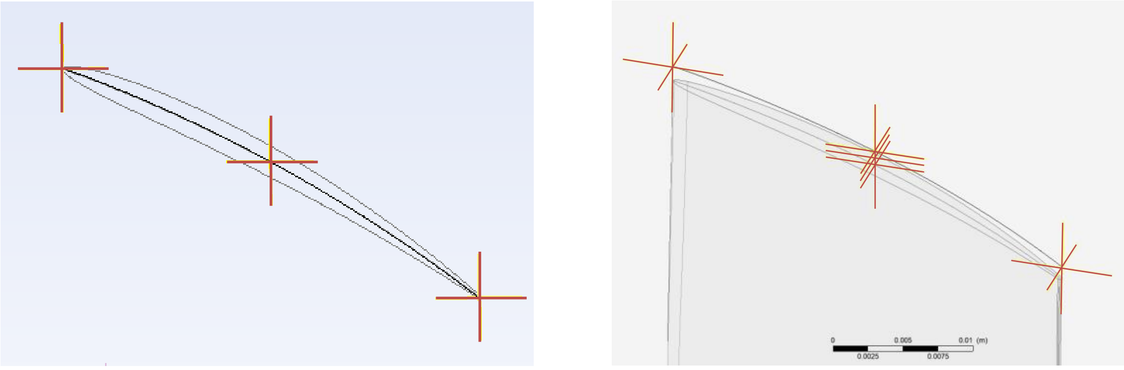

Figure 3.9. Pressure monitor points used for timestep sensitivity study

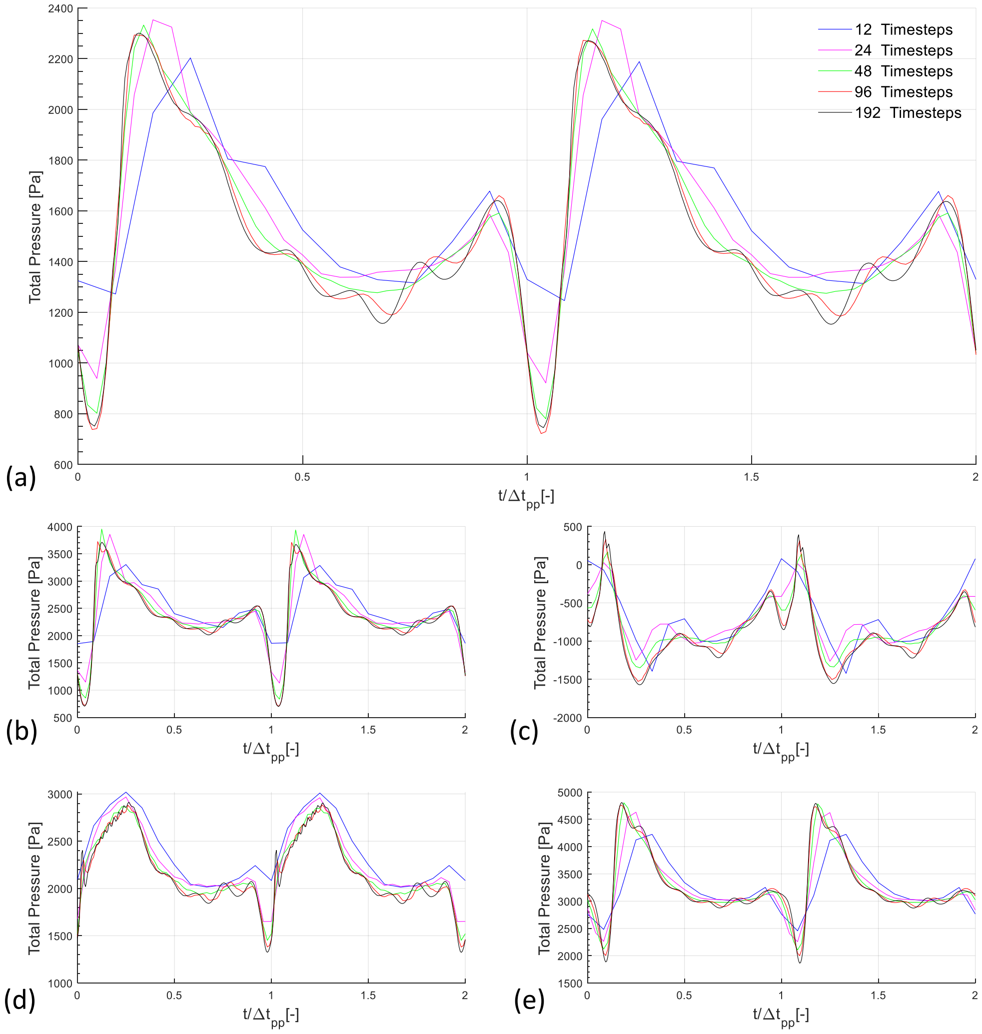

Figure 3.10. Timestep sensitivity study total pressure at: casing - centre of the rotor blade (a); midway between casing and blade tip (b); blade tip (c); LE (d); and TE (e).

3.2 Structural Domain

This section will present how the structural domain was modelled. Firstly, the stator blade was modelled as a rigid body in the fluid domain and hence it was not necessary add it to the structural domain. Although a vibrational response from a stator blade could possibly have some type of effect on the downstream flow and hence the flow over the rotor blade, this effect was excluded from the study to decrease the computational burden.

Damping was also assumed to be negligible. This was done in order to reduce the complexity of the problem, although damping would naturally be present in the physical setup. From herein after, the term *blade* will be used to describe the rotor blade, whether it be the healthy or damaged rotor blade. In cases where the stator blade is mentioned, it will be explicitly stated as such.

3.2.1 Geometry, Mesh and Material Properties

As a brief reminder to the reader, the profile of the blades used are that of a NACA4506 airfoil. The damaged blades have approximately 70% of the thickness of the healthy blades to simulate a type of wear state of the blade. The geometry of the blade was defeatured so that the meshing process could be carried out easier for both the fluid and structural domain. The root of the blade as well as the fillet at the base (Figure 3.11 (b)) were omitted in the numerical model resulting in a decrease in stiffness, which in turn altered the natural frequencies of the blade. It was thus necessary to either increase the stiffness of the blade through its elastic modulus or decrease the mass of the blade through its density. The former option was chosen, and the material properties can be viewed in Table 3.8.

Table 3.8. Rotor blade material properties - Aluminium alloy 6082 - T6 with Elastic modulus $71\ GPa$

Material Property	**Value for Healthy Blade**	**Value for Damaged Blade**
Density	$2770\ kg/m^3$	$2770\ kg/m^3$
Elastic modulus (original)	$89.7\ GPa\ (71\ GPa)$	$74\ GPa\ (71\ GPa)$
Poisson's ratio	0.33	0.33

Figure 3.11 shows the numerical model geometry of the physical blade and the defeatured blade used in this study. The defeatured blade length is equal to that of the physical blade from tip to the top of the base.

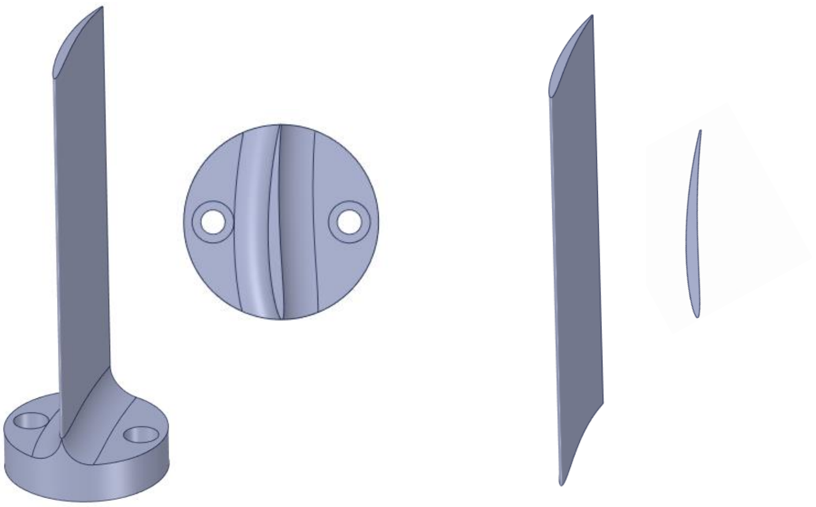

(a) (b)

Figure 3.11. Rotor blade: Physical blade with base (a); Defeatured blade (b).

3.2.2 Boundary Conditions and Solver Setup

Simple boundary conditions were used for the blade. The root of the blade (hub-side) was assigned a fixed boundary condition and a rotational velocity equal to that of the shaft speed was added to the blade body to account for the Coriolis forces. For the FSI simulations only, a *fluid-coupling* boundary condition was added to the three blade faces that would be in contact with the fluid (suction side, pressure side and tip surface) to allow for data transfers between the two domains to take place. All the boundary conditions and locations for the blade are shown in Figure 3.12. The solver settings for the structural solver are given in Table 3.9. Any solver setting not included here is set to a default Ansys Mechanical value.

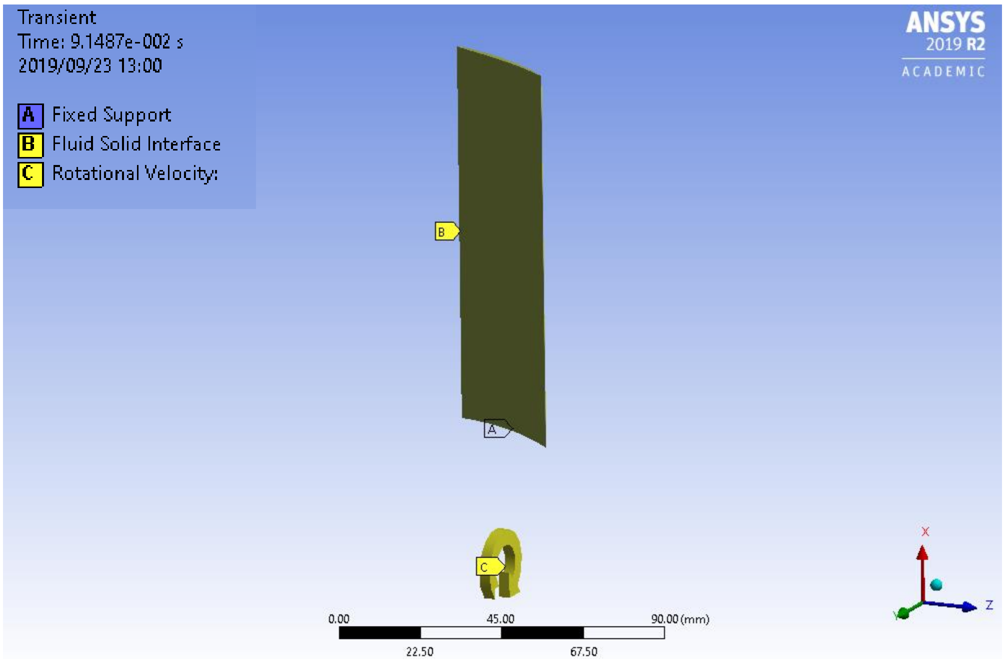

Transient
Time: 9.1487e-002 s
2019/09/23 13:00

A Fixed Support
B Fluid Solid Interface
C Rotational Velocity:

Figure 3.12. Rotor blade boundary conditions.

Table 3.9. Structural domain solver setup and boundary conditions

Analysis Setting/Boundary Condition	Property/Value
Rotational speed	Dependent on speed being tested
Large deflection formulation	Effect was tested in section 3.2.4
Force convergence tolerance (min. ref.)	$1E-3\ \%\ (1E-4\ N)$
Moment convergence tolerance (min. ref.)	$1E-3\ \%\ (1E-4\ N \cdot mm)$
Displacement convergence tolerance (min. ref.)	$1E-3\ \%\ (0\ mm)$
Rotational convergence tolerance (min. ref.)	$1E-3\ \%\ (0°)$

3.2.3 Mesh Refinement Study

Obtaining mesh-independent solutions for the structural domain is just as important as that of the fluid domain, hence the inclusion of a structural mesh refinement study. A modal analysis was performed on the blade to determine the adequate number of elements needed for the remainder of the structural analyses. Both linear order and quadratic order elements were used.

Although, only the first natural frequency is of interest as it has the highest chance of being triggered, the first two natural frequencies of the blades were computed.

The mesh size was varied through the element size used to discretise the domain in the spanwise direction (longitudinal direction of the blade). The element size in the spanwise direction was reduced by 80% for each mesh studied. Table 3.10 shows the computed natural frequencies of the healthy blade for different mesh sizes and different element types.

Table 3.10. Structural MRS using modal analysis

Element Type	Mesh number-Nodes/Elements	Spanwise Element Size [mm]	$f_1\ [Hz]$	$f_2\ [Hz]$
Linear	$A-56488/48972$	5	202.6624	1079.074
	$B-68768/60102$	4	202.4968	1078.653
	$C-85960/75684$	3.2	202.3491	1078.271
	$D-105608/93492$	2.56	202.2347	1077.975
	$E-132624/117978$	2.048	202.1285	1077.698
Quadratic	$F-218183/48972$	5	201.8039	1076.514
	$G-266148/60102$	4	201.802	1076.511
	$H-273882/61710$	3.2	201.8001	1076.506

Figure 3.13 shows the relative error made through spatial discretisation with respect to the quadratic element mesh H.

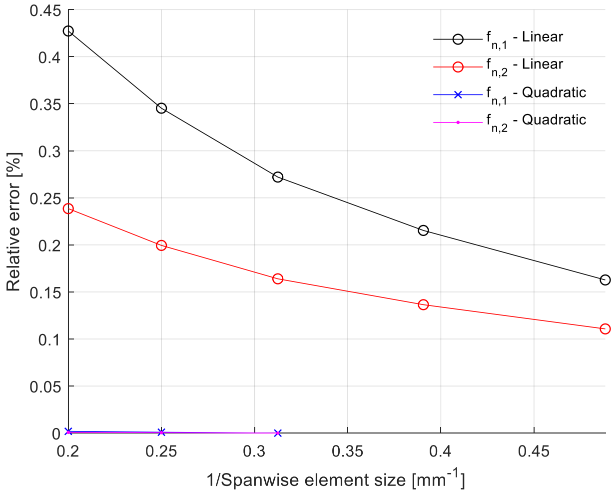

Figure 3.13. MRS for structural domain - Relative error in computed natural frequencies for different element types and sizes

As one can see in Figure 3.13, the relative error is very small for all meshes studied. The quadratic order element would indeed result in a more accurate solution to any of the structural analyses carried out in this study, but the computational cost does not justify the need for this especially because of the fact that the main focus area of this study is that of the flow field around the blade. Hence, a spanwise mesh element size of $4\ mm$ in conjunction with a linear order type element (mesh B) will be used for all further analyses.

3.2.4 Solver Type Investigation

A steady state load analysis was performed to compare the blade deformation for different solver types. A rotation of $0.1°$, $0.55°$ and $1°$, respectively, were applied to the blade tip around the z-axis (shaft of the turbine). The outcome determined which of the solvers would be more applicable for the remainder of the structural domain simulations, i.e. the geometrically nonlinear (GNLS) or geometrically linear solver (GLS). A geometrically nonlinear solver can however solve geometrically linear problems, although the computational cost is unnecessary as it has an iterative solution. It was expected that the deformations and strains would be large in relation to the geometry size for the turbine setup described throughout this dissertation. Typically, one would use a geometrically nonlinear solver if the transverse displacements are more than 10% of the thickness of a slender structure (ANSYS, 2019). The investigation was performed using the healthy blade and it was expected that the findings would be directly applicable to the thinner damaged blade.

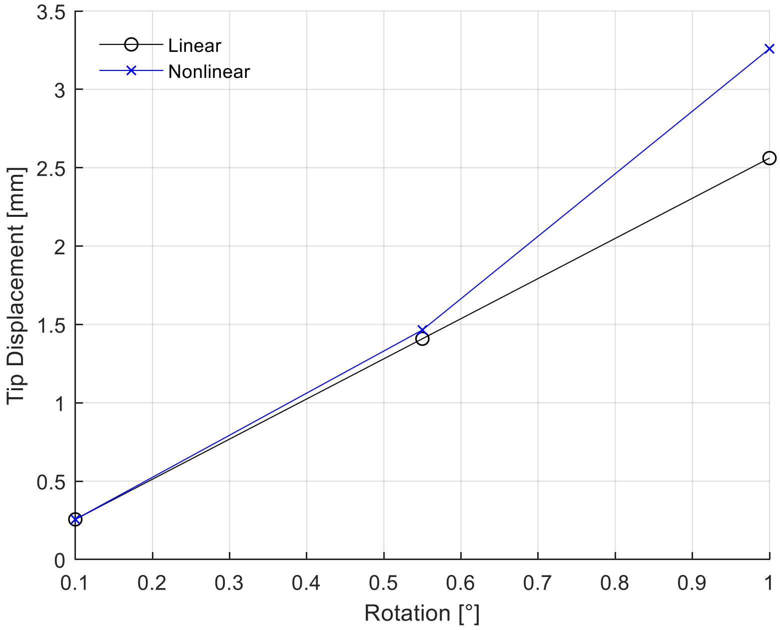

Figure 3.14. Blade tip displacement for steady state simulation using GLS and GNLS.

A GLS predicted linear displacement, as expected for the applied rotations. This can be viewed in Figure 3.14. The GLNS suggests however, that as the rotational increases, so too does the displacement of the blade, but nonlinearly. One can see for small rotations, the GLS and GNLS produce comparable results. As it is expected that the blade tip displacements of the FSI simulations are to be somewhat large, $\geq 2\ mm$ as seen in preliminary results, the GLNS will be used. If this is not the case, the GLNS will still predict the correct displacements, but at a slightly higher computational cost than the GLS.

3.3 FSI Framework

After a complete evaluation of the fluid and structural domain mesh and the selection of an appropriate timestep size, the FSI simulation setup can now be presented. The *System Coupling* service of Ansys would only link the transient fluid and structural domain through the specified data transfer interfaces to allow for the updating of each domain's boundary condition interactions. The fluid and structural models from the previous section are thus used as is. Hence, Ansys employs a partitioned method approach.

All FSI simulations were thus performed using a partitioned two-way approach. This decision was made due to the findings by Ubulom, Neely and Shankar (2017) and Alshroof *et al.* (2012) that pure one-way FSI models are highly conservative. They do not capture the full complexity of the flow through a turbine. The procedure employed by the *System Coupling* component in ANSYS Workbench is outlined in Figure 3.15 and a brief explanation is given in context of the transient simulations presented in this study.

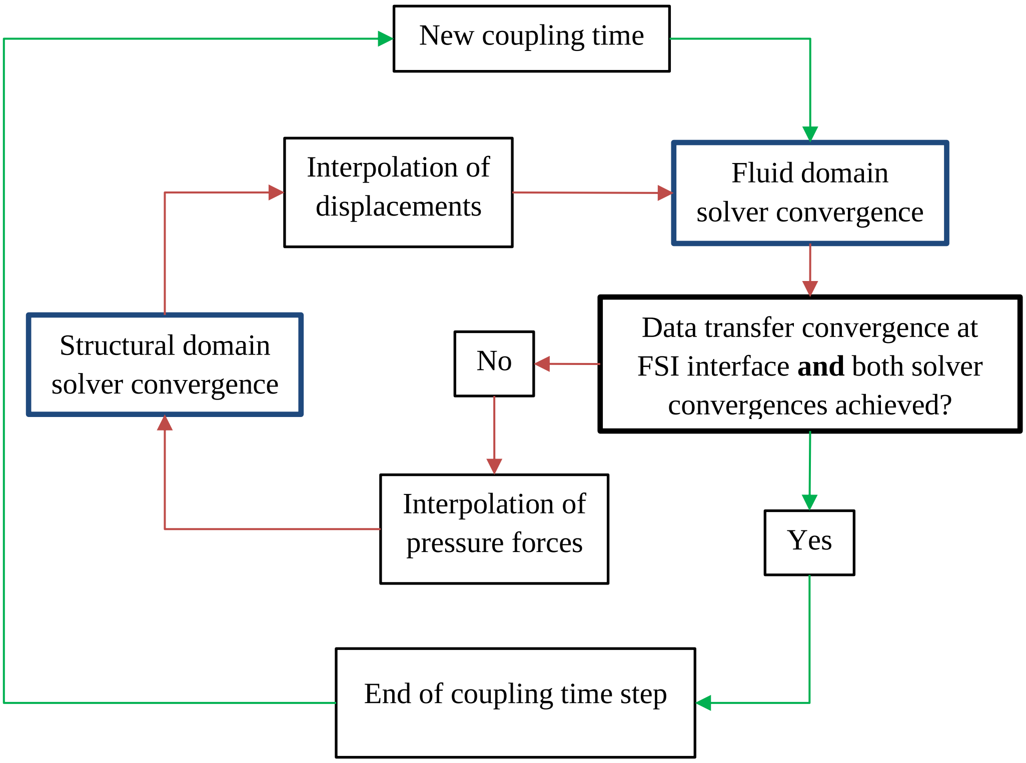

Figure 3.15. Two-way fluid-structure solver coupling in ANSYS Workbench overview

Firstly, data transfer regions need to be created in both the structural and fluid domains. In this case, this would be on the surface of the airfoil shaped rotor blade and the corresponding surface of the fluid domain it will be in contact with. Each surface can either be a source or a target depending on which way the data is being sent. Here, the fluid region will act as a source of transferring force (pressure) to the rotor blade and also act as a target for receiving incremental displacement from the blade. The rotor blade acts a source of sending incremental displacement to the fluid and a target that receives forces (due to the pressure field) from the fluid.

The coupled solving procedure starts with the convergence of the fluid domain in the first timestep. The pressures are then interpolated onto the rotor blade as pressure force boundary conditions. This results in deformation of the rotor blade mesh. The structural domain is then solved until a convergence criterion is met. The displacement of the rotor blade mesh is then interpolated onto the fluid domain which leads to the deformation of the fluid domain mesh and consequently a change in the pressure field. The change in the numerical value of the data transfer between the two domains over each system coupling iteration (per timestep) is recorded and when this change drops below a pre-determined convergence tolerance then system coupling convergence is achieved for that timestep. A new coupling timestep will only commence if the fluid domain, the structural domain and the coupling interface data transfers have met their respective residual tolerances otherwise, the coupling solver iterates until the maximum number of iterations per timestep has been reached.

This process is repeated for all timesteps. It must be noted that a minimum number of iterations can be set for the coupling solver, whereby a minimum number of iterations per timestep need to be performed before the timestep ends, even if all solvers have converged to their respective convergence criteria. By doing this, the option of linearly ramping the data transfer between the two solvers becomes available. This involves incrementally increasing the load transfer between the solvers until the minimum number of iterations have been met. This allows for a smaller and steadier perturbation to the quasi-equilibrium state of the system, especially in the case of large loads being transferred. Theoretically, this will decrease the inner-loop iterations per timestep, i.e. CFD solver and FEM solver, and lead to smaller computational solving time.

For the simulations to follow, the FSI solver is assigned a constant timestep size to properly synchronise the data transfer between the domains. The minimum and maximum coupling iterations for the *System Coupling* service relate to the number of iterations required at the fluid-structure interaction interface to achieve convergence of the data transfer between the two domains. The data transfer ramping option was enabled, as seen in Table 3.11, to steadily perturb each domain with the data transfer at the FSI interface until the full load is applied at the specified value for *minimum coupling iterations*. Table 3.11 shows the other coupling settings for the FSI simulations.

Table 3.11. System coupling settings

Setting	**Value**
Analysis time	Dependent on the rotational speed
Time step size	$8.8152E-5\ s$
Blade to fluid transfer RMS convergence tolerance	$1E-4$
Fluid to blade transfer RMS convergence tolerance	$1E-4$
Minimum coupling iterations	3
Maximum coupling iterations	5
Mesh deformation RMS residual target	$1E-6$
Mesh deformation minimum coefficient loops	3
Mesh deformation maximum coefficient loops	10

A very important consideration was the modelling of the mesh deformation. This was specified for the FSI simulations as well as the CFD-only simulations. The latter showed that no mesh deformation occurred during the simulations, as expected. The FSI case, however, solved for a deforming fluid mesh due to the forces exerted on the fluid through the motion of the rotor blade.

Simply put, the mesh stiffness can be set as variable or constant throughout the domain in CFX. A variable mesh stiffness is sought as it allows nodes in regions of high stiffness to move together. This preserves mesh distribution and quality which is particularly helpful in boundary layers. The mesh stiffness options available in CFX allow for either an increase in stiffness near small volumes; an increase in stiffness near boundaries; a combination of the previous two methods or a user-defined stiffness formulation.

After numerous tests, it was decided to make use of the stiffness formulation that was a function of the distance from small volumes based on the initial mesh. The determining factor of this was the small blade tip gap of $1\ mm$ and the number of small volume elements in this gap.

3.4 Preliminary Data Post-Processing

The FSI simulations were run for six BPPs at constant rotational speed, after which the first BPP data was removed due to reasons stated in section 0. Hence, a full rotation was simulated. Once again, the data had to be filtered using a lowpass filter due to the inclusion of numerical noise.

Numerical noise is an inevitable by-product of CFD simulations (Gilkeson *et al.*, 2014). The study by Gilkeson *et al.* (2014) highlighted that numerical noise is present due to the choice of turbulence model employed and the mesh used for the simulations. An example of the simulation data is shown in Figure 3.16 where the raw and filtered signals are shown. An in-depth look at these results will be presented in chapter 4. Figure 3.16 also shows the raw and filtered FSI pressure and fluid mesh displacement for a constant rotational speed of $1418\ rpm$. A 6th-order lowpass Butterworth filter was employed with a cut-off frequency of $1000\ Hz$. It is evident that a small amount of high frequency numerical noise is present in the pressure signal whereas the fluid mesh displacement signal contains less of this high frequency content.

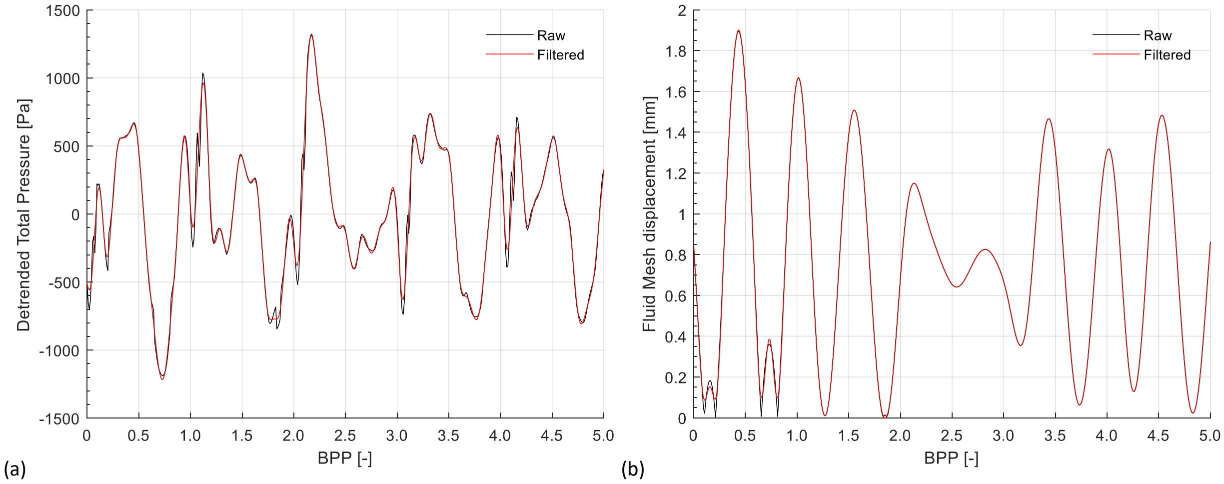

Figure 3.16. Filtering of FSI data: Total pressure on measured at the blade midpoint on the casing (a); Displacement of fluid mesh at blade tip (b)

3.5 Conclusion of Numerical Study Section

The numerical model and FSI data preparation are presented in this chapter. A simplified model of the experimental test bench is presented whereby a 72° annulus slice, or single blade passage, is modelled. Two rotor configurations are shown - a healthy configuration consisting of a single healthy rotor blade and a damaged configuration consisting of a single damaged rotor blade.

A mesh refinement study is presented for both the fluid and structural domain in terms of a steady-state CFD simulation and modal analysis, respectively, to determine adequate domain discretisation. A timestep sensitivity study is also presented for the fluid domain from which the minimum timestep for the FSI simulations was selected. Different solver types are also investigated for the structural domain.

Boundary conditions, as well as solver settings for the fluid, structural and FSI simulations, are presented. Lastly, some preliminary data processing is shown though the filtering of FSI simulation data due to the presence of numerical noise. An in-depth analysis of the FSI data is presented in chapter 4.

4 Discussion of Results

This chapter is the crux of what this study has set out to achieve - what blade condition information can we extract from a pressure field of a turbine stage passage when using a two-way fluid-structure interaction model. The results will be presented using experimental and numerical models, including CFD-*only* and FSI simulations. Firstly, the effect of the uncertainty in the measurement of inlet velocity is quantified. Secondly, validation of the FSI model in terms of the contents extracted from a CFD-*only* model as opposed to a similar FSI model are reviewed. Thirdly, the healthy rotor blade configuration analysis is presented as the main investigation. Lastly, a damaged rotor blade FSI model is reviewed in terms of the information that can be extracted from its flow field as supporting evidence to the claims made in the main investigation.

Validation is a key component of any numerical model as one has to assess how well the physics of a real-world problem or experiment are captured. As a numerical model will always include some set of assumptions made to model certain aspects of a problem, differences in numerical and experimental results are expected. Validation, therefore, also assists in quantifying the effect that these assumptions make on the numerical model results in comparison to experimental data.

Certain assumptions were made when developing the FSI model as mentioned in previous sections. These assumptions were made to better represent an actual turbine blade passage than what was available in the experimental test rig. These assumptions, as well as differences between the FSI model and experimental test turbine, are outlined below to remind the reader:

- *Inlet flow boundary condition:* A constant, uniform inlet velocity is used for the FSI model. This inlet velocity is prescribed perpendicular to the inlet boundary at $65\ m/s$ - similar to the experimental tests. The air is supplied to the experimental test rig through a single nozzle, as mentioned in section 2.1. The inlet airflow in the FSI model is modelled as a uniform flow field of 20%, or one fifth, of the annular area of the experimental test turbine at the same velocity. It is expected that this would result only in larger response magnitude of both the pressure field and blade motion than would be the case for the experimental results.
- *Defeaturing of the blade geometry:* As mentioned in section 3.2.1, the numerical blade was defeatured by removing the base of the blade that attached to the hub as well as the fillets between the blade and the base. This reduced the geometrical stiffness of the blade and led to the altering of the elastic modulus of the blade material to match the first natural frequency of the experimental blade. The blade's displacement response is, however, still expected to be larger in magnitude than the experimental blade.
- *Damping of the blades:* The damping coefficient of the experimental blades was not known, and determination thereof was excluded from this study. Thus, the numerical blades excluded damping in the simulations. This, of course, would result in differences between the experimental and numerical datasets, in terms of frequency content, but they will still be comparable.
- *Simulating a single passage and single blade:* This modelling decision leads to the assumption that the fluid flow and blade vibration is identical in each passage. This would not be an exact representation of the physical setup, especially in the case of the damaged blade simulations.

4.1 Uncertainty Quantification of Effect of the Inlet Air Velocity

The inlet velocity to the turbine stage that was measured experimentally had some degree of uncertainty in the measurement. The measured velocity of 65 m/s was used in the simulations assuming that the amount of energy transferred to the rotor blades would only change the magnitude of the blade's response and not the frequency content of the flow field around the blades. As all following simulations would use the same inlet velocity, it became necessary to justify this assumption. It would be preferable to use the largest possible excitation velocity, but not larger than the experimentally measured velocity, to produce the largest blade response. This would allow for clear distinctions of the pressure field characteristics in both the time and frequency domains.

A rotational speed of $1215\ rpm$ was used for inlet velocities of $65, 52$ and $41.6\ m/s$. The rotational speed was set equal to a critical speed using equation (28) coinciding with the $10^{th}\ EO$, i.e. the first harmonic of the blade passing frequency. The inlet velocities were reduced twice by 80% from the measured speed of 65 m/s. These simulations were carried out using the healthy blade geometry.

Figure 4.1 and Figure 4.2 show the total pressure and fluid mesh displacement, respectively, at selected monitor points (see Figure 3.9). From here on afterwards the monitor point located at the centre of the blade on the casing will be referred to as the casing monitor point, similarly, the monitor point located at the centre of the blade midway between the blade tip and casing will be referred to as the midway monitor point.

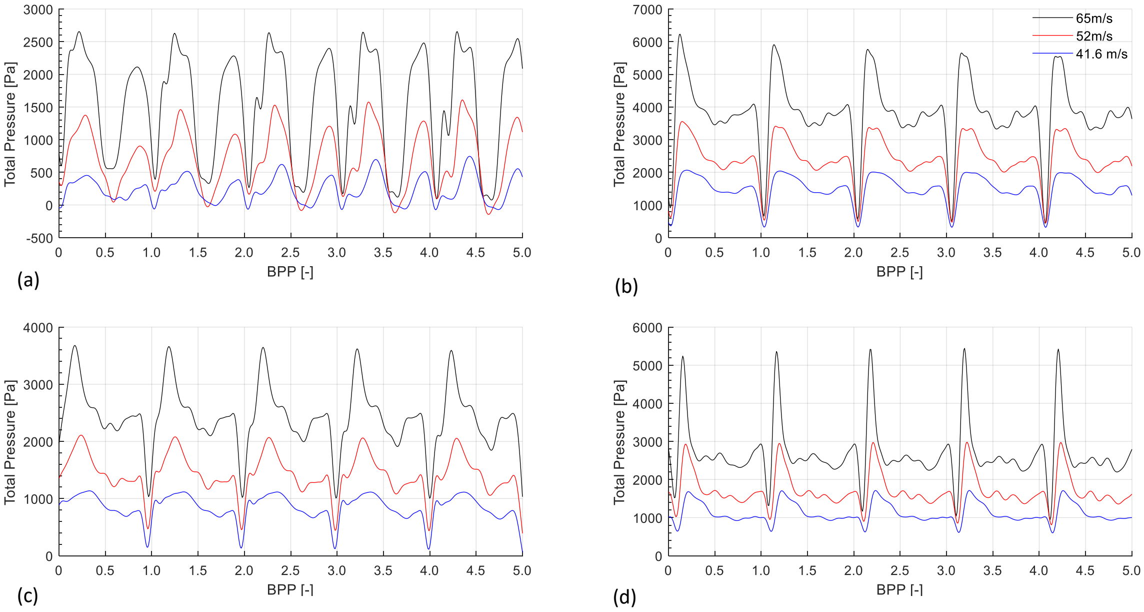

Figure 4.1. Total pressure signals at the: casing (a); midway point (b); LE (c); TE (d) for the FSI simulations pertaining to the uncertainty quantification of effect of the inlet velocity.

Examining Figure 4.1, a tentative conclusion can be made about the postulate that only the pressure magnitude changes as a function of the inlet velocity to the turbine stage. The general trend of the pressure is relatively consistent with a decrease in inlet velocity. It is, however, evident that some of the micro fluctuations in the pressure profile are lost. The high-frequency content is expected to have smaller amplitudes for less energy entering the system, hence the diminishing micro fluctuations.

Similar observations are made for the fluid mesh displacement in Figure 4.2. The general trend of the displacement profiles is consistently reduced for lower inlet velocities. There are, however, negligible micro fluctuations present in the displacement profiles. The general trend of the displacement profiles can be seen to increase over time. Negligible structural damping together with rotating the blade at a critical speed, i.e. a speed that is an integer multiple of the natural frequency of the blade, would result in resonance. If the simulation were to be carried out over a longer simulated time, an even larger displacement response amplitude will be seen. The motion of the blade is due to superposition of structural and aerodynamic loads imposed on the blade. The two key contributions to this blade motion are the disturbances caused by the rotor blade passing the stator blades; and the shaft rotational speed.

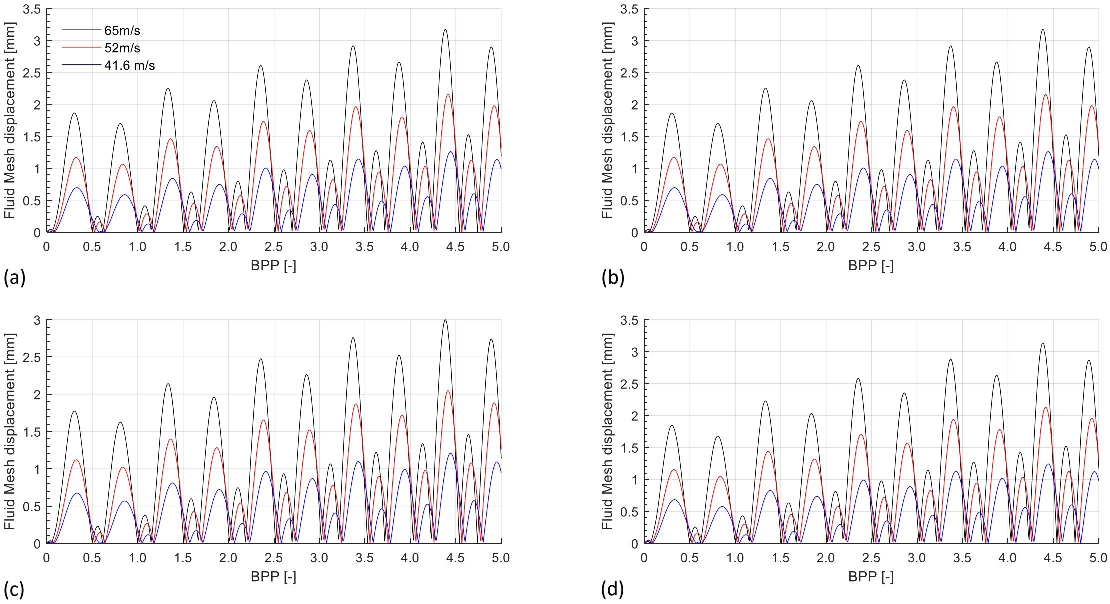

Figure 4.2. Unfiltered fluid mesh displacement at the: casing (a); midway point (b); LE (c); TE (d) for the FSI simulations pertaining to the uncertainty quantification of effect of the inlet velocity.

The frequency spectra for the casing pressure and fluid mesh displacement are portrayed by FFT magnitude and phase angle diagrams in Figure 4.3. Three dominant frequencies are observed when viewing the pressure signal spectrum. These are the BPF and two of its harmonics at $101.4, 202.8$ and $304.3\ Hz$, respectively. The frequency of $202.8\ Hz$ coincides with the first natural frequency of the blade. The dominant frequencies present in the displacement spectra are, however, located at the shaft rotational speed and then again, at the first natural frequency of the blade. This is also the ninth harmonic of the rotational speed frequency or the tenth EO of the system.

Phase changes of $\pm 90°$ and larger than $90°$ can be observed in the spectra of Figure 4.3 which indicate that the fluid is being excited at more than one frequency. In fact, the fluid is being excited by the harmonics of the shaft rotational speed and, more specifically, the BPF and its harmonics. The phase changes of $\pm 90°$ indicate that the fluid is being excited at a critical frequency. In this case, it is the BPF of the blade that can be seen in the pressure and fluid displacement spectrum. The phase changes that are larger than $90°$ occur at the blade's natural frequency and suggest that the response is slightly dampened. The response of the blade is in fact lightly dampened by the fluid.

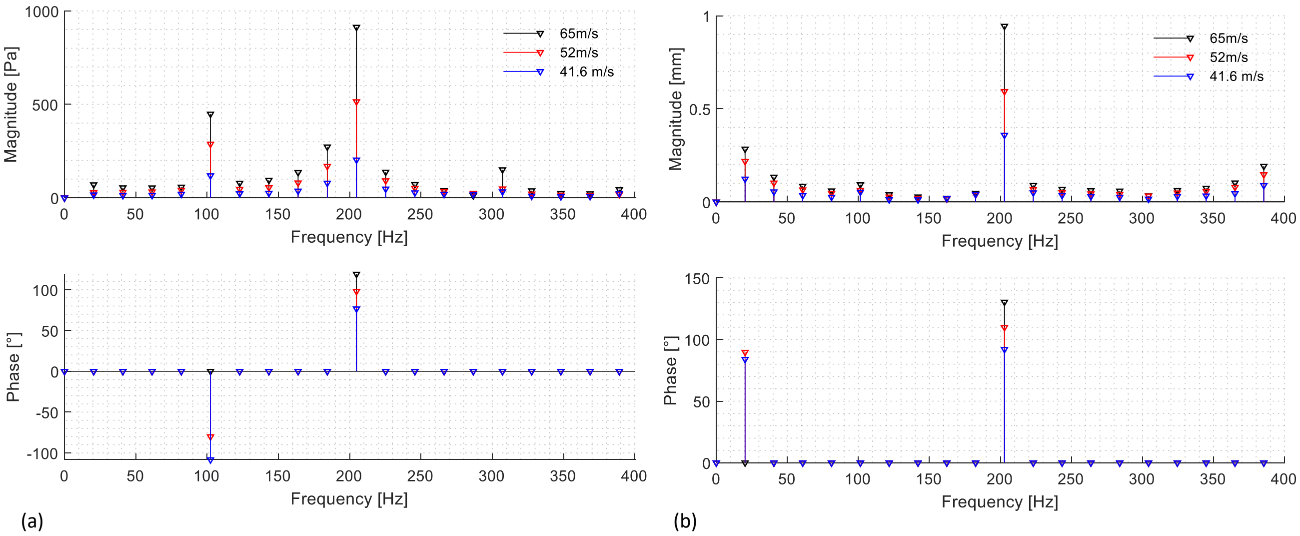

Figure 4.3. FFT plots of fluid casing monitor: total pressure (a) and fluid mesh displacement (b) for the FSI simulations pertaining to the uncertainty quantification of effect of the inlet velocity.

Both spectra shown in Figure 4.3 have consistent frequency content with, again, lower magnitudes associated with the smaller inlet velocities. This proves that the previously made assumption is adequate as the inlet velocity only influences the magnitude of the response and, for the given ranges tested, the distribution of the frequency spectra remain unaffected. Thus, the remainder of all FSI and CFD simulation results that are presented make use of an inlet velocity of $65\ m/s$.

4.2 Healthy Blade Analysis

This section presents an in-depth analysis of the experimental and simulation results for the healthy blade configuration. A brief comparison of the FSI and CFD-*only* pressures is also presented to highlight certain characteristics present in the FSI model's flow field. The analysis is split up into two major categories: varying rotational speed and constant rotational speed.

4.2.1 Varying Rotational Speed Investigation

It is well known that a blade's natural frequency increases as the shaft rotational speed increases. This phenomenon is caused by the centrifugal stiffening of the blades and is usually visualised using a Campbell diagram, also known as a frequency-RPM map. The results presented in this section serve as evidence that, although there are assumptions made in the numerical model, the underlying principles of the numerical model and experimental turbine are consistent.

Two datasets were obtained from the experimental tests, namely, casing sound pressure and casing acceleration. The frequency spectra of the varying rotational speed tests are studied for the possible generation of a frequency-RPM map to identify the natural frequency of the blades as a function of rotational speed. This will serve as a guideline as to what can be expected for simulation results. Figure 4.4 shows the frequency-RPM map for the healthy configuration experimental casing pressure signal. The frequency map of the microphone pressure data can be seen to have five distinct bands of peaks. The largest of these (on the left of the graph) represents the BPF as a function of the rotational speed. The remaining bands represent the harmonics of the BPF as functions of rotational speed. Unfortunately, this is the only blade condition information that the experimental pressure data contains. The blade natural frequencies could not be obtained from the microphone data. It is believed that the sensitivity of the microphone could be too low. Making use of either a more sensitive microphone, or pressure transducer, or increasing the air flow through the test turbine should allow for the detection of the blade natural frequency. Although the natural frequencies are detected by the accelerometer as will be discussed in detail next, more evidence is needed to confirm the hypothesis that the pressure measuring sensor can detect local blade condition information.

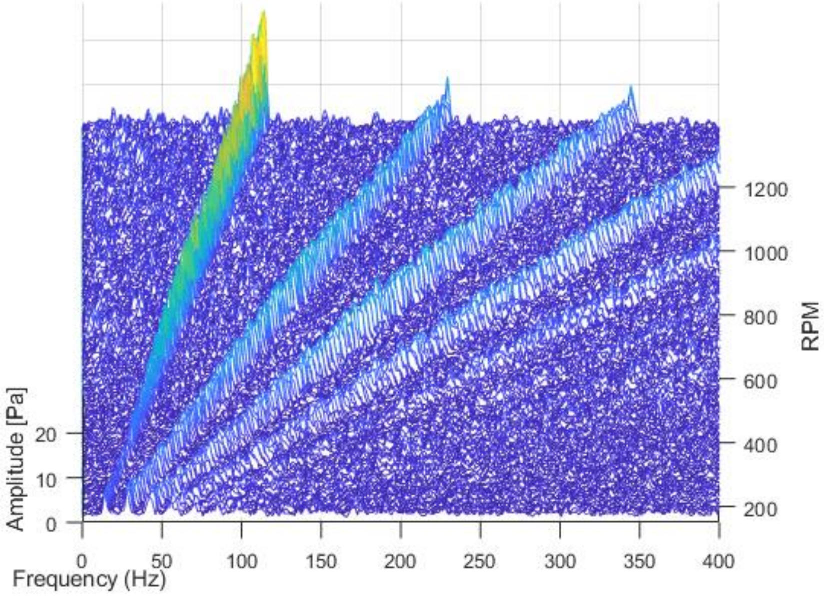

Figure 4.4. Frequency-RPM maps for the healthy configuration experimental casing pressure.

Viewing the frequency map of the casing accelerometer data in Figure 4.5, a distinct difference is observed when compared to the casing pressure frequency map. A multitude of diagonal bands of peaks fan over the frequency map, just the same as for the pressure data. These bands are identified as the EOs of the rotational speed. Two other frequencies that are can be seen as vertical lines in the frequency spectra are located at $\sim 74\ Hz$ and $\sim 114 Hz$. These frequencies are not a function of the rotational speed and are therefore inherent natural frequencies of the experimental test turbine structure.

A fair number of peaks are present in the region of $200 - 230\ Hz$. These peaks occur at rotational speeds that coincide with EOs that are closely related to the blade passing frequency. These peaks thus occur at critical speeds and the frequencies associated with them are the natural frequencies of the blades. The centrifugal stiffening effect on the blades is clearly seen in Figure 4.5, although this is not the only load that contributes to the increased stiffness of the blades as pressure forces increase the preload on the blades. The significant peaks were extracted and are shown in Figure 4.5 (a). The estimated natural frequency shift with rotational speed can be seen in Figure 4.5 (b). The numerical values of the experimental blade in Figure 4.5 (b) can be viewed in Appendix B: Natural Frequency Evolution of the Healthy Experimental Blade.

No variable rotational speed simulations were performed purely due to the amount of time it would take to solve. Instead, a modal analysis was performed on the single defeatured numerical blade by pre-stressing it with a load resulting from the applied rotational velocity to create a Campbell diagram. The numerical blade's natural frequency is also expected to increase for larger rotational speeds. It is, however, expected that the natural frequency variation over tested rotational speeds will not be as large as the variation of the experimental turbine. A number of factors influence this natural frequency variation such as structural damping (which is excluded), the pressure load from the upstream flow over the stator blades and how this provides a preload to the blade and lastly, the viscous damping provided by the flow in simulations will be higher due to a full-field inlet flow being modelled as opposed to the single nozzle used for the experiments.

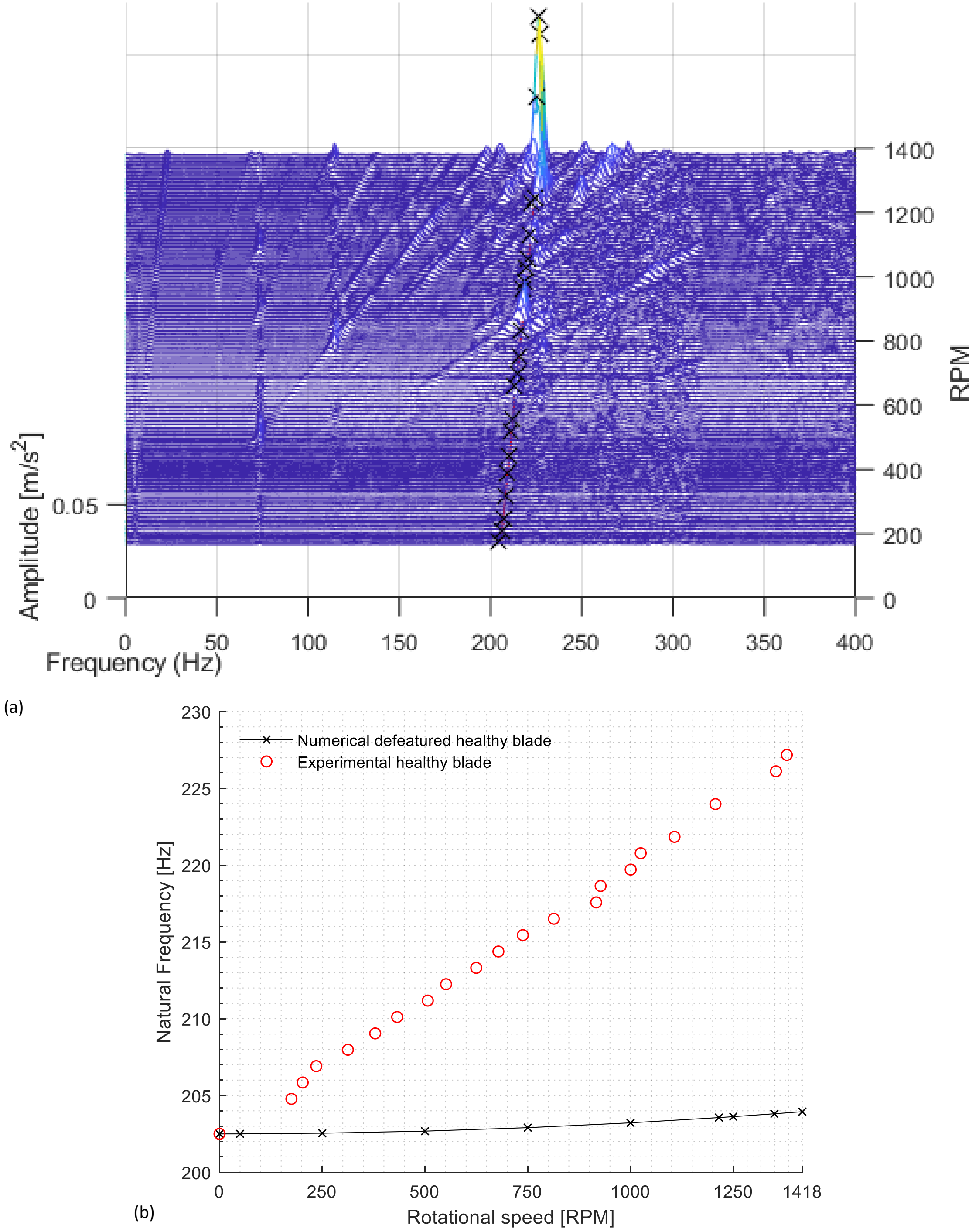

Figure 4.5. Natural frequency peak detection of healthy blade configuration: frequency-RPM map showing significant peak locations (a); peaks extracted from (a) to estimate blade natural frequency as a function of rotational speed for the experimental blades as well as the numerical blades (b).

Figure 4.5 (b) also shows the Campbell diagram of the healthy numerical blade and the evolution of the first natural frequency. It is evident that there is some sort of evolution of the blade's natural frequency with an increase in rotational speed. It is, however, not nearly as much as that experienced by the experimental blades. The frequency only increases by approximately $1.45\ Hz$, whereas the experimental blade's frequency increased by approximately $24.7\ Hz$. This serves as a guideline for the analysis of the FSI model's pressure field when driven by a constant rotational speed in the next section. The frequencies of interest, i.e. the natural frequency of the blade, should be expected on the lower end of the spectrum range, near the static natural frequency.

A last important note regarding the natural frequency evolution with rotational speed is that a specific critical speed will not occur at the same EO for the experimental and FSI models. For instance, the critical speed of $1350\ rpm$ is linked to a 10^{th} and $9^{th}\ EO$ excitation for the experimental turbine and the FSI model, respectively, for corresponding natural frequencies of $224.6\ Hz$ and $203.6\ Hz$. This can be verified through equation (28).

4.2.2 Constant Rotational Speed Investigation

As a turbine is designed to run at a constant or steady-state speed, it becomes attractive to focus on the frequency spectra at such operating conditions. It is advantageous to be able to monitor the frequency spectra at a specific speed as any deviations from a baseline spectrum would indicate that something has changed in the system. Before comparing the frequency spectra of the FSI model's pressure field to the experimental results, it is necessary to examine the relationship between the blade vibration and the change in pressure around the blade. The intention hereof is to gain a deeper understanding of flow field in a two-way FSI model.

4.2.2.1 Comparison of the FSI and CFD Flow Fields

Considering a single blade passing period. It may be expected that the rotor blade will respond as it passes a stator blade. The corresponding pressure profile close to the tip of the blade should follow the same trend, after all, Alshroof *et al.* (2012) proved this in their study. This can be illustrated by the blade-to-blade contour plots of the total pressure at the midspan of the stage through a single BPP in Figure 4.6. It is clear that there is a disturbance in the pressure field downstream of the rotor blade as it passes through the trailing wake of the stator blade. The inlet flow is prescribed perpendicular to the stator inlet face to allow for larger flow-induced vibration of the rotor blades. A recirculation zone forms behind the rotor blade due to the stagger angle of the blades and the direction of the inlet flow and is linked to how the flow dampens the blade's response.

The viscous damping of the fluid affects the rotor blade response leading to the oscillations diminishing as the rotor blade approaches the next stator blade. This is then repeated for the next blade. If there is not enough damping, the transient response continues beyond the blade passing period. This is, however, dependent on the inlet flow velocity and the rotational speed of the rotor. In this case, the pressure profile for the next blade passing period will be combined with the previous passing period's response and the signal would seem to be erratic.

This concept is better visualised by considering the transient pressure profile at a single point. A FSI and CFD-*only* simulation were run at different speeds - $1418\ rpm$ and the critical speed of $1215\ rpm$. The results for the total casing pressure are shown in Figure 4.7 as well as the arithmetic difference between the two signals for two different rotational speeds. A clear, repetitive trend is seen for the

CFD-*only* pressures for both rotational speeds. The fluid dampens out the blade passing effect on the pressure profile as there is no opposing force from the blade in this case.

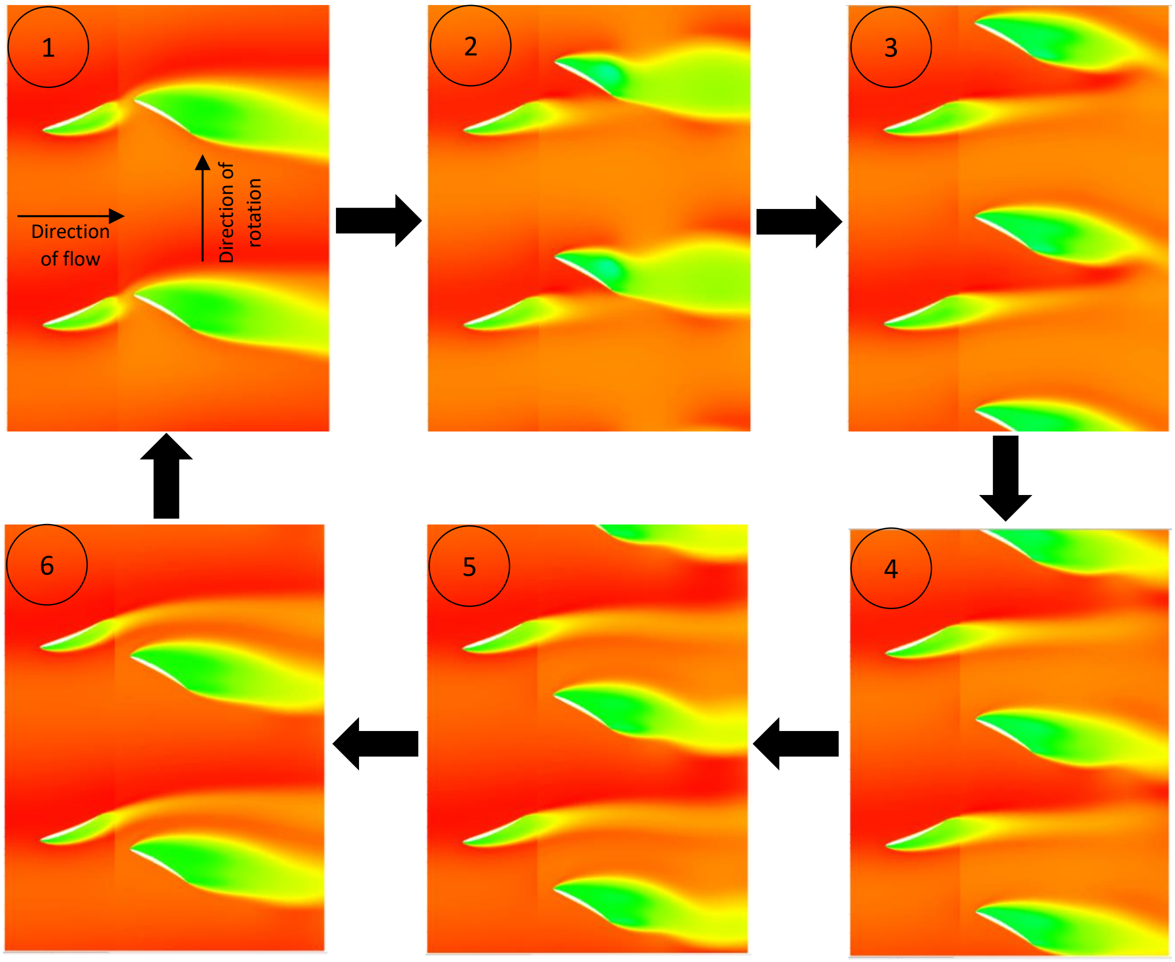

Figure 4.6. FSI blade-to-blade contour plots of the total pressure at the midspan of the stage through a single BPP.

The FSI pressure profile is somewhat different for the two rotational speeds. The FSI pressure profile is also relatively consistent for each BPP for the critical speed, i.e. 1215 rpm. This is due to the blade being excited at its natural frequency as the critical speed is a harmonic of the BPF, and this in turn is equal to the natural frequency of the blade. The speed of 1418 rpm is not a harmonic of the BPF and neither is any of its harmonics equal to the natural frequency of the blade.

Emphasis is placed on Figure 4.8 to further explain the differences in the pressure signals. The spectrum of the maximum speed case displays harmonics located in close vicinity to the blade's natural frequency. The 8^{th} and 9^{th} EO are located at 189.1 Hz and 212.7 Hz, respectively. These frequencies are close to the natural frequency of the blade, but not close enough to cause even low amplitude resonance, which is clearly absent in Figure 4.8 (b). The critical speed's spectrum includes two significant frequencies, the BPF and its first harmonic, located at 101.3 Hz and 202.5 Hz, respectively. The fewer forcing frequencies present in the critical speed's pressure spectrum, and their relation to the blade's natural frequency, results in a smoother profile. The opposite is true for the maximum speed case where the number of significant forcing frequencies are larger together with the larger centrifugal forces caused by the rotational velocity subdue the viscous damping effect of the fluid. This results in an irregular pressure profile.

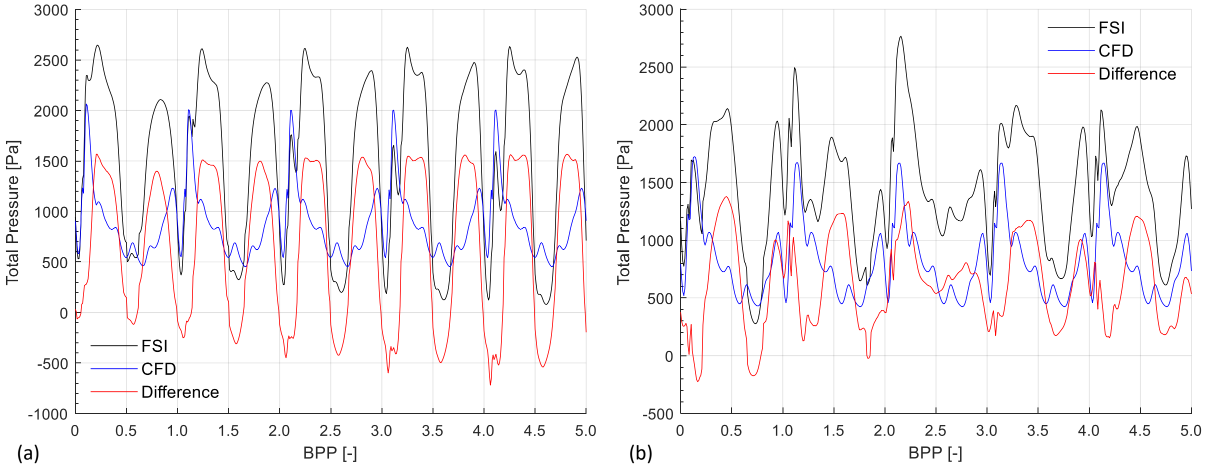

Figure 4.7. Casing pressure comparison for FSI and CFD-only simulations at: $1215\ rpm$ *(a);* $1418\ rpm$ *(b)*

Studying the difference of the FSI and CFD-*only* pressure profiles, a similar conclusion can be made. The pressure differences shown in Figure 4.7 are essentially the pressure changes produced by the pressure force exerted on the fluid by the blade only. It is clear that the blade motion, or pressure force, makes a significant contribution to the FSI model's pressure profile. Viewing the spectra of the

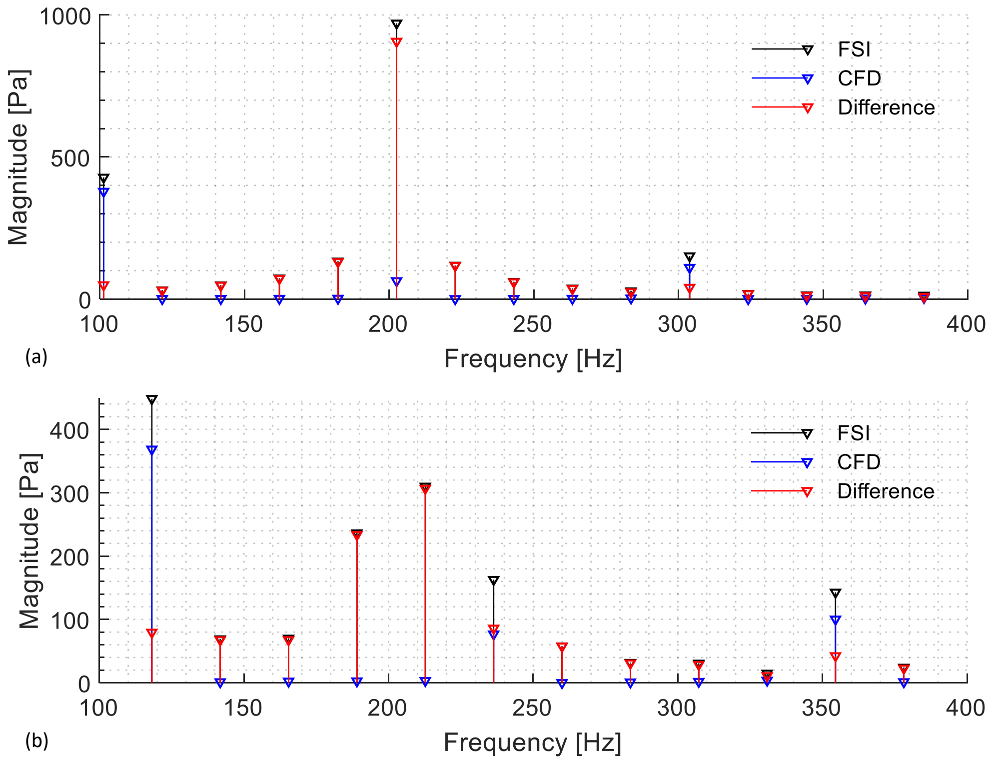

Figure 4.8. FFT magnitude of the casing pressure for FSI and CFD-only simulations at: $1215\ rpm$ *(a); 1418* rpm *(b).*

pressure differences in Figure 4.8, the contributing frequencies of the blade's pressure force exerted on the fluid are clearly seen. The CFD-*only* pressure profile includes only the BPF and its harmonics. Thus, the major driving frequency in the pressure field is that produced by the pressure force of the rotor blade. Hence, it can be tentatively concluded that blade condition information can be seen in the pressure field. It is, however, necessary to investigate this claim further.

4.2.2.2 Comparison of the FSI Model and Experimental Results

A number of FSI simulations were run at constant rotational speeds. The speeds tested are the maximum speed imposed by the limits of the experimental test turbine of $1418\ rpm$; the critical experimental speed of $1350\ rpm$; and the critical numerical speed of $1215\ rpm$. The former and second-to-last speeds relate to the $10^{th}\ EO$ excitation of the experimental and FSI models' blades, respectively. These critical speeds differ, although they represent the same EO excitation for the different data compared here. This is due to the differences in the blades' natural frequency at higher rotational speeds as discussed in section 4.2.1. The data will, however, be compared on a speed-for-speed basis.

The spectrum magnitude and phase information of the maximum speed's experimental casing pressure can be seen Figure 4.9. As mentioned in section 4.2.1, the experimental pressure spectrum only contained BPF information for the variable speed tests as it is believed that the sensitivity of the microphone was too low. This is again the case for the constant rotational speed pressure spectrum. The blade passing frequency and its harmonics are the only significant frequencies present in the experimental casing pressure spectrum. The phase angle diagram supports this claim. Therefore, the experimental casing pressure will not be investigated any further for the remainder of this study.

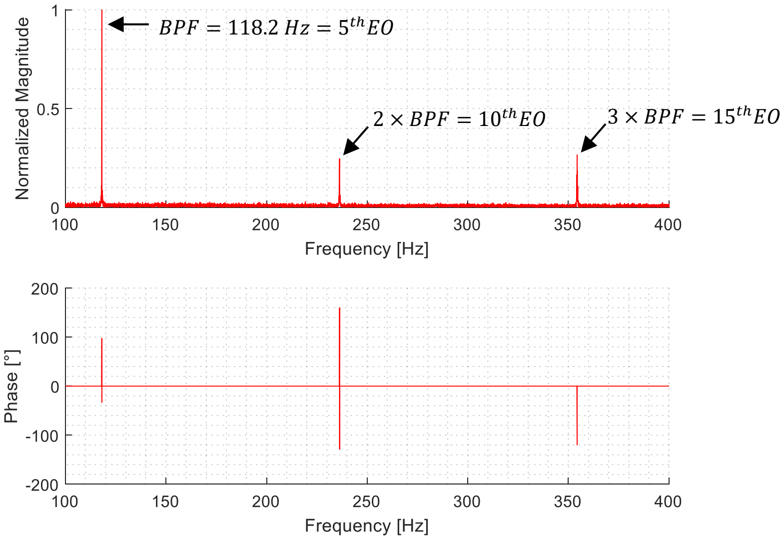

Figure 4.9. FFT magnitude and phase information of the experimental casing pressure at 1418 rpm

The spectrum magnitude of the maximum speed's FSI casing pressure and experimental casing acceleration can be viewed in Figure 4.10. The accelerometer picked up a multitude of significant frequencies in the system. These include the 5^{th}, $10^{th}$and $12^{th}\ EOs$. A frequency of $204.8\ Hz$ is also captured signifying possibly the static natural frequency of one of the rotor blades. This claim is, however, unverified. The frequency of $228.6\ Hz$ is the natural frequency of the rotor blades at a speed of 1418 rpm. This is supported by the findings of the natural frequency estimates in Figure 4.5 of section 4.2.1. The 10^{th} EO frequency (first harmonic of the BPF) is relatively close to the experimental blade natural frequency and therefore results in the resonating the blades, but not at full amplification.

The FSI casing pressure spectrum at this speed, however, does not contain such a large, significant frequency denoting the natural frequency of the blade. This is due to a variety of factors influencing the blade's stiffness as explained in section 4.2.1. The spectrum of the maximum speed case does, however, have harmonics located in close vicinity to the blade's natural frequency as explained in section 4.2.2.1. The 8^{th} and 9^{th} EO are located at 189.1 Hz and 212.7 Hz, respectively. These frequencies are not in the region of resonance of the blade to lead to any form of forced harmonic vibration.

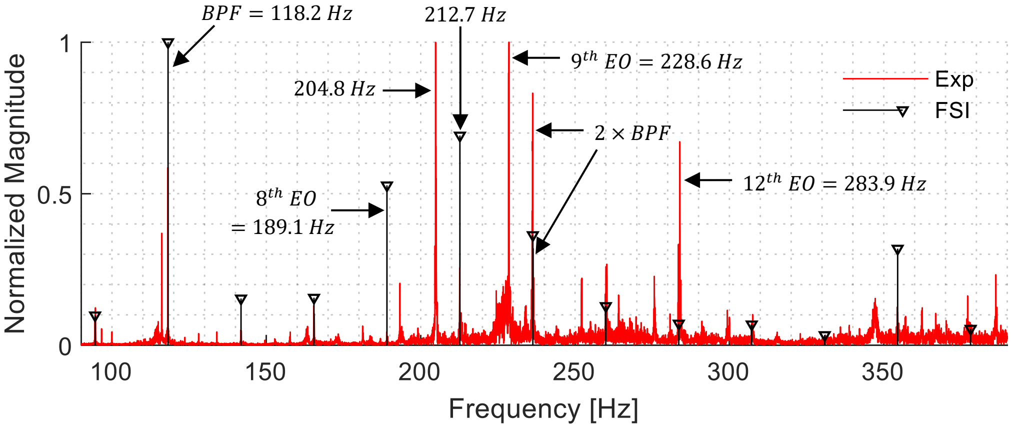

Figure 4.10. FFT magnitude of the FSI model casing pressure and experimental casing acceleration at 1418 rpm for the healthy configuration.

The experimental blade's natural frequency is also clearly seen in the casing accelerometer's spectrum located at 228.6 Hz. The BPF and its first harmonic appear in both spectra and in general, the spectra are in agreement putting aside the differences created through the assumptions made in the FSI model.

The next rotational speed that will be analysed is the experimental critical speed of 1350 rpm. The experimental and numerical blades are excited by different EOs. For this speed, the 9^{th} EO excites the numerical blade and the 10^{th} EO excites the experimental blades due to the way in which the natural frequencies evolve with rotational speed. This is clearly seen in the spectra of Figure 4.11. Also shown in this figure, is the experimental casing acceleration spectrum magnitude for this critical speed. In general, the harmonics of a base frequency reduce in amplitude the higher the order of the harmonic is. If the amplitude of a harmonic is larger than the base frequency, it is an indication that there is another component in the system that is vibrating at this frequency. This is seen in the spectrum of the accelerometer's signal. The 2^{nd} harmonic of the BPF can be seen to have the largest amplitude for the experimental results. The blades are being excited at this EO as the rotational frequency harmonic coincides with the natural frequency of the blades at this specific rotational speed.

The FSI casing pressure spectrum shows similar tendencies. The largest peak occurs at the $9^{th}\ EO$, corresponding to a frequency very close to the static natural frequency of the blade. This inevitably causes the blade to vibrate close to its natural frequency - again not at maximum amplification as this is not a strong harmonic. This claim is again supported by the fact that a higher order harmonic of the rotational frequency has a larger amplitude compared to the rest of the spectrum, and thus there is more than one component contributing to its amplitude for that specific frequency.

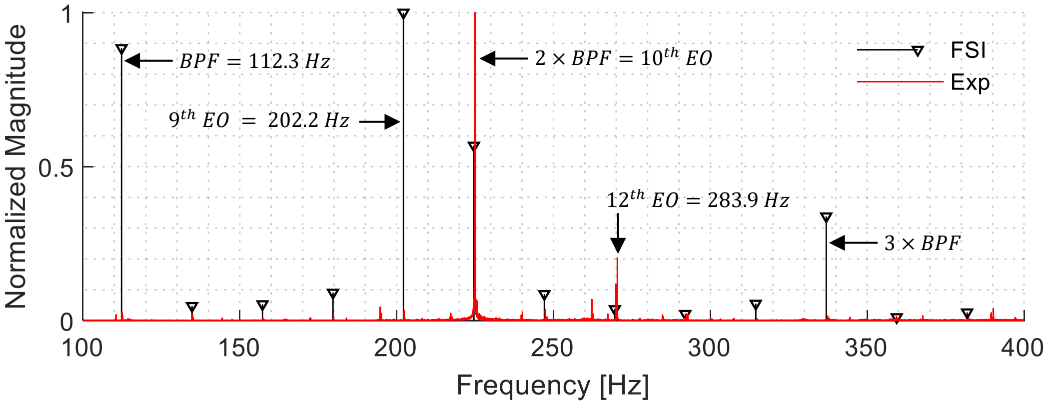

Figure 4.11. FFT magnitude of the FSI model casing pressure and experimental casing acceleration at 1350 rpm for the healthy configuration.

The final rotational speed that will be analysed is the numerical critical speed of $1215\ rpm$. Here, the $10^{th}\ EO$ excites the numerical blade and the $11^{th}\ EO$ excites the experimental blades. This is clearly seen in the spectra of Figure 4.12. Yet again, higher order EOs, specifically the 10^{th} and 11^{th}, have larger amplitudes than the lower EO frequencies for each set of data, respectively. This leads to the finding that there is another component in the system that is vibrating at this frequency. This is seen in both spectra shown in Figure 4.12.

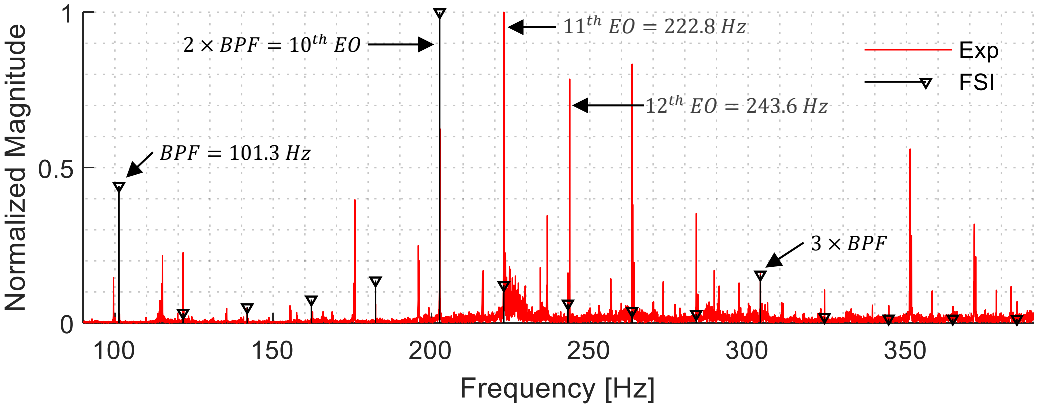

Figure 4.12. FFT magnitude of the FSI model casing pressure and experimental casing acceleration at 1215 rpm for the healthy configuration.

Similar findings are observed in the FSI casing pressure spectrum. The largest peak occurs at the $10^{th}\ EO$, corresponding to a frequency of $202.6\ Hz$ which, is essentially the natural frequency of the blade. This causes the rotor blade to resonate. This EO is the only significant frequency in the spectrum within a few EOs for this critical speed, unlike the previous two speeds analysed. This is again the case of having more than one component contributing to the amplitude of this specific frequency, being, the EO excitation frequency of the shaft and response frequency of the blade.

Reviewing the three speeds analysed, i.e. 1418 rpm, 1350 rpm and 1215 rpm, the latter rotational speed is the only speed to have caused the healthy numerical blade to resonate at full amplification at its natural frequency which is picked up in the pressure field of the FSI model. The speed of 1350 rpm excited the blade, but at a low amplification factor, whereas the maximum speed of 1418 rpm did not excite the blade at all as none of its EOs coincided with the blade's natural frequency. This statement is supported by the transient pressure profile as well as the transient fluid mesh displacement profile of the FSI model at the casing monitor point. Both of these profiles can be seen for the different rotational speeds tested in Figure 4.13.

It is clear that for the speed of 1215 rpm, both the pressure and displacement profiles "*blow up*" - the responses diverge due to the blade resonating at its natural frequency, whereas the responses of the other two speeds are dampened out due to the weak EO driving frequencies. This is confirmation that blade condition information can be detected in the pressure field of a two-way FSI model. The blade condition information that was extracted from the pressure field is the resonance frequency of the blade, which in each case, coincided with an EO. Collectively, this type of forced vibration can be termed ultra-harmonic, or harmonic multiple forced vibration.

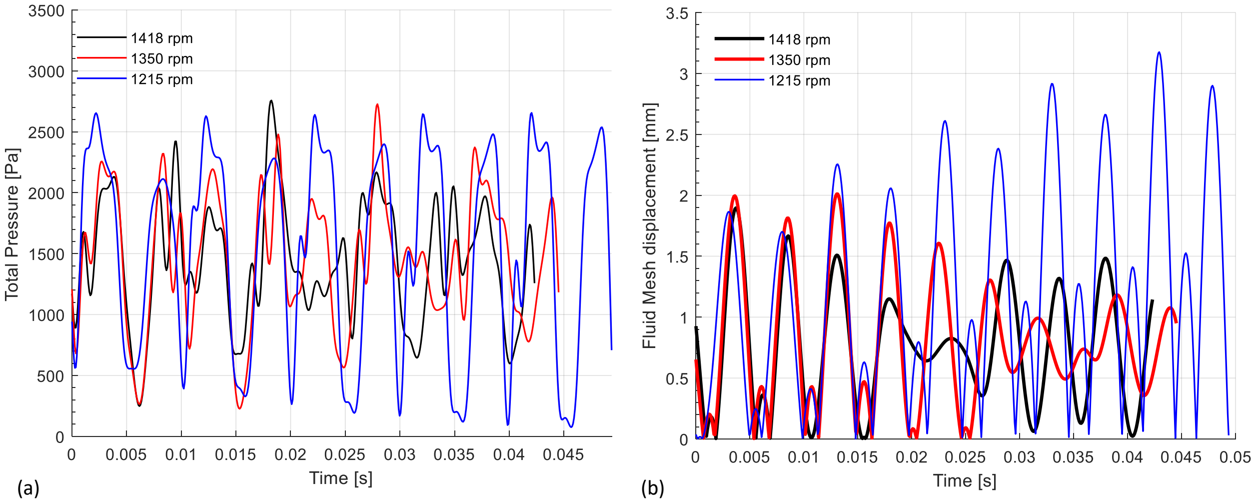

Figure 4.13. FSI casing: pressure (a) and fluid mesh displacement (b) transient profiles for different rotational speeds of the healthy rotor blade.

Synchronous vibration, or EO vibration, is a major component in turbomachinery vibration. This has been highlighted in this section. Even if the base forcing frequency - the rotational speed - is not near the natural frequency of the blade, the EO frequencies that are in close vicinity of the blade natural frequency lead to either an amplified response of the blade or to the resonance of the blade. This is, however, dependent on the strength of the harmonic and whether it is a harmonic of the blade passing frequency. This is shown experimentally and numerically through CFD and FSI model comparisons.

4.3 Damaged Blade Analysis

This section presents the analysis of the experimental and simulation results for the damaged blade configuration. This can be considered supplementary to the Healthy Blade Analysis of section 4.2.

The damaged rotor configuration of the experimental turbine consisted of four healthy blades and a single damaged blade. The damaged blade consisted of the same profile as the healthy blade, but its thickness was reduced by 30%. The damaged blade FSI model was set up identically to the healthy blade model. Setting up the model as such assumes that identical flow profiles exist in each blade passage as all the rotor blades have the same reduced thickness profile. Hence, comparing the FSI model to the experimental results will be problematic.

The secondary objective of this study, minimising the computational effort, affected how the final FSI model would be set up, bearing in mind the consequences that it would have on certain analyses. That being said, the experimental and numerical results will be uncoupled and analysed such that the similarities and differences in the datasets are exemplified.

4.3.1 Experimental Data Investigation

There is an expectation of what the spectra will reveal prior to generating the frequency-RPM maps of the experimental casing pressure and acceleration signals. The spectral map of the casing pressure is not shown here as it again only shows the blade passing frequency accompanied by four of its harmonics with nothing related to the local rotor blade response. One would expect the casing accelerometer to show clear information of the healthy and damaged blades. The spectral map of the casing accelerometer, however, seems quite similar to the healthy blade configuration spectrum. Both of these spectral maps are shown in Figure 4.14.

There is no clear indication of the local mode of the first natural frequency for the damaged blade in the spectral map of Figure 4.14 (b). Instead, the presence of a large number of small undulations can be seen around the frequency of $115\ Hz$ and in the range spanning from $190\ Hz$ to $315\ Hz$. In fact, what is actually observed here, are the global modes of the system - the measured spectrum corresponds to the structure's global dynamics rather than the local behaviour of a single damaged blade. This does, however, indicate that something in the system has changed, which in this case refers to the inclusion of a single damaged rotor blade.

This finding epitomises the challenging situation of comparing the numerical and experimental data. To gain more insight into the local behaviour of the damaged blade, one would perhaps have to instrument the blade directly with strain gauges. This creates another challenge as a more advanced telemetry system will have to be used to allow for data transmission while the turbine is in operation. These problems can also, however, be alleviated through the use of an adequately sensitive casing microphone or pressure transducer. Usage of a BTT technique could also be a viable alternative.

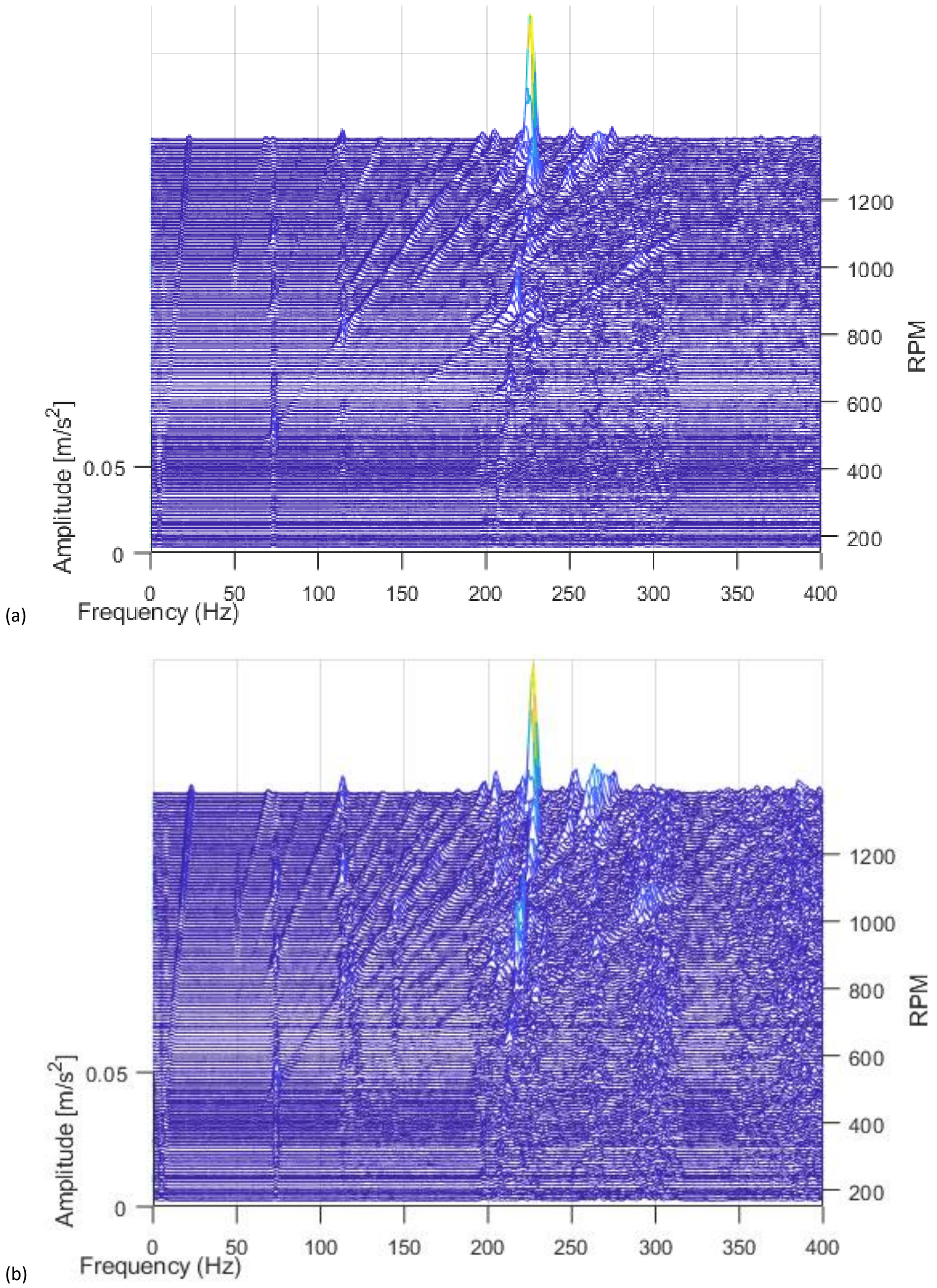

Figure 4.14. Frequency-RPM maps for the experimental casing acceleration of the: healthy (a); and damaged (b) rotor configurations.

To further investigate the spectrum of the casing acceleration, constant rotational speed data will now be presented. Figure 4.15 shows the spectra of two different rotational speeds' casing acceleration. It is clear that a majority of EO frequencies are present in the spectra. There is, however, no clear suggestion of either of the blades' natural frequencies - although the healthy blade's natural frequency has been marked due to prior knowledge of its shift with rotational speed. Thus, advanced signal processing techniques would have to be used to extract useful information as well as perhaps the use of other vibration measuring techniques.

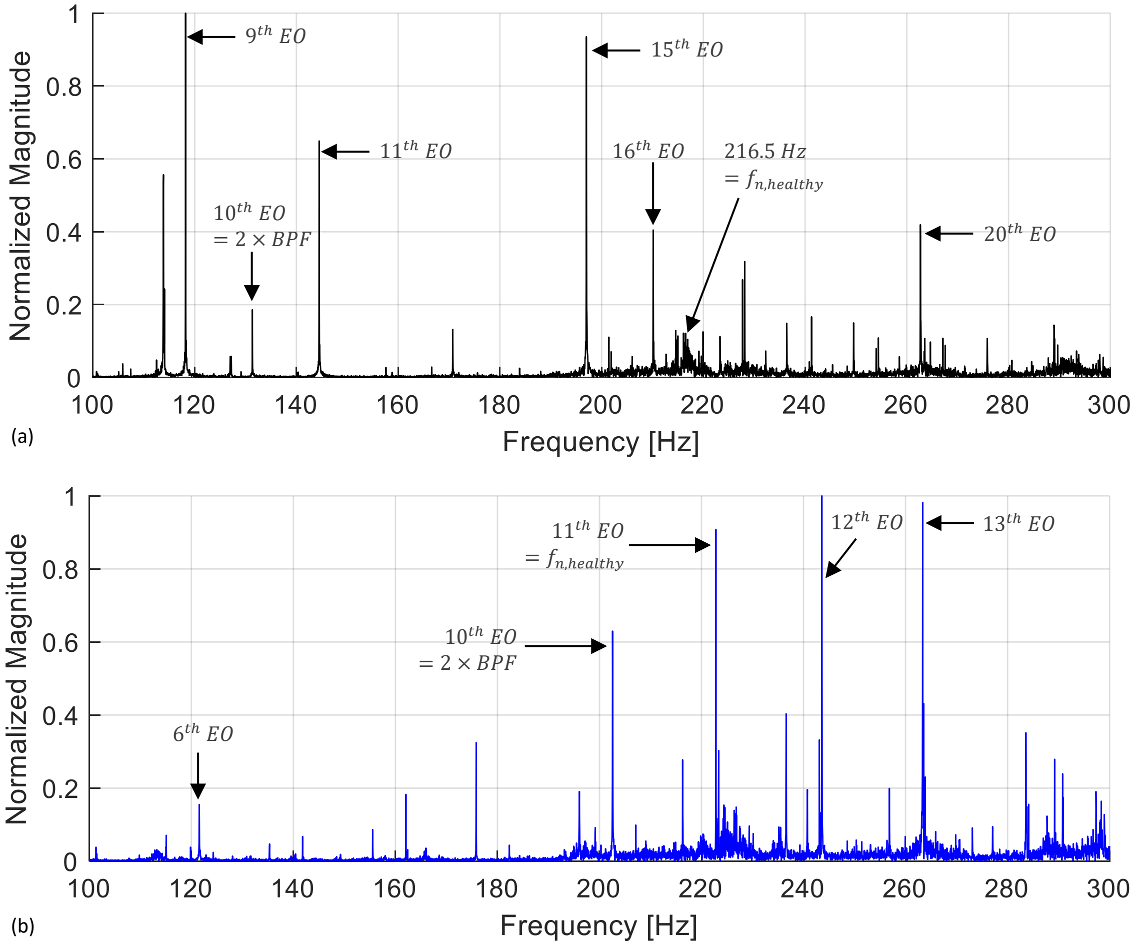

Figure 4.15. FFT magnitude plot of the experimental damaged configuration casing acceleration for: 787 rpm (a); and 1215 rpm (b).

4.3.2 Numerical Data Investigation

Shifting the focus now to the numerical model, a Campbell diagram can be presented showing the expected evolution of the blade's natural frequency with rotational speed. This is shown in Figure 4.16 along with the $10^{th}\ EO$. The $10^{th}\ EO$ corresponds to the 2^{nd} harmonic of the BPF and is thus identified as a critical blade vibration contributor. Over the specified rotational speed range, the damaged numerical blade's first natural frequency is expected to evolve from $131.2\ Hz$ to $135.1\ Hz$. The experimental damaged blade, of course, will have a larger change in natural frequency.

Next, the spectra for two constant rotational speeds will be presented. The speeds shown are the maximum speed imposed by the limits of the experimental test turbine of $1418\ rpm$ and the critical numerical speed of $787\ rpm$. The former speed relates to the $10^{th}\ EO$ excitation of the damaged numerical blade. An additional set of results for a speed of $1350\ rpm$ can be found in Appendix C: Additional FSI Simulation Results.

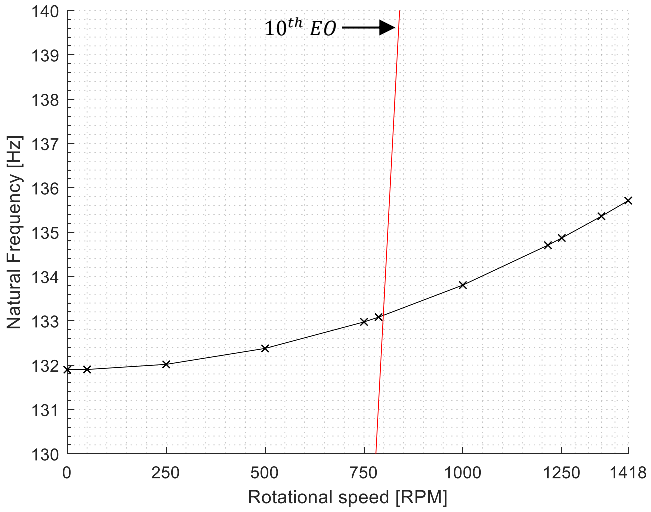

Figure 4.16. Campbell diagram for the numerical damaged blade's first natural frequency

A few conclusions can be drawn from the spectra shown in Figure 4.17. The spectrum magnitude of the maximum speed's casing pressure includes peaks at the 5^{th}, $10^{th}$and 12^{th} EO frequencies. These significant peaks, as well as all the other EO frequencies, are not sufficiently close to the natural frequency of the damaged rotor blade and therefore the blade is not excited. This was also observed for the healthy blade and it is thus expected that the damaged rotor blade responds in a similar manner.

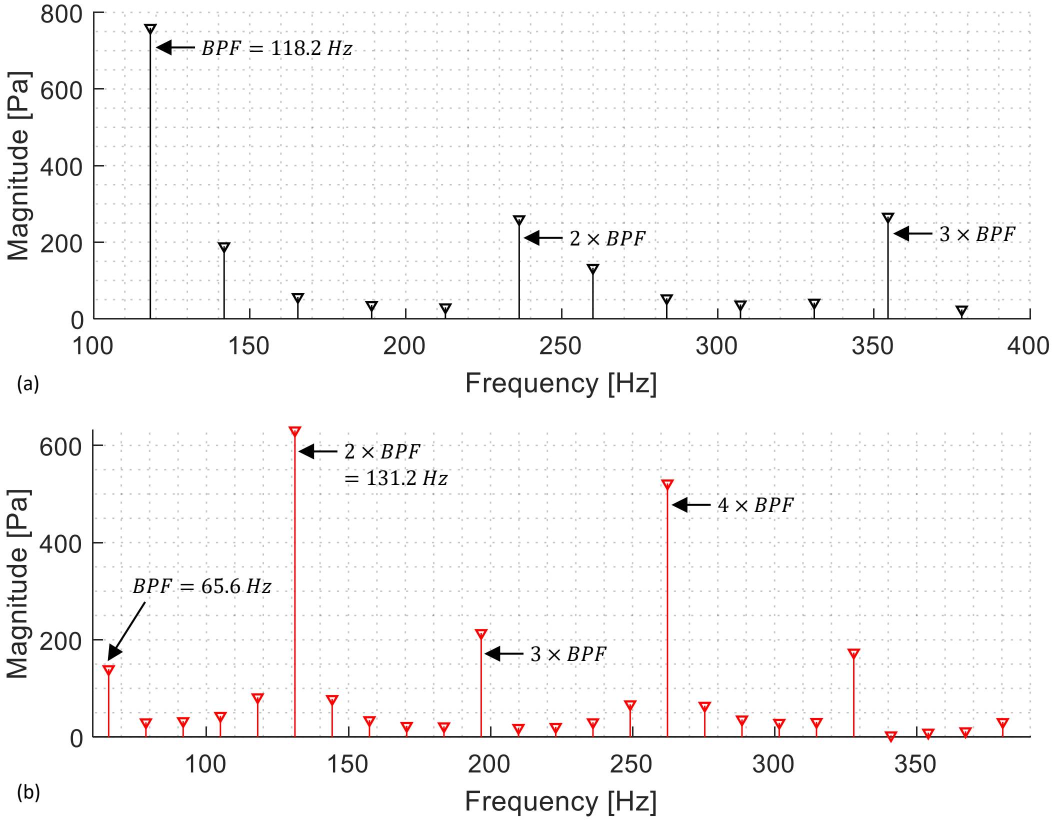

Figure 4.17. FFT magnitude of the FSI model casing at: 1418 rpm (a); and 787 rpm (b) for the healthy configuration.

Viewing the spectrum produced by the critical speed of 787 rpm, findings analogous to the healthy blade results can be made. The 2^{nd} harmonic of the BPF, or the 10^{th} EO, coincides with the natural frequency of the damaged blade. This ultra-harmonic forced vibration leads to resonance of the damaged blade. This statement is again supported by the transient pressure profile together with the transient fluid mesh displacement profile of the FSI model at the casing monitor point. Both of these profiles can be seen for the different rotational speeds in Figure 4.18.

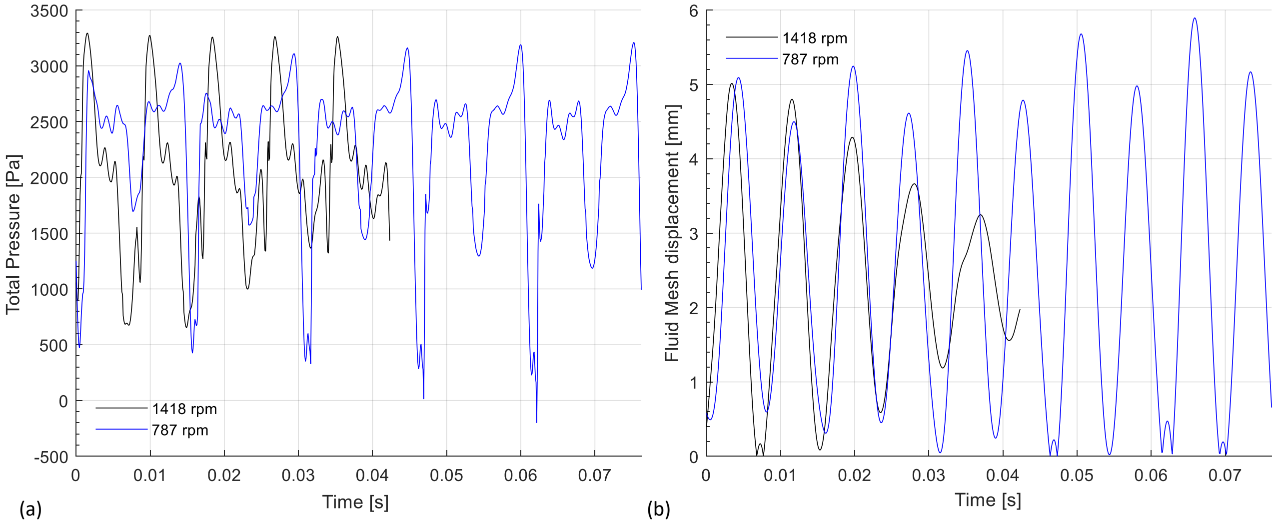

Figure 4.18. FSI casing: pressure (a) and fluid mesh displacement (b) transient profiles for different rotational speeds of the damaged rotor blade

It is clear that for the speed of 787 rpm, both the pressure and displacement profiles diverge due to the blade resonating at its natural frequency, whereas the responses of the maximum speed case are dampened out. This is supportive evidence that blade condition information can be detected in the pressure field of a two-way FSI model. The information extracted pertains to the resonance frequency of the blade when exciting the blade with an appropriate EO frequency. An appropriate EO frequency would be one that is strongly related to the physics involved in the problem - which is most likely to be the blade passing frequency or a harmonic thereof.

4.4 Conclusion of the Discussion of Results Section

This chapter presented the numerical and experimental results of this study through an in-depth analysis. The primary objective that this study set out to achieve, namely, to what extent can blade condition information be extracted from a pressure field of a turbine stage passage when using a two-way fluid-structure interaction model, was successfully accomplished.

Firstly, an uncertainty quantification for the effect of the measured inlet velocity was presented to determine the effect on the frequency response of the flow field. Secondly, a brief overview of the differences between a CFD-*only* model and FSI model was presented. Thirdly, the healthy rotor blade configuration analysis was presented as the main investigation. Lastly, a damaged rotor blade FSI model was reviewed in terms of the information that can be extracted from its flow field as supporting evidence to the claims made in the main investigation.

The findings confirmed that blade condition information can be detected in the pressure field of a two-way FSI model. The blade condition information that was extracted from the pressure field, as well as the fluid mesh deformation field, coincided with the resonance frequency of the blade. In each case, the resonance frequency of the blade coincided with an EO equal to the second harmonic of the blade passing frequency. Other EO frequencies within one order of the second harmonic of the blade passing frequency also showed low-amplitude vibration of the blade in the region of resonance. Collectively, this type of forced vibration is termed ultra-harmonic, or harmonic multiple forced vibration.

Synchronous vibration, or EO vibration, is a major component in turbomachinery vibration. This has been highlighted in this section. Even if the base forcing frequency - the rotational speed - is not near the natural frequency of the blade, the EO frequencies that are in close vicinity of the blade natural frequency lead to either an amplified response of the blade or to the resonance of the blade. This is, however, dependent on the strength of the harmonic. An appropriate EO frequency would be one that is strongly related to the physics involved in the problem - which is most likely to be the blade passing frequency or a harmonic thereof.

A few challenges were however encountered, as extending the FSI model to evaluate a damaged blade was far more complex than anticipated. The damaged rotor configuration of the experimental turbine consisted of four healthy blades and a single damaged blade. Setting up the numerical model with a single stator and rotor blade assumes that identical flow profiles exist in each blade passage as all the rotor blades have the same profile. This was the key difference between the experimental and numerical model that did not allow for direct comparison.

5 Conclusion and Recommendations

5.1 Conclusion

In this dissertation a three-dimensional two-way fluid-structure interaction model of a single turbine stage blade passage was developed. The primary objective was to investigate what blade vibration information could be obtained from the pressure field around the rotor blade. The secondary objective required minimising the computational effort while retaining accuracy of the model.

Analyses into mesh independent solutions were undertaken for both the structural and fluid domains. As the FSI model solution would be transient in nature, a timestep sensitivity study was included to ensure adequate temporal discretization. Furthermore, the study involved investigations of a healthy rotor blade and a damaged rotor blade - which was a reduced thickness version of the healthy rotor blade. Accommodating the numerical model, was an experimental test turbine that was used to gather experimental data for validation of the numerical model. The single-stage test turbine was comprised of five upstream stator blades and five rotor blades. Two rotor blade assemblies were tested with the first configuration consisting of five healthy blades, and the second configuration consisting of four healthy blades and one damaged blade. All simulations were performed at constant rotational speeds for one single revolution of the rotor. Structural damping of the rotor blades was, however, not considered. All numerical simulations were carried out using the commercial multiphysics software package of Ansys R2 2019 and the explicit use of CFX for the CFD simulations.

The numerical study was split up into four key analyses. Firstly, the effect of the uncertainty in the measurement of inlet velocity was quantified. Secondly, validation of the FSI model in terms of the contents extracted from a CFD-*only* model as opposed to a similar FSI model were reviewed. Thirdly, the healthy rotor blade configuration analysis was presented as the main investigation. Lastly, a damaged rotor blade FSI model was reviewed in terms of the information that could be extracted from its flow field as supporting evidence to the claims made in the main investigation.

The uncertainty quantification of the inlet velocity proved that the inlet velocity only influences the magnitude of the response and, for the given ranges tested, the distribution of the frequency spectra remains unaffected. This led to using the experimentally measured inlet velocity for the remainder of all FSI and CFD simulations.

Studying the difference of the FSI and CFD-*only* pressure profiles, it was observed that the pressure differences between the FSI and CFD-*only* models were effectively the pressure changes produced by the pressure force exerted on the fluid by the blade. It was clearly shown that this blade pressure force made a significant contribution to the FSI model's pressure profile as the major contributing frequencies of the FSI and CFD-*only* models were located at different EOs for the same rotational speed. Furthermore, the spectrum of the pressure difference clearly showed the contributing frequencies of the blade's pressure force exerted on the fluid, suggesting a strong coupling between the blade motion and the surrounding pressure field.

The main analysis confirmed that blade condition information can be detected in the pressure field of a two-way FSI model. The blade condition information that was extracted from the pressure field, as well as the fluid mesh deformation field, coincided with the resonance frequency of the blade. In each case, the resonance frequency of the blade coincided with an EO equal to the second harmonic of the blade passing frequency. Other EO frequencies - within one order of the second harmonic of the blade passing frequency - also showed low-amplitude vibration of the blade in the region of resonance. Collectively, this type of forced vibration is termed ultra-harmonic, or harmonic multiple forced vibration.

The fact that the blade resonance frequency can be extracted from the pressure field of a two-way FSI model makes it a promising numerical diagnostics or prognostics tool. This is due to the resonance frequency being a strong indicator of blade health. As a more complex - and more realistic - representation of the turbomachinery flow physics is being observed through this strong two-way coupling, more accurate solutions for pressure and blade vibratory motion is achieved. Furthermore, as this has been proved numerically, it can be extended to non-intrusive condition-monitoring of the rotor blades using characteristics of the flow-field, in practice. Once the operating conditions are known and a baseline pressure profile has been recorded, the scenario can be recreated numerically to predict downstream flow characteristics or be coupled with a fatigue analysis to determine the remaining useful life of a blade as an example.

The findings made in this study lay the foundation for a more complete diagnostic or prognostic model that is based on blade resonance frequencies. The novelty lies in the approach taken in this study, which offers improvements in certain areas over previous work by the likes of Forbes, Alshroof and Randall (2011), Alshroof *et al.* (2012) and Rao and Dutta (2014) in the sense that two-way fluid-structure interaction was modelled for a three-dimensional blade passage domain and pressure profile spectra were subsequently studied for blade condition information.

However, a few challenges were encountered when extending the FSI model to evaluate a damaged blade. This idea was far more complex than anticipated. The damaged rotor configuration of the experimental turbine consisted of four healthy blades and a single damaged blade. Setting up the numerical model with a single stator and rotor blade assumed that identical flow profiles existed in each blade passage as all the rotor blades had the same profile. This was the key difference between the experimental and numerical model, and as such, the results could not be directly compared. A numerical analysis similar to the healthy blade analysis was conducted for the damaged blade in which analogous findings were made about the blade natural frequency being extracted from the pressure profile around the blade through ultra-harmonic forced vibration of the blade.

Nonetheless, synchronous vibration is a major component in turbomachinery vibration. Engine-ordered frequencies that are in close vicinity of the blade natural frequency lead to either an amplified response of the blade or to the resonance of the blade. It has been proved that this vibration profile can be extracted from the pressure field of a two-way FSI model of a turbine blade passage and that the further development of such a model will be beneficial, especially seeing that computational power has become more readily available.

5.2 Recommendations

The following recommendations are made for future work to improve the numerical model:

- Inclusion of damping in the structural analyses (modal and transient cases).
- Quantification of the effect that the viscous damping of the fluid has on the blade structure.
- Modelling of the velocity inlet profile to better represent a physical turbine (instead of a near-uniform inlet flow). The experimental model should be numerically recreated, essentially.
- Investigation of higher-pressure flow (for an adequately sized domain)
- To further develop the model to be able to identify blade damage. This would either require simulation of the full annulus or incorporation of the flow effects of healthy blade passages on the damaged blade passage.
- Implementation of more sensitive microphones, or perhaps better suited sensors to measure the pressure experimentally.

References

Agilis (2014) *Non-Intrusive Stress Measurement Systems vs. Strain Gauges*. Available at: http://agilisengineering.com/agilis-blog.html (Accessed: 30 August 2018).

Ali, Z., Tyacke, J., Tucker, P. G. and Shahpar, S. (2016) 'Block topology generation for structured multi-block meshing with hierarchical geometry handling', *Procedia Engineering*. The Author(s), 163, pp. 212–224. doi: 10.1016/j.proeng.2016.11.050.

Allport, J. M., Jupp, M. L., Pezouvanis, A., Janicki, G. W., Pierończyk, A. I., Day, A. J., Olley, P., Mason, B. and Ebrahimi, M. K. (2012) 'Turbocharger blade vibration : Measurement and validation through laser tip-timing', *10th International Conference on Turbochargers and Turbocharging*, p. 173. doi: http://dx.doi.org/10.1533/9780857096135.3b.173.

Alshroof, O. N., Forbes, G. L., Sawalhi, N., Randall, R. B. and Yeoh, G. H. (2012) 'Computational fluid dynamic analysis of a vibrating turbine blade', *International Journal of Rotating Machinery*, 2012. doi: 10.1155/2012/246031.

ANSYS (2018a) 'ANSYS CFX-Solver Modeling Guide 19.2'. Southpointe, Canonsburg.

ANSYS (2018b) 'ANSYS CFX-Solver Theory Guide R19.2'. Southpointe, Canonsburg.

ANSYS (2018c) 'ANSYS CFX Reference Guide R19.2'. Southpointe, Canonsburg.

ANSYS (2018d) 'ANSYS Fluent Theory Guide 19.1'. Southpointe, Canonsburg.

ANSYS (2018e) 'ANSYS TurboGrid User's Guide R19.2'. Southpointe, Canonsburg.

ANSYS (2019) 'ANSYS Mechanical User's Guide'. Southpointe, Canonsburg.

Argyropoulos, C. D. and Markatos, N. C. (2015) 'Recent advances on the numerical modelling of turbulent flows', *Applied Mathematical Modelling*. Elsevier Inc., 39(2), pp. 693–732. doi: 10.1016/j.apm.2014.07.001.

Battiato, G., Firrone, C. M. and Berruti, T. M. (2017) 'Forced response of rotating bladed disks: Blade Tip-Timing measurements', *Mechanical Systems and Signal Processing*. Elsevier, 85(July 2016), pp. 912–926. doi: 10.1016/j.ymssp.2016.09.019.

Beauseroy, P. and Lengellé, R. (2007) 'Nonintrusive turbomachine blade vibration measurement system', *Mechanical Systems and Signal Processing*, 21(4), pp. 1717–1738. doi: 10.1016/j.ymssp.2006.07.015.

Benra, F. K., Dohmen, H. J., Pei, J., Schuster, S. and Wan, B. (2011) 'A comparison of one-way and two-way coupling methods for numerical analysis of fluid-structure interactions', *Journal of Applied Mathematics*, 2011. doi: 10.1155/2011/853560.

Booysen, C. (2014) *Fatigue Life Prediction of Steam Turbine Blades during Start-up Operation Using Probabilistic Concepts*. University of Pretoria.

Boyce, M. P. (2012) *Gas Turbine Engineering Handbook*. Fourth. Oxford: Elsevier.

Brahimi, F. and Ouibrahim, A. (2016) 'Blade dynamical response based on aeroelastic analysis of fluid structure interaction in turbomachinery', *Energy*. Elsevier Ltd, 115, pp. 986–995. doi:

10.1016/j.energy.2016.09.071.

Carrington, I. B., Wright, J. R., Cooper, J. E. and Dimitriadis, G. (2001) 'A comparison of blade tip timing data analysis methods', *Proceedings of the Institution of Mechanical Engineers, Part G: Journal of Aerospace Engineering*, 215(5), pp. 301–312. doi: 10.1243/0954410011533293.

Chung, T. J. (2002) *Computational Fluid Dynamics.*, *The British journal of radiology*. doi: 10.1007/s10915-006-9104-x.

Degroote, J., Bathe, K. J. and Vierendeels, J. (2009) 'Performance of a new partitioned procedure versus a monolithic procedure in fluid-structure interaction', *Computers and Structures*. Elsevier Ltd, 87(11–12), pp. 793–801. doi: 10.1016/j.compstruc.2008.11.013.

Denton, J. D. (2010) 'Some Limitations of Turbomachinery CFD', in *Proceedings of ASME Turbo Expo 2010: Power for Land, Sea and Air*. Glasgow, UK, pp. 735–745. doi: 10.1115/GT2010-22540.

Diamond, D. H. and Heyns, P. S. (2018) 'A novel method for the design of proximity sensor configuration for rotor blade tip timing (accepted manuscript)', *Journal of Vibration and Acoustics*, 140(VIB-17-1510), pp. 1–23. doi: 10.1115/1.4039931.

Dimitriadis, G., Carrington, I. B., Wright, J. R. and Cooper, J. E. (2002) 'Blade-tip timing measurement of synchronous vibrations of rotating bladed assemblies', *Mechanical Systems and Signal Processing*, 16(4), pp. 599–622. doi: 10.1006/mssp.2002.1489.

Drozdowski, R., Völker, L., Häfele, M. and Vogt, D. M. (2016) 'Numerical and experimental analysis of low-pressure steam turbine blades coupled with lacing wire', *Journal of Power and Energy*, 230(3), pp. 332–342. doi: 10.1177/0957650915627563.

Engineering ToolBox (2005) *Dry Air Properties [online]*. Available at: https://www.engineeringtoolbox.com/dry-air-properties-d_973.html (Accessed: 1 May 2019).

EPRI (1985) 'Survey of Steam Turbine Blade Failures'. Palto Alto. doi: CS-3891.

EPRI (2008) *Steam Turbine Blade Failure Root Cause Analysis Guide*. Palo Alto, CA. doi: 1014137.

Eskom Holdings (2019) *Kriel Power Station*. Available at: http://www.eskom.co.za/sites/heritage/Pages/KRIELPOWERSTATION.aspx (Accessed: 3 April 2019).

Forbes, G. L. (2010) 'Non-contact gas turbine blade vibration monitoring using internal pressure and casing response measurements', (January), pp. 1–2.

Forbes, G. L., Alshroof, O. N. and Randall, R. B. (2011) 'Fluid-structure interaction study of gas turbine blade vibrations', in *Australian Journal of Mechanical Engineering*, pp. 143–150.

Forbes, G. L. and Randall, R. B. (2007) 'Simulated Gas Turbine Casing Response to Rotor Blade Pressure Excitation', *5th Australasian Congress on Applied Mechanics, ACAM 2007 10-12 December 2007*, (December).

Forbes, G. L. and Randall, R. B. (2013) 'Estimation of turbine blade natural frequencies from casing pressure and vibration measurements', *Mechanical Systems and Signal Processing*. Elsevier, 36(2), pp. 549–561. doi: 10.1016/j.ymssp.2012.11.006.

Gilkeson, C. A., Toropov, V. V., Thompson, H. M., Wilson, M. C. T., Foxley, N. A. and Gaskell, P. H. (2014)

'Dealing with numerical noise in CFD-based design optimization', *Computers and Fluids*. Elsevier Ltd, 94, pp. 84–97. doi: 10.1016/j.compfluid.2014.02.004.

Heath, S. and Imregun, M. (1996) 'An improved single-parameter tip-timing method for turbomachinery blade vibration measurements using optical laser probes', *International Journal of Mechanical Sciences*, 38(10), pp. 1047–1058. doi: 10.1016/0020-7403(95)00116-6.

Heinz, C., Schatz, M., Casey, M. V. and Stuer, H. (2010) 'Experimental and Analytical Investigations of a Low Pressure Model Turbine during Forced Response Excitation', in *Proceedings of ASME Turbo Expo 2010: Power for Land, Sea and Air*. Glasgow, UK.

Henningson, D. S. and Berggren, M. (2005) 'Fluid Dynamics : Theory and Computation'. KTH, Stockholm, p. 177.

Knappett, D. and Garcia, J. (2008) 'Blade tip timing and strain gauge correlation on compressor blades', 222, pp. 497–507. doi: 10.1243/09544100JAERO257.

Krack, M., Salles, L. and Thouverez, F. (2016) 'Vibration Prediction of Bladed Disks Coupled by Friction Joints', *Archives of Computational Methods in Engineering*. Springer Netherlands, 24(3), pp. 589–636. doi: 10.1007/s11831-016-9183-2.

Lin, J., Hu, Z., Chen, Z. S., Yang, Y. M. and Xu, H. L. (2016) 'Sparse reconstruction of blade tip-Timing signals for multi-mode blade vibration monitoring', *Mechanical Systems and Signal Processing*. Elsevier, 81, pp. 250–258. doi: 10.1016/j.ymssp.2016.03.020.

Logan, E. J. and Roy, R. (eds) (2003) *Handbook of Turbomachinery*. 2nd edn. Available at: http://ebooks.bharathuniv.ac.in/gdlc1/gdlc1/Engineering Library/Earl Logan/Handbook of Turbomachinery (447)/Handbook of Turbomachinery - Earl Logan.pdf.

McCloskey, T. H. (2002) 'Troubleshooting turbine steam path damage mechanisms', in *Proceedings of the thirty-first turbomachinery symposium*, pp. 105–144. doi: 10.1115/IJPGC2002-26108.

Megerle, B. (2014) *Unsteady Aerodynamics of Low-Pressure Steam Turbines Operating Under Low Volume Flow Conditions*. Swiss Federal Institute of Technology.

Meher-Homji, C. B. (1995) 'Blading vibration and failures in gas turbines part A: blading dynamics and the operating environment', pp. 1–11.

Mohan, R. S., Sarkar, A. and Sekhar, A. S. (2014) 'Vibration analysis of a steam turbine blade', pp. 1–10.

Pichler, R., Sandberg, R. D., Michelassi, V. and Bhaskaran, R. (2016) 'Investigation of the Accuracy of RANS Models to Predict the Flow Through a Low-Pressure Turbine', *Journal of Turbomachinery*, 138(12), p. 121009. doi: 10.1115/1.4033507.

Rao, A. R. and Dutta, B. K. (2010) 'Non Intrusive Method of Detecting Turbine Blade Vibration in an Operating Power Plant', *Proceedings of the International Conference on Noise and Vibration Engineering*, (March 2015), pp. 2937–2948.

Rao, A. R. and Dutta, B. K. (2012) 'In Situ Detection of Turbine Blade Vibration and Prevention', pp. 567–574. doi: 10.1007/s11668-012-9597-6.

Rao, A. R. and Dutta, B. K. (2014) 'Blade vibration triggered by low load and high back pressure', *Engineering Failure Analysis*. Elsevier Ltd, 46, pp. 40–48. doi: 10.1016/j.engfailanal.2014.07.023.

Ratz, J., Forbes, G. L. and Randall, R. B. (2013) 'Gas Turbine Blade Natural Frequency Measurement Using External Casing Vibrations', *Proceedings of the 59th International Instrumentation Symposium and MFPT Conference*, pp. 1–10.

Rigosi, G., Battiato, G. and Berruti, T. M. (2017) 'Synchronous vibration parameters identification by tip timing measurements', *Mechanics Research Communications*. Elsevier Ltd., 79, pp. 7–14. doi: 10.1016/j.mechrescom.2016.10.006.

Roache, P. J. (1994) 'Perspective: A Method for Uniform Reporting of Grid Refinement Studies', *Journal of Fluids Engineering*, 116, pp. 405–413.

Russhard, P. (2015) 'The Rise and Fall of the Rotor Blade Strain Gauge', in *Vibration Engineering and Technology of Machinery*. Springer, pp. 27–38. doi: 10.1007/978-3-319-09918-7.

Sabbatini, D., Peeters, B., Martens, T. and Janssens, K. (2012) 'Data acquisition and processing for tip timing and operational modal analysis of turbomachinery blades', in *AIP Conference Proceedings*, pp. 52–60. doi: 10.1063/1.4730542.

Salhi, B., Lardiès, J., Berthillier, M., Voinis, P. and Bodel, C. (2008) 'Modal parameter identification of mistuned bladed disks using tip timing data', *Journal of Sound and Vibration*, 314(3–5), pp. 885–906. doi: 10.1016/j.jsv.2008.01.050.

Schönleitner, F., Traussnig, L., Heitmeir, F. and Marn, A. (2015) 'Modal Characterization, Strain Gauge Setup and 1-Way FSI of a Low Pressure Turbine Rotor Blading', in *Volume 7B: Structures and Dynamics*, p. V07BT32A015. doi: 10.1115/GT2015-42717.

Du Toit, R. G. (2017) *A Stochastic Hybrid Blade Tip Timing Approach for the Identification and Classification of Turbomachine Blade Damage Master of Mechanical Engineering*. University of Pretoria.

Ubulom, I. A., Neely, A. J. and Shankar, K. K. (2017) 'Fluid-Structure Interactions for High-Cycle Fatigue Life Estimation', *Proceedings of the 27th ISABE Conference*, pp. 1–23.

Zhang, D., Hong, J., Ma, Y. and Chen, L. (2011) 'A probability method for prediction on High Cycle Fatigue of blades caused by aerodynamic loads', *Advances in Engineering Software*. Elsevier Ltd, 42(12), pp. 1059–1073. doi: 10.1016/j.advengsoft.2011.07.010.

Zhang, L. Y., He, L. and Stüer, H. (2012) 'A Numerical Investigation of Rotating Instability in Steam Turbine Last Stage', *Journal of Turbomachinery*, 135(011009). doi: 10.1115/1.4006330.

Zielinski, M. and Ziller, G. (2000) 'Noncontact vibration measurements on compressor rotor blades', *Analysis*, 847.

Appendices

Appendix A: Computational Run Times

The computational times are listed in the table below for selected FSI and transient CFD runs. The simulations were run for six blade passing periods. The system used to perform the simulations is reiterated here as a reminder to the reader.

System Specifications:

- AMD Ryzen 7 2700X CPU (8 x cores, 16 threads, 3.7 (4.3 GHz Turbo)). All threads were utilised in each simulation performed.
- 32GB DDR4 RAM (2667 MHz)

Simulation	**Physical time simulated [s]**	**Solve Time [hours]**
	FSI	
Healthy - $1418\ rpm, V_{in} = 65\ m/s$	0.050776	87.45
Healthy - $1350\ rpm, V_{in} = 65\ m/s$	0.053334	95.79
Healthy - $1215\ rpm, V_{in} = 65\ m/s$	0.05926	107.41
Healthy - $1215\ rpm, V_{in} = 52\ m/s$	0.05926	111.69
Healthy - $1215\ rpm, V_{in} = 41.6\ m/s$	0.05926	110.12
Damaged - $1418\ rpm, V_{in} = 65\ m/s$	0.050776	103.81
Damaged - $1350\ rpm, V_{in} = 65\ m/s$	0.053334	107.78
Damaged - $787\ rpm, V_{in} = 65\ m/s$	0.091487	224.43
	CFD	
Healthy - $1418\ rpm, V_{in} = 65\ m/s$	0.050776	17.69
Healthy - $1215\ rpm, V_{in} = 65\ m/s$	0.05926	18.76

Appendix B: Natural Frequency Evolution of the Healthy Experimental Blade

The table below shows the estimated natural frequency of the healthy experimental blade as a function of rotational speed.

Rotational speed [rpm]	Natural Frequency [Hz]
0	202.5
175	204.8
202.4	205.8
235.5	206.9
312.3	208
378.8	209
432.3	210.1
506.7	211.2
551.4	212.2
624.7	213.3
678.5	214.4
738	215.4
813.5	216.5
916.5	217.6
927.2	218.6
1000.3	219.7
1024.8	220.8
1107	221.8
1206.6	224
1353.8	226.1
1380.3	227.2

Appendix C: Additional FSI Simulation Results

An additional simulation was performed using the damaged rotor blade model. The FFT magnitude plot of the is shown below for a rotational speed of $1350\ rpm$. No frequencies pertaining to blade condition information are present in the spectrum. This is due to the EO frequencies not being near to the natural frequency of the damaged blade. The three frequencies that appear clearly in the spectrum are the blade passing frequency and its first two harmonics.

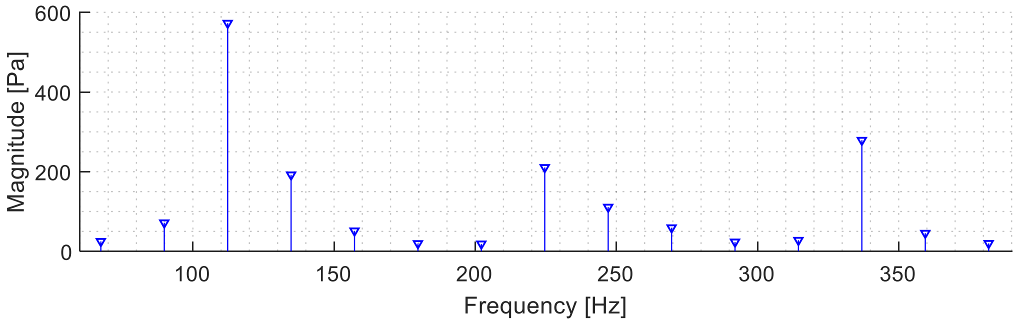

Appendix D: Test Turbine Technical Drawings

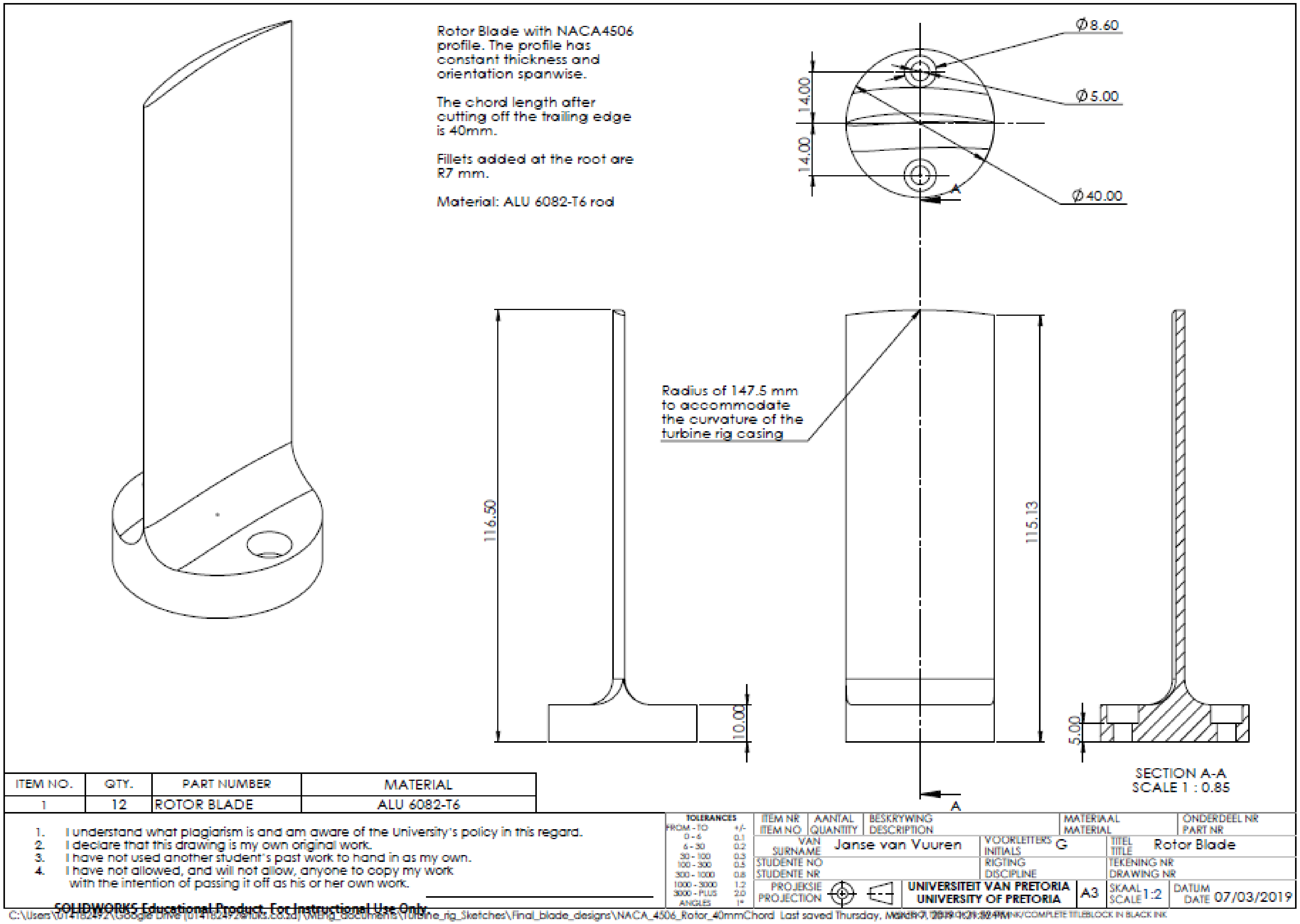

Rotor Blade with NACA4506 profile. The profile has constant thickness and orientation spanwise.

The chord length after cutting off the trailing edge is 40mm.

Fillets added at the root are R7 mm.

Material: ALU 6082-T6 rod

Radius of 147.5 mm to accommodate the curvature of the turbine rig casing

ITEM NO.	QTY.	PART NUMBER	MATERIAL
1	12	ROTOR BLADE	ALU 6082-T6

1. I understand what plagiarism is and am aware of the University's policy in this regard.
2. I declare that this drawing is my own original work.
3. I have not used another student's past work to hand in as my own.
4. I have not allowed, and will not allow, anyone to copy my work with the intention of passing it off as his or her own work.

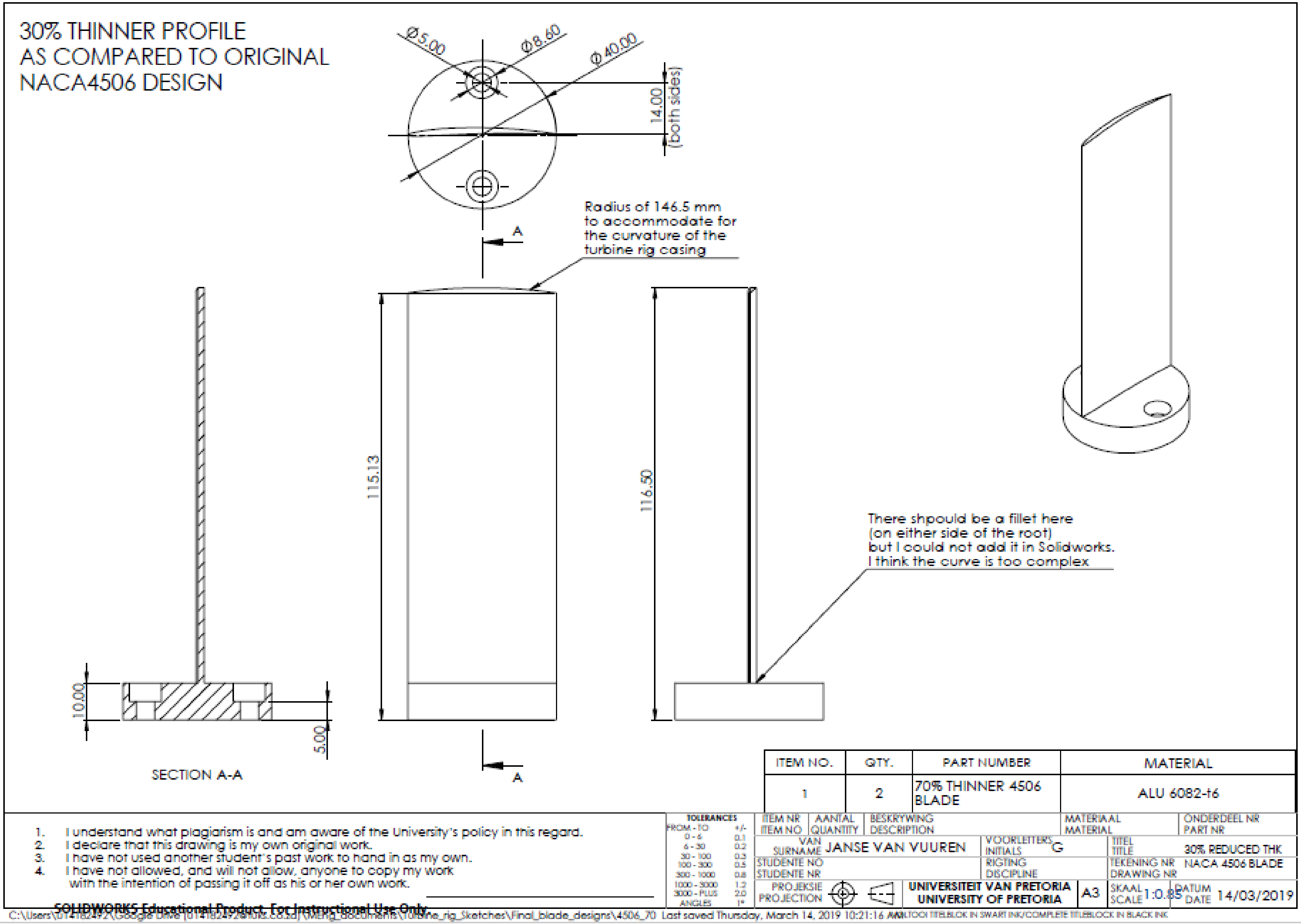

Radius of 146.5 mm to accommodate for the curvature of the turbine rig casing

There shpould be a fillet here (on either side of the root) but I could not add it in Solidworks. I think the curve is too complex

ITEM NO.	QTY.	PART NUMBER	MATERIAL
1	2	70% THINNER 4506 BLADE	ALU 6082-t6

1. I understand what plagiarism is and am aware of the University's policy in this regard.
2. I declare that this drawing is my own original work.
3. I have not used another student's past work to hand in as my own.
4. I have not allowed, and will not allow, anyone to copy my work with the intention of passing it off as his or her own work.

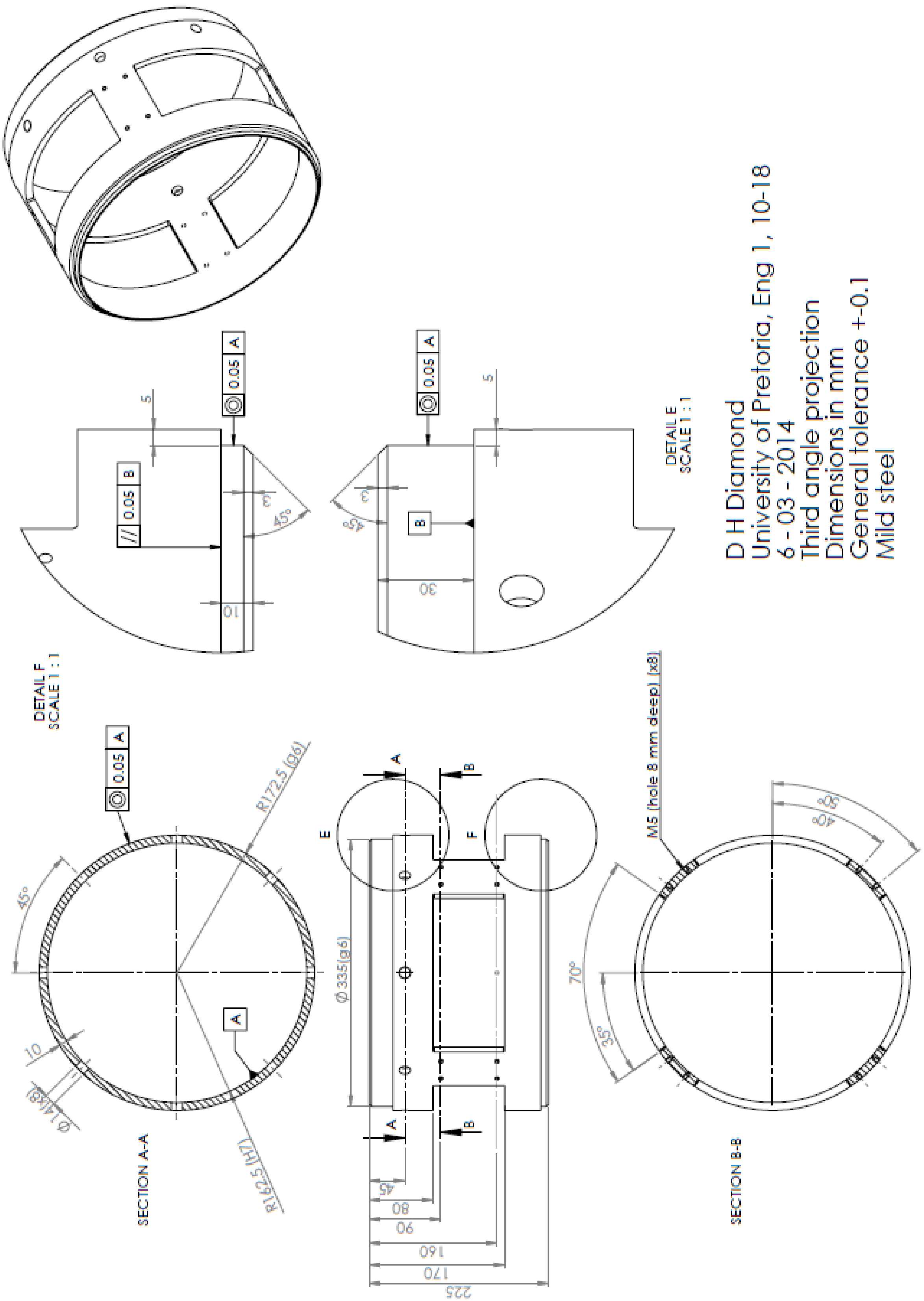
D H Diamond
University of Pretoria, Eng 1, 10-18
6 - 03 - 2014
Third angle projection
Dimensions in mm
General tolerance +-0.1
Mild steel
DETAIL E
SCALE 1 : 1
DETAIL F
SCALE 1 : 1
SECTION A-A
SECTION B-B
M5 (hole 8 mm deep) (x8)
R172.5 (g6)
R162.5 (H7)
Ø 335(g6)
Ø 14(x8)
0.05 A
// 0.05 B
A
B
E
F
45°
10
70°
35°
40°
50°
5
3
30
45
80
90
160
170
225

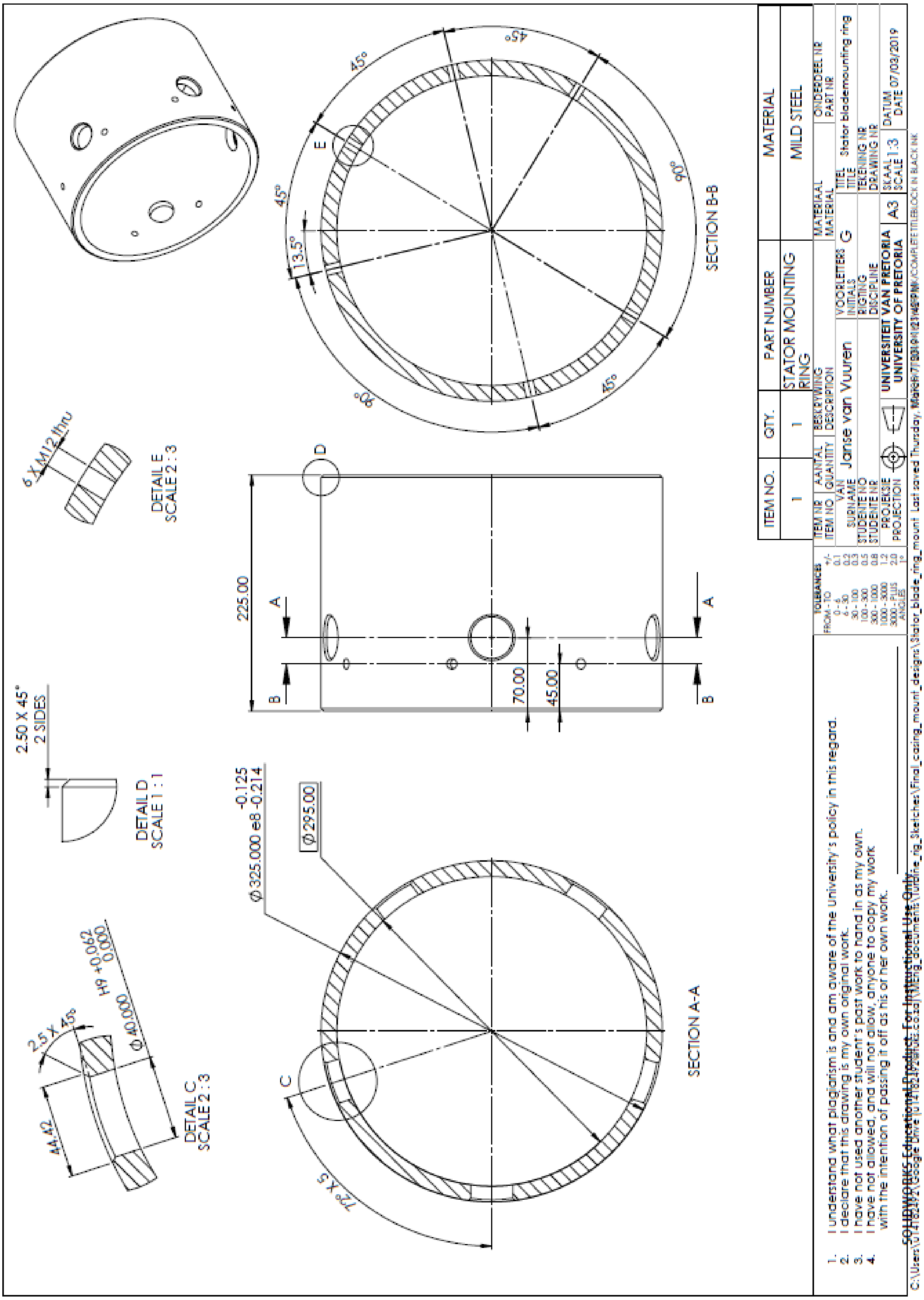
SECTION A-A
SECTION B-B
DETAIL C
SCALE 2 : 3
DETAIL D
SCALE 1 : 1
DETAIL E
SCALE 2 : 3
6 X M12 thru
2.50 X 45°
2 SIDES
225.00
70.00
45.00
A
B
C
D
E
Ø325.000 e8 -0.125 -0.214
Ø295.00
2.5 X 45°
Ø40.000
H9 +0.062 0.000
44.42
72° X 5
45°
45°
45°
45°
90°
90°
13.5°
ITEM NO.
QTY.
PART NUMBER
MATERIAL
1
1
STATOR MOUNTING RING
MILD STEEL
TOLERANCES
FROM - TO +/-
0 - 6 0.1
6 - 30 0.2
30 - 100 0.3
100 - 300 0.5
300 - 1000 0.8
1000 - 3000 1.2
3000 - PLUS 2.0
ANGLES 1°
1. I understand what plagiarism is and am aware of the University's policy in this regard.
2. I declare that this drawing is my own original work.
3. I have not used another student's past work to hand in as my own.
4. I have not allowed, and will not allow, anyone to copy my work with the intention of passing it off as his or her own work.
ITEM NR
ITEM NO
AANTAL
QUANTITY
BESKRYWING
DESCRIPTION
MATERIAAL
MATERIAL
ONDERDEEL NR
PART NR
VAN
SURNAME
Janse van Vuuren
VOORLETTERS
INITIALS
G
TITEL
TITLE
Stator blademounting ring
STUDENTE NO
STUDENTE NR
RIGTING
DISCIPLINE
TEKENING NR
DRAWING NR
PROJEKSIE
PROJECTION
UNIVERSITEIT VAN PRETORIA
UNIVERSITY OF PRETORIA
A3
SKAAL 1:3
SCALE 1:3
DATUM 07/03/2019
DATE
SOLIDWORKS Educational Product. For Instructional Use Only.

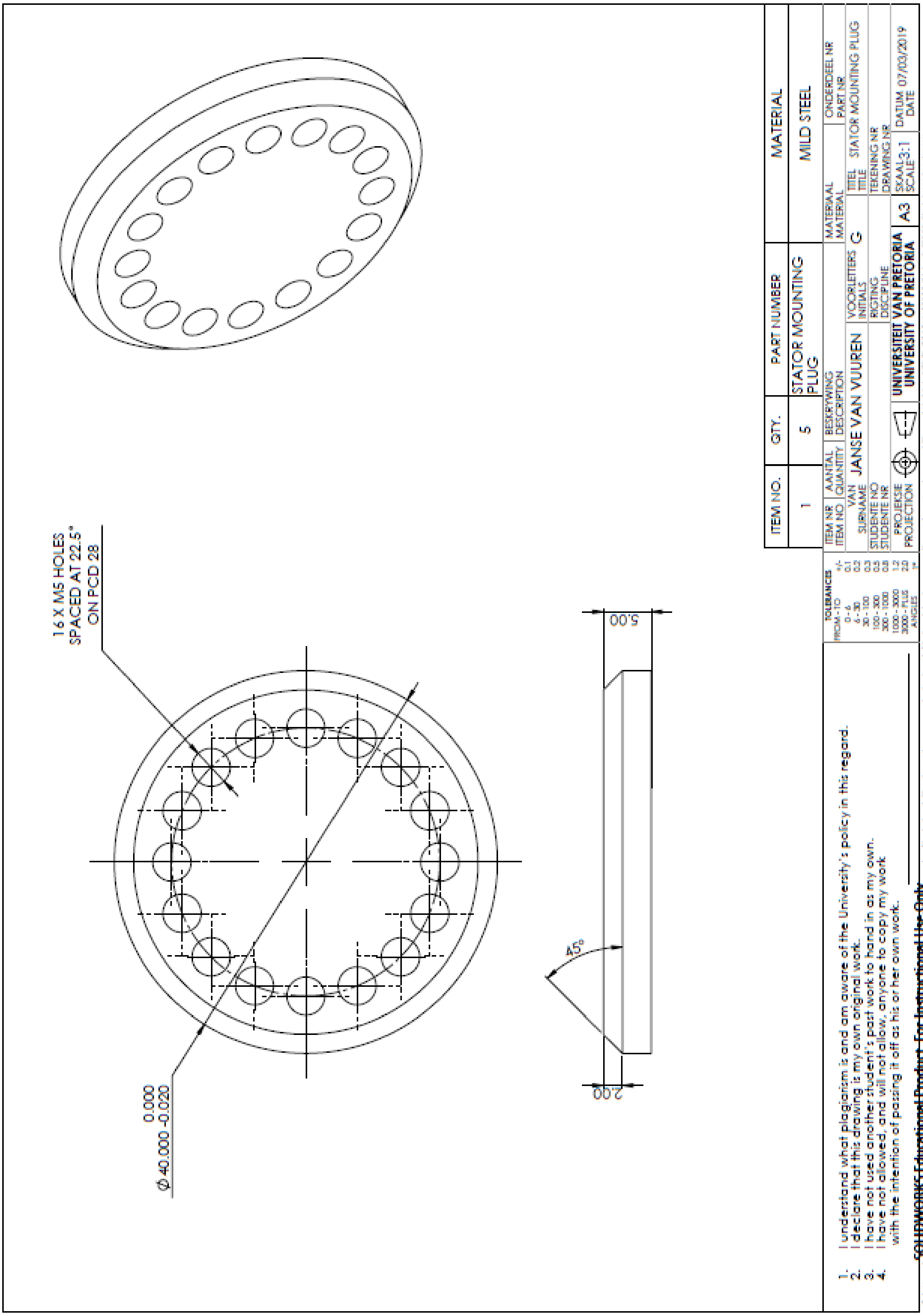
16 X M5 HOLES
SPACED AT 22.5°
ON PCD 28
Ø40.000 0.000 -0.020
5.00
2.00
45°
ITEM NO.
1
QTY.
5
PART NUMBER
STATOR MOUNTING PLUG
MATERIAL
MILD STEEL
VAN SURNAME
JANSE VAN VUUREN
VOORLETTERS INITIALS
G
TITEL TITLE
STATOR MOUNTING PLUG
DATUM DATE
07/03/2019
SKAAL SCALE
3:1
A3
PROJEKSIE PROJECTION
UNIVERSITEIT VAN PRETORIA
UNIVERSITY OF PRETORIA
TOLERANCES
1. I understand what plagiarism is and am aware of the University's policy in this regard.
2. I declare that this drawing is my own original work.
3. I have not used another student's past work to hand in as my own.
4. I have not allowed, and will not allow, anyone to copy my work with the intention of passing it off as his or her own work.
SOLIDWORKS Educational Product. For Instructional Use Only.

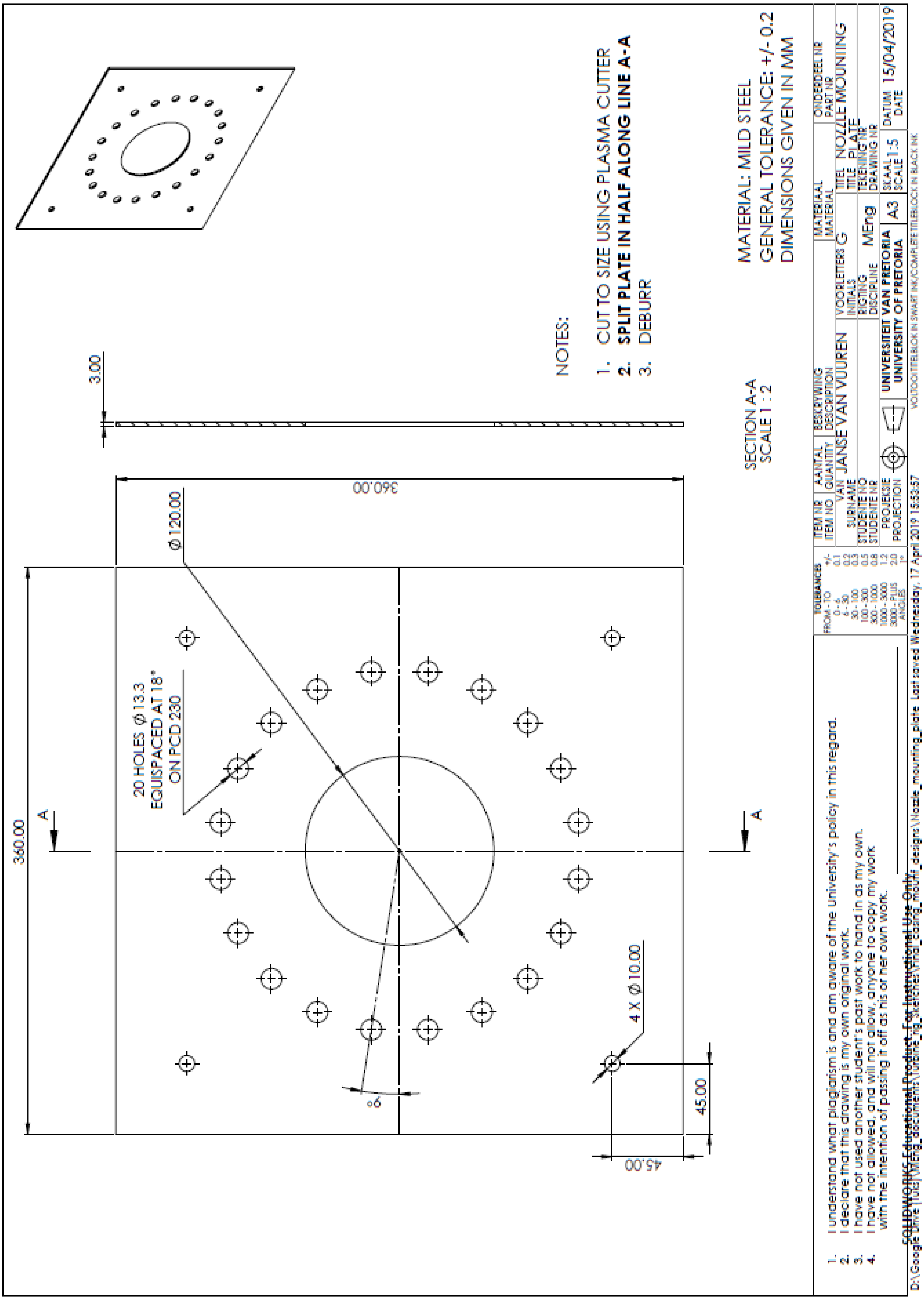
3.00
360.00
Ø120.00
360.00
20 HOLES Ø13.3
EQUISPACED AT 18°
ON PCD 230
A
A
9°
4 X Ø10.00
45.00
45.00
SECTION A-A
SCALE 1 : 2
NOTES:
1. CUT TO SIZE USING PLASMA CUTTER
2. SPLIT PLATE IN HALF ALONG LINE A-A
3. DEBURR
MATERIAL: MILD STEEL
GENERAL TOLERANCE: +/- 0.2
DIMENSIONS GIVEN IN MM
1. I understand what plagiarism is and am aware of the University's policy in this regard.
2. I declare that this drawing is my own original work.
3. I have not used another student's past work to hand in as my own.
4. I have not allowed, and will not allow, anyone to copy my work with the intention of passing it off as his or her own work.
TOLERANCES
FROM - TO +/-
0 - 6 0.1
6 - 30 0.2
30 - 100 0.3
100 - 300 0.5
300 - 1000 0.8
1000 - 3000 1.2
3000 - PLUS 2.0
ANGLES 1°
ITEM NR / ITEM NO
AANTAL / QUANTITY
BESKRYWING / DESCRIPTION
MATERIAAL / MATERIAL
ONDERDEEL NR / PART NR
VAN / SURNAME JANSE VAN VUUREN
VOORLETTERS / INITIALS G
TITEL / TITLE NOZZLE MOUNTING PLATE
STUDENTE NO / STUDENTE NR
RIGTING / DISCIPLINE MEng
TEKENING NR / DRAWING NR
PROJEKSIE / PROJECTION
UNIVERSITEIT VAN PRETORIA / UNIVERSITY OF PRETORIA
A3
SKAAL / SCALE 1:5
DATUM / DATE 15/04/2019
VOLTOOI TITELBLOK IN SWART INK/COMPLETE TITLEBLOCK IN BLACK INK
SOLIDWORKS Educational Product. For Instructional Use Only.
D:\Google Drive (TUKS)\MEng_documents\Turbine_rig_Sketches\Final_casing_mount_designs\Nozzle_mounting_plate Last saved Wednesday, 17 April 2019 15:53:57

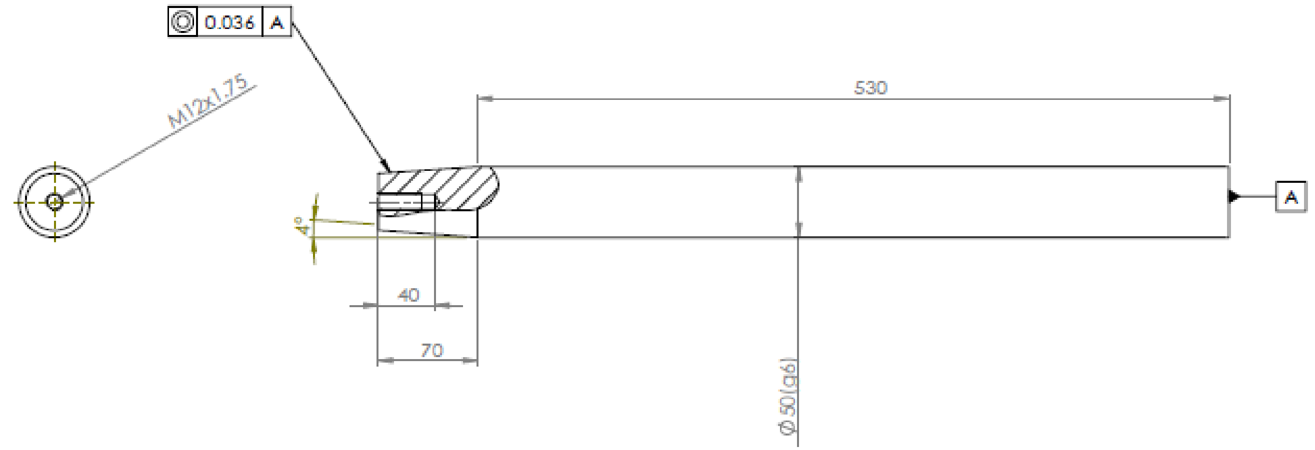

D H Diamond, University of Pretoria, Eng 1, 10-18
24 February 2014
Shaft
Third angle projection
Dimentions in mm
General tolerance: +-0.05
Material will be supplied. Toolsteel